PhD Thesis
Ingeniería Industrial

Biomorphic Silicon Carbide as porous substrate for automotive Diesel Particulate Filters

by

MARÍA DEL PILAR ORIHUELA ESPINA

A Thesis submitted to the
Universidad de Sevilla
for the degree of
DOCTOR OF PHILOSOPHY

Departamento de Ingeniería Energética
Universidad de Sevilla
January 2018

Abstract

Given the amount of diesel vehicles worldwide and their overall environmental impact, particulate emission control is an increasingly important issue. Particles control systems based on improvements of the combustion process or on the design of the engines are not sufficient to comply with current regulations. Therefore, the use of aftertreatment systems has become necessary. The most popular aftertreatment device for the abatement of particles, the wall-flow Diesel Particulate Filter (wall-flow DPF), still has a considerable scope for improvement. The high backpressure they introduce in the exhaust pipe, and the technical issues associated with the on-board regeneration process are some of the most concerning aspects.

The aim of this work is to develop a new substrate for wall-flow Diesel Particulate Filters based on a novel porous ceramic material: biomorphic silicon carbide (bioSiC). BioSiC is a particular type of silicon carbide obtained from the pyrolysis of wood and its subsequent infiltration with silicon. It is characterized by having a porous microstructure that replicates the cellular biological tissue of the wood precursor used for its manufacture. The main advantage of this material is the possibility of manipulating its microstructural features through the adequate selection of the precursor. With a suitable combination of porosity, pore size, and microstructural arrangement, the resulting filter could have enough filtration efficiency, with lower pressure drop, and better response to regeneration.

In the first part of this research work, bioSiC is characterized in terms of its suitability as substrate for particle filter. A filtration-focused characterization study was carried out in which the main physical and microstructural features involved in a proper behaviour in a particulate filter for automotive applications were measured. Up to five different wood precursors were chosen to make the laboratory bioSiC samples. In the case of natural woods, the anisotropy of the material was also taken into account; in this sense, the two possible cutting directions were considered and analyzed. As a result, measurements of density, porosity, pore size distribution, thermal expansion coefficient, thermal conductivity, compression strength, permeability and intrinsic filtration efficiency were provided for the nine bioSiC specimens.

The characterization study was complemented with a deeper study on the relationships between the different functional properties of bioSiC and its microstructure. Crucial parameters in the filtration performance of a DPF substrate such as permeability, thermal conductivity or compressive strength, were correlated with relevant microstructural features. The purpose of this analysis is to extrapolate the measurements obtained in this thesis with the nine selected specimens to any other bioSiC sample, and to foresee the potential of other wood precursors with different microstructure for their use as substrate in DPFs for the same application.

After selecting a suitable precursor for the target application, small bioSiC wall-flow DPF prototypes were manufactured. The chosen precursor was MDF. A complete and customized procedure for the manufacturing of these systems is proposed including the mechanization of the channels, the sticking of the sections, and the plugging of the channels. The resulting prototypes were tested at laboratory scale under real operating conditions similar to those produced by an internal combustion engine. Their performance in terms of efficiency and pressured drop was measured through accurate and repeatable tests.

Then, the experimental results were scaled up to a real-size MDF-bioSiC wall-flow DPF by means of a renowned and validated numerical model. A possible geometry was proposed for the full scale DPF in terms of length, diameter, cell density and wall-thickness, and it was simulated under real driving operating conditions, but implementing the physical and microstructural measured features of MDF-bioSiC in the definition of the substrate. The results were promising and encouraging. The resulting system widely complies with the current European standards in terms of number and mass of released particles. Furthermore, a comparative study was carried out with other commercial DPFs, and the results show that bioSiC DPFs may be clearly competitive in the aftertreatment systems industry for the automotive sector.

to my father

Acknowledgements

The present PhD Thesis presents a scientific work carried out in the University of Seville with the direct support of the Thermal Engines Research Group (Energy Engineering Department) and the Biomimetic and Multifunctional Materials Research Group (Condensed Matter Physics Department). This work is supported by the Spanish Ministry of Economy and Competitivity through a predoctoral grant (BES-2014-069023).

First of all, I would like to thank my supervisors, Prof. Ricardo Chacartegui and Prof. Julián Martínez, for giving me opportunity to carry out my PhD program, for their assistance and support. My deepest gratitude to Aurora Gómez for her invaluable contribution to this work, for her time, her ideas and her constant help. I am also indebted to Dr. José Antonio Becerra and to Dr. Joaquín Ramírez for their technical support, and all the things I learned from them in their respective fields of knowledge.

Within the project I would like to acknowledge Dr. Javier Quispe for his technical assistance, his ideas, and for maintaining all the infrastructure ready for testing. The competence of the mechanical technicians is also highly esteemed, in particular Juan Martín, Antonio Cañizares and José Luis Benjumea, who contributed to this work in many ways. I extend my gratitude to the rest of the FIL-BIO-DIESEL team, especially to Yolanda Sánchez for starting the project and pushing forward in the early stage.

I am fully grateful to Prof. Debora Fino for giving me the opportunity of spending a fruitful research stay at the Politecnico di Torino. My deepest gratitude also to Paolo Miceli and Francesco Matera for their support and kindness.

My special thanks to Dr. Onoufrios Haralampous for my stay at Larisa, his thorough work and direct supervision. I want to thank Dimitri for being so nice and helpful.

I gratefully acknowledge Prof. Hal Gurgenci for giving me the opportunity of spending some months working at the University of Queensland. I extend my gratitude to Dr. Kamel Hooman for his technical supervision. Thanks to my UQ coleagues, Fadhilah, Mostafa and Iman for their support.

I would like to thank Prof. Francisco J. Espadafor and Javier Serrano, colleagues of the Department, for the experiments in the engine bench at the Laboratory of Thermal Engines. I also appreciate the help of the administration staff: Mª Salu, María José, Silvia and Lourdes for making the most difficult part of the work. To those I worked with within the Energy Department and within the Biomimetic Materials Department; I thank them for the good teamwork, the coffee breaks, and for providing a lovely working environment.

With the permission of the reader, I would like to write the most personal acknowledgements in Spanish. Quiero dar las gracias a las personas que dan valor a mi vida, independientemente de lo que pase con esta Tesis, ya que sin ellos no hubiera sido capaz de llegar hasta aquí.

Gracias a Edu, mi pareja y mi compañero en la vida, por su cariño incondicional y por compartir todo conmigo en los momentos buenos y en los malos. Gracias a mis hermanos María del Socorro, Felipe y Luis. Gracias mis tíos, mis primos, mis sobrinos y al resto de mi pequeña pero unida familia. Gracias a mis amigas por poner la chispa y el toque de locura. Y por último, pero por encima de todo, gracias a mi padre, quien me contagió el interés por la investigación, quien me da los mejores consejos, y quien ha creído siempre en mí, incondicionalmente, dándome el valor y el ánimo para enfrentarme a los mayores retos.

Contents

Abstract 3
Acknowledgements 7
Contents 9
List of abbreviations 13
Notation 15
List of tables 19
List of figures 21

Chapter 1. Introduction

1.1. Background 25
1.2. Aim and objectives of the study 27
1.3. Scope 28
1.4. Outline of the Thesis 29
1.5. List of publications supporting this Thesis 31

Chapter 2. Review of the state of the art on automotive Diesel Particulate Filters

2.1. Particulate emissions of diesel engines 36
2.2. Overview of the filtration process in DPFs 37
2.3. Aftertreatment systems for the abatement of PM 39
2.3.1. Diesel Particulate Filters (DPF) 40
2.3.2. Design conditions depending on the application 44
2.4. Wall-flow Diesel Particulate Filters (wall-flow DPFs) 47
2.4.1. Geometric configurations of wall-flow DPFs 48
2.4.2. Materials commonly used in wall-flow DPFs 53
2.4.3. Microstructural characterization 56
2.5. DPF performance parameters 58
2.5.1. Filtration efficiency 62
2.5.2. Pressure drop 66
2.6. Regeneration process in a DPF 70
2.7. Motivations, research opportunities and expected contribution 72

Chapter 3. Materials and methods

3.1. Standard manufacturing process of bioSiC elements 84
3.2. Laboratory scale disk-shaped samples 86

3.3. Characterization techniques 91
3.3.1. Microstructural characterization 92
3.3.2. Thermal and mechanical characterization 93
3.3.3. Phase and TGA-DSC analysis 96
3.3.4. Permeability and intrinsic filtration efficiency 98
3.4. Small-scale prototypes of wall-flow DPFs made of bioSiC 103
3.5. Experimental measurement of filtration efficiency and pressure drop 108
3.6. Numerical model 111
3.6.1. Model description 111
3.6.2. Model calibration for a bioSiC DPF 115
3.6.3. Extrapolation to a full-size DPF 118
3.7. Summary of the methodology 120

Chapter 4. Microstructural and physical characterization of biomorphic Silicon Carbide

4.1. Microstructural characterization 126
4.1.1. Density based porosity 130
4.1.2. Porosity and pore size distribution 131
4.1.3. Specific surface 132
4.2. Thermal and mechanical characterization 134
4.2.1. Thermal expansion coefficient 134
4.2.2. Thermal conductivity 135
4.2.3. Compressive strength 136
4.3. Phase and TGA-DSC analysis 139
4.3.1. X-ray diffraction 139
4.3.2. TGA (Thermogravimetry) + DSC (Differential Scanning Calorimetry) analysis 140
4.4. Permeability and intrinsic filtration efficiency 141
4.4.1. Permeability 142
4.4.2. Intrinsic filtration efficiency 143
4.5. Summary of microstructural, physical and chemical parameters of the studied bioSiC specimens 150

Chapter 5. General applicability of bioSiC as filter material

5.1. Permeability dependency on the microstructure 156
5.2. Relationship between intrinsic filtration efficiency and permeability 162
5.3. Contribution of viscous and inertial effects to total pressure drop 164
5.4. Thermal conductivity dependence on the microstructure 166
5.5. Mechanical strength dependency on density 171
5.6. Applicability as filter material 173
5.7. Economic considerations 174
5.8. Conclusions 175

Chapter 6. Filtration performance of wall-flow MDF-bioSiC DPFs

6.1. Introduction 182
6.2. Experimental results with the bioSiC DPF prototypes 183
6.2.1. Preliminary blank tests 183
6.2.2. Characterization of the soot generator 184
6.2.3. Filtration efficiency 186
6.2.4. Pressure drop 187
6.2.5. Preliminary estimation of the performance during the soot load 188
6.2.6. Active regeneration of the filter 190
6.3. Results of the numerical simulation 191
6.3.1. Filtration efficiency and pressure drop of a full-size MDF-bioSiC DPF 193
6.3.2. Behaviour under a New European Driving Cycle (NEDC) 193
6.3.3. Potential of bioSiC wall-flow DPFs. Comparison with other commercial filters 196
6.4. Summary: potential of wall-flow MDF-bioSiC DPFs 203

Chapter 7. Conclusions and future work

7.1. Main contributions 207
7.2. Main research conclusions 208
7.3. Future works 210

List of abbreviations

AA	Axial Ayous
ACM	Acicular Mullite
ACT	Asymmetric Cell Technology
AF	Alloy foam
AP	Axial Pine
AI	Axial Iroko
AO	Axial Oak
AT	Aluminum Titanate
bioSiC	Biomorphic Silicon Carbide
BET	Brunauer, Emmett and Teller
BSE	Backscattered electron
cc	Cubic centimetres
cfm	Cubic feet per minute
CNC	Computer Numerical Control
CPC	Condensation Particle Sizer
cpsi	Cells per square inch
cpsc	Cells per square centimeter
CR	Commission Regulation
CTE	Thermal Expansion Coefficient
DMA	Differential Mobility Analyzer
DOC	Diesel Oxidation Catalyst
DPF	Diesel Particulate Filter
DSC	Differential Scanning Calorimetry
ECU	Engine Control Unit
EEA	European Environment Agency
EGR	Exhaust Gas Recirculation
EMEP	European Monitoring and Evaluation Programme
FCC	Face Centred Cubic
HC	Hydrocarbons
LPM	Litres per minute
MDF	Medium Density Fibreboard
MSA	Minimum solid area
NEDC	New European Driving Cycle
OPS	Optical Particle Sizer
PM	Particulate Matter
RA	Radial Ayous
RP	Radial Pine

RI	Radial Iroko
RO	Radial Oak
SE	Secondary electron
SEM	Scanning Electron Microscopy
SG	Soot generator
SMPS	Scanning Mobility Particle Sizer
SOF	Soluble Organic Fraction
STP	Standard temperature and pressure
TGA	Thermogravimetry Analysis
TW	Thin Wall
XCT	X-ray Computed Tomography
XRD	X-ray Diffraction
W/O	Without

Notation

α	Thermal diffusivity	$m^2 s$
$b(w)$	Effective width	m
C_E	Forchheimer's coefficient	m^{-1}
C_p	Specific heat	$J \cdot m^{-1} K^{-1}$
C_r	Parameter in the direct interception efficiency	-
d	Diameter	m
d_0	Primary particle diameter	m
D_f	Fractal dimension	-
D_p	Particle diameter	m
D_{part}	Particle diffusion coefficient	$m^2 \cdot s^{-1}$
ΔP	Pressure drop	Pa
ε	Porosity	-
F_0	Forchheimer's number	-
k	Thermal conductivity	$W \cdot m^{-1} K^{-1}$
k_1	Darcian (inertial) permeability	m^2
k_2	Viscous permeability	m
k_p	Inertial permeability of the soot layer	m^2
k_w	Inertial permeability of the substrate	m^2
Kn	Knudsen number	-
Ku	Kubawara's hydrodynamic factor	-
L	Length	m
Lmd	Logarithmic mean diameter	m
λ	Wavelength	m
M	Molecular mass	kg·mol
m	Mass	kg
N	Number	-
nPe	Exponent of Peclet number	-
η	Dynamic viscosity	Pa·s
η_D	Diffusional filtration efficiency	-

η_m	Mass filtration efficiency	-
η_N	Number filtration efficiency	-
η_R	Interception filtration efficiency	-
P	Pressure	Pa
P_0	Saturation pressure	Pa
Pe	Peclet number	-
Q	Volume flow rate	$m^3 \cdot s^{-1}$
q	Volume flow rate per unit area (velocity)	$m \cdot s^{-1}$
R	Interception parameter	
R_c	Maximum radius of the cluster	m
r_0	Primary particle radius	m
r_p	Particle radius	m
$\Re$	Gases constant	$J \cdot mol^{-1}K^{-1}$
Re	Reynolds number	
ρ	Density	$kg \cdot m^{-3}$
ρ_0	Primary particle density	$kg \cdot m^{-3}$
ρ_d	Effective density	$kg \cdot m^{-3}$
S	Surface	m^2
σ	Surface tension and compressive strength	$N \cdot m^{-1}$ and Pa
t	Time	s
T	Temperature	K
θ	angle	rad
v	Velocity	$m \cdot s^{-1}$
v_i	Interstitial fluid velocity	$m \cdot s^{-1}$
V	volume	m^3
w	Thickness/Intralayer dimension	m
z	Axial dimension	m

Subscripts

0	initial/clean state
ads	adsorbate
b	boiler
c	convection
d	downstream

e	effective
ε	pores
g	gas
fib	fibre
i	initial/input
m	mobility
o	output
p	particle/soot layer
r	radiation
ret	retained
s	solid
u	upstream
v	volume
w	Substrate/wall

List of tables

Table 2.1. Estimated utilization of filter materials for hot gas or exhaust cleaning 40
Table 2.2. DPF design requirements for different applications 45
Table 2.3. Summary of several DPF configurations used as samples in different tests as they appear in the bibliography 49
Table 2.4. Thermal and mechanical properties of the main materials used as substrate in wall-flow DPFs. 54
Table 2.5. Initial pressure drop and efficiency of several DPF described in the bibliography 59
Table 2.6. Some diesel engines used for DPFs testing 61
Table 2.7. Active regeneration measures 70
Table 2.8. Passive regeneration measures 71

Table 3.1. Samples identification nomenclature 90
Table 3.2. Technical specifications of the boiler 101
Table 3.3. Technical specifications of the optical particle sizer 103
Table 3.4. Geometrical specifications of the prototypes 108
Table 3.5. Summary of the experimental procedure 110
Table 3.6. Summary of the governing equations of the flux in the single channel volume control 113
Table 3.7. Single collector filtration efficiency by diffusion and interception for fibre unit collectors 115
Table 3.8. Parameters setting in the theoretical model of the small prototypes 116
Table 3.9. Parameters setting in the theoretical model of a real-scale bioSiC filter 119

Table 4.1. Bulk density, real density and density-based porosity of the bioSiC samples 130
Table 4.2. Porosities and pore size ranges of the bioSiC samples 131
Table 4.3. Specific surface of the bioSiC samples 133
Table 4.4. Thermal conductivity of the bioSiC samples 136
Table 4.5. Maximum compressive strength of the bioSiC samples 138
Table 4.6. Permeability constants of the bioSiC samples 143
Table 4.7. Particle size arrangement in the OPS channels: diameter range, logarithmic mean diameter, and effective density samples 144
Table 4.8. Evolution of the average efficiency in the 5 cycles of the tests 149

Table 5.1. Initial (clean state) intrinsic efficiency of the bioSiC samples 162
Table 5.2. Forchheimer number range of the bioSiC samples for air-flow velocity ranging from 0.01 to 0.4 m/s 165
Table 5.3. Anisotropy coefficient β of the bioSiC samples at room temperature and 700 °C ... 170

Table 6.1. Thermal and mechanical properties of the bioSiC samples (evaluated at ambient temperature) affecting its thermal shock performance..... 182
Table 6.2. Correspondence between gas flow rate and darcian velocity..... 189
Table 6.3. Calibrated values of the empirical parameters of the numerical model..... 191
Table 6.4. Specifications of the vehicle whose performance..... 194
Table 6.5. Simulation parameters taken form the literature for different DPF examples..... 197
Table 6.6. Initial pressure drop of a bioSiC DPF compared to an equivalent commercial DPF..... 199
Table 6.7. Initial filtration efficiency of a bioSiC DPF compared to an equivalent commercial DPF..... 201

List of figures

Figure 2.1. Typical particle size distribution of diesel engine exhaust 36
Figure 2.2. Distribution of the soot layer thickness along the axial (left) and radial (right) direction 39
Figure 2.3. General scheme and operation principle of a wall-flow DPF 47
Figure 2.4. General appearance of a wall-flow filter as incorporated in a vehicle 47
Figure 2.5. Detail of a wall-flow filter showing the cell density and the wall thickness 48
Figure 2.6. Standard and asymmetric cell technology (ACT) designs 51
Figure 2.7. Bilayer channels technology, and its effect on the evolution of pressure drop with the soot load 52
Figure 2.8. Relationship between the amount of coating applied and the initial efficiency and pressure drop 52
Figure 2.9. Relation between bulk density and particle load leading to surpass the thermal limit to failure during regeneration process 57
Figure 2.10. Filtration efficiency of a high porosity SiC filter, with and without surface layer 62
Figure 2.11. Filtration efficiency and pressure drop for DPFs with filtration membrane 63
Figure 2.12. Effect of the mass flux of gases on the filter efficiency 63
Figure 2.13. Curves Efficiency-Soot load measured by different authors 64
Figure 2.14. Predicted clean filter efficiency sensitivity on porosity (left) and median pore diameter (right) 65
Figure 2.15. Filtration efficiency and pressure drop of wall-flow DPFs with different pore width 66
Figure 2.16. Curves Pressure drop-Soot load measured by different authors 68
Figure 2.17. Hysteresis cycle experienced by the pressure drop of a DPF with the particle loading level 69
Figure 2.18. Comparison between loading curves of a clean filter and loading curves of an identical but not completely regenerated filter 69
Figure 2.19. Evolution of pressure drop and temperature (in the inlet and outlet section) during a typical regeneration process 71

Figure 3.1. Scheme of the bioSiC manufacuting process 85
Figure 3.2. Pyrolyzation heating programme 88
Figure 3.3. Pyrolysis furnace on the left hand side. On the right hand side, inside view of the furnace with the carbon blocks obtained after the pyrolysis 88
Figure 3.4. Cutting of the carbon cylinders into disks in the precision slicing machine 89
Figure 3.5. Specimens inside the crucible before (left) and after (right) the infiltration process 89

Figure 3.6. High-temperature furnace used for the infiltration and the evaporation processes 90
Figure 3.7. Final aspect of the Oak samples: AO (left) and RO (right)..... 90
Figure 3.8. Laboratory-made permeameter built for this work 99
Figure 3.9. Design sketch of the sample carrier and operating diagram of the permeameter 99
Figure 3.10. Test bench layout for the measurement of the intrinsic filtration efficiency of the lab-scale bioSiC samples 101
Figure 3.11. Experimental facility for the preliminary measurement of the filtration efficiency: diesel boiler (left) and test rig (right). 102
Figure 3.12. Attachment of the thermocouple (K-TC) and the fan to the heat exchanger 102
Figure 3.13. Main stages of the manufacturing process of bioSiC..... 105
Figure 3.14. One of the mechanized slices (left) and final aspect of the whole prototypes before the infiltration with silicon 106
Figure 3.15. Carbon slices of the prototype in the crucible covered with silicon..... 106
Figure 3.16. Three-dimensional rendering of the XCT analysis carried out over the wall-flow bioSiC filter prototype 107
Figure 3.17. Test bench layout..... 109
Figure 3.18. Photograph of the test bench 109
Figure 3.19. Final aspect of the samples in the cordierite adaptor (left) and fitting of the samples inside the canning (right)..... 110
Figure 3.20. Front area of the control volume in the "single channel problem" represented over a SEM image of a real MDF-bioSiC wall-flow filter 112
Figure 3.21. Scheme of the channel with geometrical definitions used in the model 113
Figure 3.22. Real particle size distribution of the soot generator and modelled curve..... 117

Figure 4.1. SEM images of the carbon matrix obtained from the pyrolysis of MDF..... 126
Figure 4.2. SEM images of the carbon matrixes obtained from the pyrolysis of natural woods..... 127
Figure 4.3. SEM image of the MDF-bioSiC specimen..... 128
Figure 4.4. SEM images of the bioSiC specimens (axial samples) 128
Figure 4.5. SEM images of the bioSiC specimens (radial samples)..... 129
Figure 4.6. Pore size distributions of bioSiC specimens from different wood precursors 131
Figure 4.7. Adsorption isotherm curves of bioSiC specimens from different wood precursors..... 132
Figure 4.8. Thermal expansion coefficient of bioSiC specimens from different wood precursors..... 134
Figure 4.9. Thermal diffusivity of bioSiC specimens from different wood precursors..... 135
Figure 4.10. Thermal conductivity of bioSiC specimens from different wood precursors 136
Figure 4.11. Stress-strain curves from compressive-strength tests of two bioSiC specimens: MDF and Axial Oak..... 137
Figure 4.12. Compressive fractography of bioSiC specimens from different wood precursors..... 137

Figure 4.13. X-ray diffraction patterns of an MDF-bioSiC specimen before and after residual Si removal by capillary extraction at high temperature 139
Figure 4.14. TGA analysis of bioSiC specimens from different wood precursors 140
Figure 4.15. Percentage of residual carbon in the samples after the infiltration process versus porosity 141
Figure 4.16. Pressure drop per unit of length as a function of air-flow velocity of bioSiC specimens from different wood precursors 142
Figure 4.17. Number of particles measured downstream the filter samples during boiler's first cycle. (a) Axial samples (b) Radial samples 146
Figure 4.18. Number of particles measured downstream the axial filter samples along five full cycles of operation of the boiler 147
Figure 4.19. Efficiency evolution, averaged every 150 s, during boiler's first cycle, (a) Axial samples (b) Radial samples..... 147
Figure 4.20. Efficiency evolution, averaged every 120 s, along the whole test, (a) Axial samples (b) Radial samples..... 148
Figure 4.21. Efficiency evolution with soot load, averaged every 120 s, along the whole test, (a) Axial samples (b) Radial samples 149
Figure 4.22. Evolution of the filtration efficiency with the soot load (a) Axial samples (b) Radial samples..... 150
Figure 4.23. SEM micrographs taken after the tests of two soot loaded samples (a) BioSiC from axial Iroko (b) BioSiC from axial Ayous 150
Figure 4.24. Summary of microstructural, physical and chemical parameters of the studied bioSiC specimens..... 152

Figure 5.1. Permeability vs. effective pore size for bioSiC samples from different precursors in two orientations 159
Figure 5.2. Specific surface area per unit volume calculated from the pore size distribution vs. S_v measured from Kr adsorption 160
Figure 5.3. A) Viscous permeability k1 vs. εd2 and B) inertial permeability k2 vs. ε2d as dictated by Ergun's relationships, in both axial and radial directions..... 161
Figure 5.4. Initial efficiency of the bioSiC samples as a function of: a) the most likely pore size, and b) the maximum pore size 163
Figure 5.5. Dependence of bioSiC filtration efficiency on the permeability..... 164
Figure 5.6. Viscous and inertial terms of the bioSiC samples as a percentage of total pressure drop, as a function of air-flow velocity..... 166
Figure 5.7. Effective thermal conductivity of the bioSiC samples as a function of porosity..... 168
Figure 5.8. Schematic depiction of the relation between heat flux direction and microstructure in: a) radial and b) axial orientations..... 170
Figure 5.9. (A) Maximum compressive strength at room temperature as a function of density and (B) relative strength as a function of relative density of the bioSiC specimens 172
Figure 5.10. Classification of filter materials according to permeability values from the literature including experimental data from this work 173

Figure 6.1. Estimated Thermal Shock Resistance and Specific Heat of bioSiC ceramics compared to other commercial ceramics 183
Figure 6.2. Normalized particle size distribution of the soot generator Palas GFG 1000 and comparison with the distribution in the exhaust of different engines 185
Figure 6.3. Filtration efficiency of the wall-flow bioSiC DPF prototypes..... 186
Figure 6.4. Filtration efficiency of the wall-flow bioSiC DPF prototypes as a function of the particle diameter in two different moments: t=0s, and t=1800s 187
Figure 6.5. Pressure drop of the wall-flow bioSiC DPF prototypes..... 188
Figure 6.6. Filtration efficiency and normalized pressure drop of the wall-flow bioSiC DPF prototypes as a function of the estimated soot load 189
Figure 6.7. Evolution in the temperature and the non-dimensional pressure drop during the regeneration process 190
Figure 6.8. Evolution of the pressure drop of the small wall-flow bioSiC DPF prototype with the soot load 192
Figure 6.9. Evolution of the filtration efficiency of the small wall-flow bioSiC DPF prototype with the time 192
Figure 6.10. Expected performance of a full-size wall-flow bioSiC DPF; pressure drop on the left hand side; filtration efficiency on the right hand side..... 193
Figure 6.11. Speed evolution in a NEDC 194
Figure 6.12. Simulated pressure drop and particles emissions during a NEDC cycle with an MDF-bioSiC wall-flow DPF..... 195
Figure 6.13. Initial pressure drop of a bioSiC DPF compared to a number of commercial DPFs..... 200
Figure 6.14. Transient evolution of the pressure drop of a bioSiC DPF compared to a similar commercial DPF 202

Chapter 1
Introduction

This thesis deals with the use of biomorphic Silicon Carbide (bioSiC) as substrate for wall-flow Diesel Particulate Filters (DPF). This thesis has been developed within the project *Bio-ceramics for diesel engine particulate filters* (FIL-BIO-DIESEL), a three-years-long project supported by the Spanish *Ministerio de Economía y Competitividad* and by the European Regional Development Fund (ERDF). The project addresses the issue of sustainable transport by developing a regenerative particulate filter for diesel engines based on a new generation of bio-derived ceramic materials.

In this first Chapter, the main objectives of the thesis are presented, the scope of the study is demarcated, and the whole structure of the document is explained.

1.1. Background

Emission levels for new automotive engines are submitted to increasingly stringent limits. The European Monitoring and Evaluation Programme (EMEP) estimates at 1897 Gg the total emissions of particles smaller than 10 microns (PM_{10}) that were emitted in 2015 in the European Union, of which approximately 205 Gg, an 11%, are associated with the road transport sector [1]. While particulate emissions PM_{10} have been reduced by around 25% between 2000 and 2015 (>35% since 1990), current emission levels are still not sufficient to meet the limit of 40 mg/m^3 of annual mean concentration [2] that dictates the European Directive 2008/50/EC on air quality [3]. Thus, the European Union continues to maintain and narrow the emission thresholds for automotive engines, particularly for diesel engines, which are the ones that emit the most particles.

From September 2015, all new European diesel cars must be compliant with the Euro 6 emission standards, which set a particle number emission limit of 6×10^{11} particles/km and a limit of 4,5 mg/km for the mass of particulate. In the short future new standards will be developed for even stricter emissions. Developments in the design of the engines contribute to lessen particle emissions, but they are no longer sufficient to ensure compliance of these

thresholds. Therefore, the use of more efficient Diesel Particle Filters is becoming increasingly necessary in diesel vehicles.

Nowadays, the most popular aftertreatment system for the abatement of particulate emissions in diesel engines is the wall-flow Diesel Particulate Filter (wall-flow DPF). Given their well-known filtration efficiency and their potential to meet more and more strict emission standards [4], wall-flow DPFs have the longest track record in the market. The main drawbacks of current wall-flow DPFs are the high backpressure they introduce in the exhaust pipe, and the technical issues associated with the on-board regeneration process. The backpressure induced by the system increases the mechanical losses, the fuel consumption, and the CO_2 emissions [5]. Therefore, reducing the pressure drop of the particulate filters is a recurring objective in current research in the field of DPFs. On the other hand, the quick saturation of the filter, and the difficulties that many drivers experience to achieve its regeneration (if they make only short drives, or they don't usually drive on highways), are becoming a problem for some users, some of which decide to dispend with it after a short period of use.

For these reasons, the search of new materials that could improve permeability, thermal properties and filtration performance of Diesel Particulate Filters is a current topic, boosted among scientists in the recent time. The development and optimization of particulate filters is certainly one the biggest matters of concern in the field of sustainable transport, as the number of annually registered patents evidences.

The behaviour of a wall-flow DPF is given by its geometry (diameter, length, wall thickness, cell density) at the macroscopic scale [6], and by the properties of the material used as substrate (permeability, porosity, pore size, tortuosity) at the microscopic scale [7]. For a given geometry, the microstructural properties of the substrate define the filtration efficiency and the pressure drop of the filter. The problem is that filtration efficiency and pressure drop are generally closely related; an increase in filtration efficiency brings an increase in pressure drop and vice versa. One of the main challenges nowadays is designing substrates that reduce the pressure drop without penalizing the filtration efficiency.

On the other hand, filters should have a proper regeneration behaviour. A slow regeneration process (low combustion velocity) would be safer for the filter but would entail a higher penalty in fuel consumption. The most common way of regenerating the filter is through the *drop-to-idle* process. This process involves rapidly reducing the gas flux just after starting the regeneration, so that a peak of temperature is induced and the soot combustion is accelerated. The problem is that this process produces a high thermal stress in the material which, in some cases, may lead to crack formation and its eventual collapse [8]. A possible way to alleviate this problem is using a porous substrate with higher susceptibility to regeneration, that is, a substrate capable of inducing the soot combustion at a lower temperature.

Possible candidate materials for being used as DPF substrate must fulfil the following requirements: high filtration efficiency, low pressure drop, high thermal and chemical stability,

and high capability to resist the severe and frequent heating cycles associated to the regeneration processes [9]. In that sense, currently, the majority of the DPFs are made with substrates of Cordierite ($2MgO{\cdot}2Al_2O_3{\cdot}5SiO_2$) and Silicon Carbide (SiC); and, in a few cases, they may also be made of Mullite (ACM, Al_2SiO_5), Aluminum Titanate (AT, Al_2TiO_5), and alloy foams (AF) [10]. Silicon carbide is one of the most reliable materials used as substrate [11]. It presents some advantages and disadvantages [12]: on the one hand, during the regeneration, silicon carbide presents lower temperature peaks for the same soot load, which leads to a higher soot limit; while on the other hand, it has higher thermal losses, which may reduce the thermal levels and, hence, the efficiency of selective catalytic reduction systems.

Biomorphic Silicon Carbide (bioSiC) is a particular type of silicon carbide obtained from the pyrolysis of wood and its subsequent infiltration with silicon. It is characterized by having a porous microstructure that replicates the cellular biological tissue of the wood precursor used for its manufacture. The main advantage of this material is the possibility of manipulating its microstructural features through the adequate selection of the precursor. With a suitable combination of porosity, pore size, and microstructural arrangement, the resulting filter could have enough filtration efficiency with lower pressure drop, and better response to regeneration.

Some recent studies have demonstrated that bioSiC has real potential to be used in high temperature gas filtration applications [13,14]. BioSiC may have permeabilities of around 10^{-11}–10^{-12} m^2 [15], and thermal conductivities in the range of 4-88 W/mK [16]. Besides, the manufacturing process of bioSiC [17] differs considerably from that of other granular ceramic materials [18]. According to De Arellano-López et al. [19] and Singh et al. [20], bioSiC is a low-cost, environmentally friendly material. For all these reasons, the possibility of developing a bioSiC-DPF is an attractive research topic and an appropriate response to the needs of the automotive market.

1.2. Aim and objectives of the study

This research work is aimed at exploring the possibility of using biomorphic Silicon carbide as substrate for Diesel Particulate Filters. The main goal of this thesis is to afford a final overview of the potential of this novel material to be used as substrate in wall-flow DPFs. Accordingly, the initial proposal includes two main objectives:

First of all, bioSiC material is characterized as automotive DPF substrate. On this purpose, a review on the main specifications of current aftertreatment systems is conducted, so that a first approach to the physical and microstructural requirements of a possible wood precursor can be made. Then, a number of precursors are chosen and a comprehensive characterization study on their properties is carried out. The characterization study shall include the most influencing properties in the functional performance of a DPF, which are porosity, pore size, permeability, thermal expansion coefficient, thermal conductivity and compressive strength. The results should allow to make a decision on the most suitable precursor for the considered application.

The second objective is manufacturing a real bioSiC wall-flow DPF prototype and evaluating its potential for automotive applications. This implies setting the manufacturing process and testing the prototype under real conditions. For this purpose, the general manufacturing process of bioSiC will be adjusted and optimized. The substrate will be made of the most suitable candidate among the characterized precursors. Filtration tests on the prototype shall measure two main parameters: filtration efficiency (capability of retaining particles) and exhaust back-pressure, under real operating conditions (exhaust gas composition, mass flow, temperature, particle size distribution). The tests shall offer measurements for the clean state and also for the transient soot-loading process.

The obtained results will be used to stablish a comparison with the state of the art in automotive DPFs. Numeric simulation tools will be used to extrapolate the results of the experimental campaign to the diversity of configurations and operating conditions found in the literature. Practical conclusions shall be obtained that allow to predict the performance of other precursors based on their microstructural characteristics, and that provide a criterion for selecting an optimal wood precursor for the application.

1.3. Scope

This thesis revolves around biomorphic Silicon Carbide as an alternative substrate for DPFs. It takes into consideration the influence of the vegetal precursor in the final properties of the material, and so it starts with the selection of several wood candidates covering a wide range of densities and microstructural arrangements to later determine the most desirable properties for the application under study.

The general fabrication process for bioSiC has been recurrently described in the literature with different nuances. It consists mainly of three stages: pyrolysis, silicon infiltration, and excess silicon removal. In this work, stages one and two have been applied as previously reported by other authors; but the third stage has been applied with a substantial modification. In this case, the excess silicon has been removed by evaporation at high temperature, instead of by chemical etching with acids, which is considered an improvement in terms of safety and efficacy. As a result, slight differences in the final properties of the material may be obtained, but they are not expected to affect negatively its performance for the application under study.

This thesis is focused on the filtration performance of the bioceramic filters from a physical point of view; that is, through the physical interactions between the porous ceramic substrate and the soot particles. Since these interactions take place at the micro and nano-scale, the characterization study is focused on two main aspects: the microstructural features of the material, and the physical aspects that characterize the interaction substrate-particle at the pore-scale. The characterization techniques were selected accordingly. The microstructural characterization is made through the measurement of the density, the porosity and the pore size

distribution. The physical characterization is focused mainly on the measurement of the permeability and the intrinsic filtration efficiency of the porous substrate, which are the most influential parameters on the behaviour of a filter. However, other aspects such as the thermal conductivity, the thermal expansion coefficient, and the mechanical strength, are also measured since they directly affect the regeneration behaviour of an automotive DPF.

The particular geometry of wall-flow DPFs affects its filtration performance as much as its substrate does. Length, cell density, or wall thickness, are some of the geometrical aspects that may significantly influence the pressure drop or the efficiency of a DPF. In this thesis, the potential of a bioSiC wall-flow DPF for automotive applications is studied through the manufacture and testing of a real prototype, the geometrical design of which is set in advance based on the current trends. That is, the prototype design was unique and carefully made paying attention to the most influential aspects (cell density and wall thickness). The length and the front area of the prototype were adjusted to fit the sample-carrier of the test rig. As a result, the resulting prototype was smaller than a real DPF, so it was later scaled up through computational techniques.

The bioSiC wall-flow DPF prototype was tested at lab-scale with the aid of a soot generator. Through this device, operating conditions similar to those of a real diesel exhaust were simulated in terms of mass flow and particle size distribution. Besides, the prototype was studied in both the clean state and during the soot load. The testing conditions were controlled and repeatable, so that they could be easily implemented in the numerical model to validate the results and to scale up the system to a real-size DPF. This allows to simulate the performance of the bioSiC wall-flow DPF under any operating conditions; and, in particular, under standard European driving cycles (NEDC) to predict its particle abatement potential for current and future emissions regulations.

1.4. Outline of the Thesis

This thesis is structured in seven main chapters, the contents of which are summarized below.

Chapter 2. Review of the state of the art on automotive Diesel Particulate Filters.

As stated in its title, this chapter intends to serve as a background for the rest of the text. The main topics appraised in this introductory chapter are: a description of the particulate emissions produced by diesel engines, an overview of the filtration process in DPFs, a broad revision of the state-of-the-art in aftertreatment systems for the abatement of particles in diesel vehicles, an exhaustive description of the wall-flow DPF and its main physical and microstructural features, and an in-depth review on the most recent studies about efficiency and pressure drop in these particular filtration systems. At the end of Chapter 2, the possibilities that the current state of the art offers are summarized as motivations for the development of this thesis, and the main sought contributions to the development of the sector are presented.

Chapter 3. Materials and methods.

Chapter 3 sets the bases of this thesis in several well-differentiated parts. In the first part, the selection criteria for the wood precursors is stated, and a description of the laboratory samples and their manufacturing procedure is provided. Then, Section 3.3 describes in detail the basic working principles of all the characterization techniques used in this work. The second part of the chapter is devoted to the final prototype and the main experimental campaign. In Section 3.4 the procedure developed for manufacturing bioSiC wall-flow filters is described. Then the experimental work carried out to determine the filtration performance of the prototype is described in Section 3.5. And finally, the last section of the chapter is focused on the numerical tools used to model the bioSiC filter, and to extrapolate the experimental results to any hypothetical situation that allows to compare with other filters.

For the sake of clarity, the results of this thesis are structured in three chapters. Chapters 4 and 5 present the measurements and results down to the material level obtained from the lab-scale samples. While Chapter 6 presents the results at a system level obtained with the prototype.

Chapter 4. Microstructural and physical characterization of biomorphic Silicon Carbide.

Chapter 4 presents the main results of the material characterization study, including all the representative data obtained through each technique. All results presented in this chapter correspond to the lab-scale samples that were manufactured during the first part of the research. The results are structured into four main sections according to the purpose of the employed characterization technique. In the first section, Section 4.1, the results of the microstructural study are presented. Section 4.2 is focused on the physical properties (thermal and mechanical). The third section presents additional measurements that were made to detect possible deviations in the material from the sought composition. And finally, in Section 4.4, measurements on the permeability and the intrinsic filtration efficiency of the specimens are presented as specific parameters for an optimal filtration performance.

Chapter 5. General applicability of bioSiC as filter material.

In Chapter 5, the results of the characterization study presented in Chapter 4 are analysed in detail in order to draw significant relationships between different functional parameters. The purpose of this chapter is to predict the potential of other types of bioSiC made with other wood precursors for their use as substrate in any particle filtration application, and especially in automotive DPFs.

Chapter 6. Filtration performance of wall-flow MDF-bioSiC DPFs.

Chapter 6 deals with the results of the experimental campaign with the prototypes, and with the results of the numerical study. It is divided into two main sections. In Section 6.2 the

measurements on filtration efficiency and pressure drop of the bioSiC wall-flow prototypes are presented, while Section 6.3 presents the results of applying the numerical model to the biomorphic filter. This section gathers some of the most representative results about the filter system in global terms, and stablishes the competitiveness of bioSiC wall-flow DPFs within the aftertreatment systems market.

Chapter 7. Conclusions and future work.

Finally, in the last chapter, the main contributions of the thesis are presented, the main conclusions of the research are summarized, and some possible future research lines are presented.

1.5. List of publications supporting this Thesis

The following papers are derived from this thesis. They are original and fully developed by the author and her co-authors during the research period associated to the development of the same. The author has express authorization by all her co-authors to use their content as part of this thesis, which was certainly used recurrently along the text to present results and considerations. References to the referred papers are included where applicable.

Papers in indexed journals

1. M.P. Orihuela, R. Chacartegui, A. Gómez-Martín, J. Ramírez-Rico, J.A. Becerra-Villanueva. *Current trends in wall-flow Diesel Particulate Filters*. Journal of hazardous materials (under review)

2. A. Gómez-Martín, M.P. Orihuela, J.A. Becerra-Villanueva, J. Martínez-Fernández, J. Ramírez-Rico. *Permeability and mechanical integrity of porous biomorphic SiC ceramics for application as hot-gas filters*. Materials & Design, Vol. 107, 450–460, 2016.
   doi: 10.1016/j.matdes.2016.06.060

3. A. Gómez-Martín, M.P. Orihuela, J. Ramírez-Rico, R. Chacartegui, J. Martínez-Fernández. *Thermal conductivity of porous biomorphic SiC derived from wood precursors*. Ceramics International, Vol. 42, Iss. 14, 16220–16229, 2016.
   doi: 10.1016/j.ceramint.2016.07.151

4. M.P. Orihuela, A. Gómez-Martín, J.A. Becerra-Villanueva, R. Chacartegui, J. Ramírez-Rico. *Performance of biomorphic Silicon carbide as particulate filter in diesel boilers*. Journal of Environmental Management, Vol. 203, Iss. 3, 907-919, 2017.
   doi: 10.1016/j.jenvman.2017.05.003

5. M.P. Orihuela, A. Gómez-Martín, P. Miceli, J.A. Becerra-Villanueva, R. Chacartegui, D. Fino. *Experimental measurement of the filtration efficiency and pressure drop of wall-flow Diesel Particulate Filters (DPF) made of biomorphic Silicon Carbide using laboratory generated particles*. Applied Thermal Engineering, Vol. 131, 41-53, 2018.
doi: 10.1016/j.applthermaleng.2017.11.149

6. M.P. Orihuela, F. Shikh Anuar, I. Ashtiani Abdi, M. Odabaee, K. Hooman. *Thermohydraulics of a metal foam-filled annulus*. International Journal of Heat and Mass Transfer, Vol. 117, 95-106, 2018.
doi: 10.1016/j.ijheatmasstransfer.2017.10.009

7. M.P. Orihuela, O. Haralampous, R. Chacartegui, J. Martínez. *Numerical simulation of a wall-flow Diesel Particulate Filter made of biomorphic Silicon Carbide*. SAE international (under review)

Participation in international conferences

1. Y. Sánchez Salinas; M.P. Orihuela; J. Ramírez-Rico; J.A. Becerra-Villanueva; J. Martínez-Fernández. *Biomorphic porous SiC ceramics as filtering elements in Diesel Particulate Filters* (Poster). 14th International Conference of the European Ceramic Society (ECERS 2015). Toledo, 2015.

2. M.P. Orihuela, A. Gómez-Martín, J. Ramírez-Rico, J. Martínez-Fernández, R. Chacartegui. *Assessment of the suitability of bioSiC as substrate of DPFs* (Oral presentation). FEMS Junior Euromat. Lausanne, 2016.

3. A. Gómez-Martín, M.P. Orihuela, J. Martínez-Fernández, J. A. Becerra, R. Chacartegui, J. Ramírez-Rico. *Thermal conductivity and permeability simulations based on X-ray tomography of porous biomorphic SiC* (Poster). European Materials Research Society (E-MRS) 2016 Fall Meeting. Warsaw, 2016.

4. M.P. Orihuela, A. Gómez-Martín, J.A. Becerra-Villanueva, R. Chacartegui, J. Ramírez-Rico. *Performance of biomorphic silicon carbide as particulate filter in a diesel boiler* (Oral presentation). 11th Conference on Sustainable Development of Energy, Water, and Environment Systems (SDEWES 2016). Lisbon, 2016.

5. M.P. Orihuela, A. Gómez-Martín, J.A. Becerra-Villanueva, J. Serrano-Reyes, F. Jiménez-Espadafor, R. Chacartegui. *Performance of biomorphic Silicon Carbide as substrate for DPF in an automotive diesel engine* (Oral presentation). 12th Conference on Sustainable Development of Energy, Water, and Environment Systems (SDEWES 2017). Dubrovnik, 2017.

Participation in national conferences

1. M.P. Orihuela. A. Gómez-Martín, J.A. Becerra-Villanueva, J. Ramírez-Rico, J. Martínez-Fernández. *Comportamiento del SiC biomórfico como filtro de partículas en motores diésel de automoción* (Oral presentation). LV Congreso Nacional de la Sociedad Española de Cerámica y Vidrio (SECV). Seville, 2016.

2. A. Gómez-Martín, M.P. Orihuela, J. Martínez-Fernández, J. A. Becerra, R. Chacartegui, J. Ramírez-Rico. *Evaluación de la viabilidad del carburo de silicio biomórfico para aplicaciones de filtrado a altas temperaturas* (Oral presentation). LV Congreso Nacional de la Sociedad Española de Cerámica y Vidrio (SECV). Seville, 2016.

3. A. Gómez-Martín, M.P. Orihuela, J. Martínez-Fernández, J. A. Becerra, R. Chacartegui, J. Ramírez-Rico. *Evaluación de la viabilidad del carburo de silicio biomórfico para aplicaciones de filtrado a altas temperaturas* (Oral presentation). V Jornadas de Jóvenes Investigadores del Instituto de Cerámico y Vidrio. Madrid, 2016.

References

[1] WebDab - EMEP database. EMEP/CEIP 2014 Present State Emiss Data 2015. http://www.ceip.at/webdab_emepdatabase/reported_emissiondata/.

[2] EEA. European Environment Agency. Air quality in Europe — 2017 report. Copenhagen (Denmark): 2017.

[3] Directive 2008/50/EC. Off J Eur Comm 2008;152:1–44.

[4] Guan B, Zhan R, Lin H, Huang Z. Review of the state-of-the-art of exhaust particulate filter technology in internal combustion engines. J Environ Manage 2015;154:225–58.

[5] Stamatelos AM. A review of the effect of particulate traps on the efficiency of vehicle diesel engines. Energy Convers Manag 1997;38:83–99. doi:10.1016/0196-8904(96)00011-8.

[6] Deng Y, Zheng W, Jiaqiang E, Zhang B, Zhao X, Zuo Q, et al. Influence of geometric characteristics of a diesel particulate filter on its behavior in equilibrium state. Appl Therm Eng 2017;123:61–73. doi:10.1016/j.applthermaleng.2017.05.071.

[7] Tandon P, Heibel A, Whitmore J, Kekre N, Chithapragada K. Measurement and prediction of filtration efficiency evolution of soot loaded diesel particulate filters. Chem Eng Sci 2010;65:4751–60. doi:10.1016/j.ces.2010.05.020.

[8] Benaicha F, Bencherif K, Sorine M, Vivalda JC. Model based mass soot observer of diesel particle filter. 18th IFAC World Congr., 2011, p. 10647–52.

[9] Millo F, Andreata M, Rafigh M, Mercuri D, Pozzi C. Impact on vehicle fuel economy of the soot loading on diesel particulate filters made of different substrate materials. Energy 2015;86:19–30. doi:10.1016/j.energy.2015.03.076.

[10] Konstandopoulos AG. Technology Evaluation Report for Diesel Engine After-Treatment System. 2013.

[11] Schaefer-Sindlinger A, Lappas I, Vogt CD, Ito T, Kurachi H, Makino M, et al. Efficient material design for diesel particulate filters. Top Catal 2007;42–43:307–17. doi:10.1007/s11244-007-0197-8.

[12] Andreata M, Millo F, Mallamo F, Mercuri D, Pozzi C. Experimental Investigation on Three Different Ceramic Substrate Materials for a Diesel Particulate Filter. SAE Tech Pap 2013;2013-24–01:1–11.

[13] Alonso-Fariñas B, Lupion M, Rodríguez-Galán M, Martínez-Fernández J. New candle prototype for hot gas filtration industrial applications. Fuel 2013;114:120–7. doi:10.1016/j.fuel.2012.12.054.

[14] Orihuela MP, Gómez-Martín A, Becerra-Villanueva JA, Ricardo C, Ramírez-Rico J. Performance of biomorphic silicon carbide as particulate filter in diesel boilers. J Environ Manage 2017;203:907–19. doi:10.1016/j.jenvman.2017.05.003.

[15] Gómez-Martín A, Orihuela MP, Becerra-Villanueva JA, Martínez-Fernández J, Ramírez-Rico J. Permeability and mechanical integrity of porous biomorphic SiC ceramics for application as hot-gas filters. Mater Des 2016;107:450–60. doi:10.1016/j.matdes.2016.06.060.

[16] Gómez-Martín A, Orihuela MP, Ramírez-Rico J, Chacartegui R, Martínez-Fernández J. Thermal conductivity of porous biomorphic SiC derived from wood precursors. Ceram Int 2016;42:16220–9. doi:10.1016/j.ceramint.2016.07.151.

[17] Bautista MA, De Arellano-López AR, Martínez-Fernández J, Bravo-León A, López-Cepero JM. Optimization of the fabrication process for medium density fiberboard (MDF)-based biomimetic SiC. Int J Refract Met Hard Mater 2009;27:431–7. doi:10.1016/j.ijrmhm.2008.10.016.

[18] Adler J. Ceramic Diesel Particulate Filters. Int J Appl Ceram Technol 2005;2:429–39. doi:10.1016/B978-0-12-385469-8.00032-0.

[19] De Arellano-López AR, Martínez-Fernández J, González P, Domínguez C, Fernández-Quero V, Singh M. Biomorphic SiC: A New Engineering Ceramic Material. Int J Appl Ceram Technol 2005;1:56–67.

[20] Singh M, Martínez-Fernández J, De Arellano-López AR. Environmentally conscious ceramics (ecoceramics) from natural wood precursors. Curr Opin Solid State Mater Sci 2003;7:247–54. doi:10.1016/j.cossms.2003.09.004.

Chapter 2
Review of the state of the art on automotive Diesel Particulate Filters

In this chapter the background and framework for the development of this thesis is provided. In this context, a review of the main trends in the design of modern wall-flow Diesel Particulate Filters (DPF) for automotive engines is presented, focusing mainly on the two main filtration parameters: the pressure drop and the filtration efficiency. There is plenty of literature on aftertreatment systems for diesel engines. In 2015, Guan et al. [1] published a comprehensive review of the state-of-the-art technology in diesel particles filtration, which sets out in detail all aspects of the DPFs: the diverse materials used as substrate, new catalyst formulations, regeneration control strategies, soot load prediction models, etc. Other review articles or books published earlier, but with information about DPFs just as complete and comprehensive are: Khair 2003 [2], Konstandopoulos 2008 [3], Prasad 2010 [4] or Somiya 2013 [5].

This thesis deals with the use of biomorphic Silicon Carbide (bioSiC) as substrate for wall-flow DPFs. Thus, this literature review will be specifically focused on the physical and microstructural description of current wall-flow DPFs. The chapter is structured as follows. First, Section 2.1 describes briefly the particulate emissions produced by diesel engines. In Section 2.2, an overview of the filtration process is presented. Section 2.3 presents an introduction to DPFs and provides a summary of the design conditions depending on the engine and its application. In Section 2.4, an in-depth physical description of wall-flow DPFs is provided. The most recent research activities in their development and improvement are summarized; and the main technological advances are presented. Section 2.5 gathers the main results and conclusions of the most recent studies about the efficiency and the pressure drop. These results taken from the state-of-the-art literature about DPFs were the starting point for the design of a bioSiC wall-flow DFP, and served as reference for the development of a competitive filtration system in the market. Finally, in Section 2.6, a quick review on the regeneration processes is presented.

Related publications

M.P. Orihuela, R. Chacartegui, A. Gómez-Martín, J. Ramírez-Rico, J.A. Becerra-Villanueva. *Current trends in wall-flow Diesel Particulate Filters*. Journal of hazardous materials (under review)

2.1. Particulate emissions of diesel engines

2.2. Overview of the filtration process in DPFs

2.3. Aftertreatment systems for the abatement of PM

2.4. Wall-flow Diesel Particulate Filters (wall-flow DPFs)

2.5. DPF performance parameters

2.5.1. Filtration efficiency

2.5.2. Pressure drop

2.6. Regeneration process in a DPF

2.7. Motivations, research opportunities and expected contribution

From the frenzied past and present research activity, it can be clearly seen that there is a great concern in the society about particulate emissions coming from the transport sector and, in particular from diesel engines. Not only research agencies are involved, but also private companies from the automotive industry are actively participating in this joint effort to improve

the performance of current DPFs and to develop new and better particles control systems. Apart from other specific interest, three main causes are pushing the research activity in this field.

- First, the legal restrictions imposed by the environmental policies. The majority of the developed countries have legislative committees controlling the emission limits for the main pollutants. This affects directly the automotive market due to the approval system (homologation process). Vehicle manufacturing companies and other companies of the transport sector need type-approval certificates to introduce their products in the market, so they are forced to continuously update their quality standards.
- Second, the magnitude of the automotive market and the amount of money involved in this sector. Gasoline and diesel cars have become almost staple items in many countries and this is reflected in the business volume they generate. The level of sales in the global automotive industry is over 70 million vehicles a year. The manufacturers are highly encouraged to offer competitive vehicles with the best features for the drivers.
- And finally, the impulse of the increasingly social awareness regarding the environmental issue and the actual trend towards a sustainable transport. Customers do care not only about getting an economic product anymore, but they also care about their environmental impact, their ecologic dimension. The way of purchasing products has experienced a substantial change in recent years, and the cars manufacturers are sensitive to this change.

This situation is an exceptional opportunity for the development of new research projects on emission control technologies. Sustainable transport is actually one of the most important target in the Horizon 2020 Work Programme. But also a considerable part of the manufacturers budget is devoted to the development of more environmentally-friendly vehicles.

Despite their long track record in the market, particulate filters still pose several shortcomings. DPFs are physical obstacles for the passage of soot particles. The mere placement of a filter in the exhaust pipe of an engine introduces an additional pressure drop to the gases circuit that the engine must overcome with a penalty in its performance and in the fuel consumption. Current DPFs are usually made with homogeneous substrates (granular, foamed or fibre-based), which leads to a direct relationship between particles abatement capacity and pressure drop. The more a filter hinders the passage of particles, the more it hinders the passage of gases too. From the author's point of view, the particular hierarchical microstructure of biomorphic silicon carbide is an opportunity to overcome this relationship between efficiency and pressure drop. The possibility of using so many different precursors to tailor the most influential microstructural features (such as porosity or pore size distribution), provides bioSiC with a great potential to optimize separately both performance parameters.

Furthermore, the accumulation of particles in the porous substrate of the filter increases in turn the backpressure in the system. DPFs must be periodically regenerated to eliminate this accumulation of soot. But the regeneration process is both a challenge for the designer of the aftertreatment system, and a nuisance for the user. Nowadays, still more resistant materials are needed to deal with the frequent regeneration cycles that take place on board the vehicle. Silicon

carbide is the most popular material for the manufacture of DPFs for light-duty engines (passenger vehicles). It has a high heat capacity and a high thermal conductivity, apart from a high mechanical strength and chemical stability. These are suitable properties for an appropriate regeneration behaviour. Nevertheless, silicon carbide has one important drawback: its high thermal expansion coefficient forces to make the filter in several segments stuck by a cement layer.

Apart from these technical issues, silicon carbide poses another drawback: the high price of the raw materials and, sometimes, of the post-processing.

By using bioSiC as a substrate, a reduction in the cost of the raw material is foreseeable, since a considerable part of the starting material is ordinary wood. A deeper analysis may show if the silicon consumption and the differences in the manufacturing process yield similar or lower costs. This thesis analyses the potential of bioSiC as automotive DPF substrate. On this purpose the major contributions to knowledge expected from this research are listed below:

- A physical and microstructural characterization study focused on the most influential features on the filtration performance. A first selection of precursors based on a preliminary analysis of current DPF substrates. The consideration of the material anisotropy, and the differentiated study on the two possible cutting directions of the wood, which eventually turned out to be a crucial factor in the filtration performance of the material.
- An analysis on possible relationships between functional parameters of the material, useful for future predictions on the performance of other bioSiC made from different wood precursors. At this point, the dependency of the permeability and the thermal conductivity on the microstructure are worth noting. A relationship between permeability and initial filtration efficiency is also provided, that provides with an initial criterion for selecting suitable candidates for particle filtration applications.
- An optimization of the general manufacturing process of bioSiC based in the improvement of the last stage. In this work, the elimination of the excess silicon was done by means of a thermal treatment that eliminates the risks associated with the chemical etching and assures the complete reaction of the carbon matrix regardless its thickness.
- A new proposal for the manufacture of wall-flow bioSiC DPFs. A complete and customized procedure for the manufacturing of these systems is proposed including the mechanization of the channels, the sticking of the sections, and the plugging of the channels.
- Experimental measurements of the filtration performance of a bioSiC wall-flow DPF in both the initial state and during the soot load. Accurate measurement of the filtration efficiency and the pressure drop with specialized equipment. A first approximation to the regeneration process.
- The utilization of a validated numerical model to simulate the behaviour of a bioSiC wall-flow DPF that includes the main microstructural features of the biomorphic substrate. The prediction of the behaviour of a real-scale bioSiC DPF under real operating conditions in both the initial state and during the soot load. A comparative study of the filtration

performance of the bioSiC wall-flow DPF and that of a number of other commercial filters in the market.

References

[1] Guan B, Zhan R, Lin H, Huang Z. Review of the state-of-the-art of exhaust particulate filter technology in internal combustion engines. J Environ Manage 2015;154:225–58.

[2] Khair M. A Review of Diesel Particulate Filter Technologies. SAE Tech Pap Ser 2003;1:1–11.

[3] Konstandopoulos AG, Papaioannou E. Update on the science and technology of diesel particulate filters. KONA Powder Part J 2008;26:36–65.

[4] Prasad R, Bella VR. A Review on Diesel Soot Emission, its Effect and Control. Bull Chem React Eng Catal 2010;5:69–86. doi:10.9767/bcrec.5.2.794.69-86.

[5] Somiya S, Kaneno M. Handbook of advanced ceramics. 2013.

[6] Mollenhauer K, Tschöke H. Handbook of Diesel Engines. 2010. doi:10.1007/978-3-540-89083-6.

[7] Kerminen VM, Mäkelä TE, Ojanen CH, Hillamo RE, Vilhunen JK, Rantanen L, et al. Characterization of the particulate phase in the exhaust from a diesel car. Environ Sci Technol 1997;31:1883–9. doi:10.1021/es960520n.

[8] Matti Maricq M. Chemical characterization of particulate emissions from diesel engines: A review. J Aerosol Sci 2007;38:1079–118. doi:10.1016/j.jaerosci.2007.08.001.

[9] Kittelson DB. Engines and nanoparticles: A review. J Aerosol Sci 1998;29:575–88. doi:10.1016/S0021-8502(97)10037-4.

[10] Kim H, Sung Y, Jung K, Choi B, Lim MT. Size distributions and number concentrations of particles from the DOC and CDPF. J Mech Sci Technol 2008;22:1793–9. doi:10.1007/s12206-008-0610-7.

[11] Lee H, Kim J, Myung CL, Park S. Experimental investigation of nanoparticle formation characteristics from advanced gasoline and diesel fueled light duty vehicles under different certification driving modes. J Mech Sci Technol 2009;23:1591–601. doi:10.1007/s12206-009-0425-1.

[12] Park S, Kim H, Choi B. Emission characteristics of exhaust gases and nanoparticles from a diesel engine with biodiesel-diesel blended fuel (BD20). J Mech Sci Technol 2009;23:2555–64. doi:10.1007/s12206-009-0704-x.

[13] Fino D, Russo N. Characterization of particulate matter emissions from a common-rail diesel engine. Ind Eng Chem Res 2011;50:3004–10. doi:10.1021/ie102094x.

[14] Benajes J, García-Oliver JM, Novella R, Kolodziej C. Increased particle emissions from early fuel injection timing Diesel low temperature combustion. Fuel 2012;94:184–90. doi:10.1016/j.fuel.2011.09.014.

[15] Liu Z, Swanson J, Kittelson DB, Pui DYH. Comparison of methods for online measurement of diesel particulate matter. Environ Sci Technol 2012;46:6127–33. doi:10.1021/es3003537.

[16] Pant P, Harrison RM. Estimation of the contribution of road traffic emissions to particulate

matter concentrations from field measurements: A review. Atmos Environ 2013;77:78–97. doi:10.1016/j.atmosenv.2013.04.028 Review.

[17] Pope CA, Burnett RT, Thun MJ, Calle EE, Krewski D, Ito K, et al. Lung cancer, cardiopulmonary mortality, and long-term exposure to fine particulate air pollution. J Am Med Assoc 2002;287:1132–41. doi:10.1001/jama.287.9.1132.

[18] Brijesh P, Sreedhara S. Exhaust emissions and its control methods in compression ignition engines: A review. Int J Automot Technol 2013;14:195–206.

[19] Fiebig M, Wiartalla A, Holderbaum B, Kiesow S. Particulate emissions from diesel engines: correlation between engine technology and emissions. J Occup Med Toxicol 2014;9:6. doi:10.1186/1745-6673-9-6.

[20] Reşitoılu IA, Altinişik K, Keskin A. The pollutant emissions from diesel-engine vehicles and exhaust aftertreatment systems. Clean Technol Environ Policy 2015;17:15–27. doi:10.1007/s10098-014-0793-9.

[21] Johnson T. Diesel Emission Control in Review. SAE Tech Pap Ser 2001;1:1–19.

[22] Johnson T. Diesel Emission Control Technology 2003 in Review. SAE Tech Pap Ser 2004;1:1–16.

[23] Johnson T. Diesel engine emissions and their control: An overview. Platin Met Rev 2008;52:23–37. doi:10.1595/147106708X248750.

[24] Johnson T. Review of Diesel Emissions and Control. SAE Int J Fuels Lubr 2010;3:16–29.

[25] Johnson T. Diesel Emissions in Review. SAE Int J Engines 2011;4:143–57.

[26] Johnson T. Vehicular Emissions in Review. SAE Int J Engines 2012;5:216–34.

[27] Johnson T. Review of Vehicular Emissions Trends. SAE Int J Engines 2015;8:1152–67.

[28] Guerrassi N, Dupraz P. A Common Rail Injection System For High Speed Direct Injection Diesel Engines. SAE Tech Pap 1998;980803:1–10.

[29] Stumpp G, Ricco M. Common Rail - An Attractive Fuel Injection System for Passenger Car DI Diesel Engines. SAE Tech Pap 1996;960870:1–11.

[30] Park C, Kook S, Bae C. Effects of Multiple Injections in a HSDI Diesel Engine Equipped with Common Rail Injection System. SAE Tech Pap 2004;2004-01–01:1–19.

[31] Mohr M, Lehmann U, Margaria G. ACEA Programme on the Emissions of Fine Particulates from Passenger Cars(2) Part1: Particle Characterisation of a Wide Range of Engine Technologies. SAE Tech Pap 2003;01–1889:1–13.

[32] Mohr M, Lehmann U, Margaria G. ACEA Programme on the Emissions of Fine Particulates from Passenger Cars(2) Part 2: Effect of Sampling Conditions and Fuel Sulphur Content on the Particle Emission. SAE Tech Pap 2003;01–1890:1–13.

[33] Burtscher H. Physical characterization of particulate emissions from diesel engines: a review. Aerosol Sci 2005;36:896–932. doi:10.1016/j.jaerosci.2004.12.001.

[34] Tien C, Ramarao BV. Mechanisms of particle deposition. Granul. Filtr. Aerosols Hydrosols 2nd Ed., 2007, p. 117–68.

[35] Konstandopoulos AG, Johnson JH. Wall-flow diesel particulate filters - Their pressure drop and collection efficiency. SAE Tech Pap 1989;890405:1–23.

[36] Bensaid S, Marchisio DL, Russo N, Fino D. Experimental investigation of soot deposition in diesel particulate filters. Catal Today 2009;147:295–300. doi:10.1016/j.cattod. 2009.07.039.

[37] Tandon P, Heibel A, Whitmore J, Kekre N, Chithapragada K. Measurement and prediction of filtration efficiency evolution of soot loaded diesel particulate filters. Chem Eng Sci 2010;65:4751–60. doi:10.1016/j.ces.2010.05.020.

[38] Choi S, Oh KC, Lee CB. The effects of filter porosity and flow conditions on soot deposition/oxidation and pressure drop in particulate filters. Energy 2014;77:327–37. doi:10.1016/j.energy.2014.08.049.

[39] Yang J, Stewart M, Maupin G, Herling D, Zelenyuk A. Single wall diesel particulate filter (DPF) filtration efficiency studies using laboratory generated particles. Chem Eng Sci 2009;64:1625–34. doi:10.1016/j.ces.2008.12.011.

[40] Konstandopoulos AG, Skaperdas E, Masoudi M. Microstructural Properties of Soot Deposits in Diesel Particulate Traps. SAE Tech Pap Ser 2002;1:1–11.

[41] Koltsakis GC, Konstantinou A, Haralampous OA, Samaras Z. Measurement and Intra-Layer Modeling of Soot Density and Permeability in Wall-flow Filters. SAE Tech Pap 2006;2006-01–02:1–15.

[42] Liati A, Dimopoulos Eggenschwiler P, Müller Gubler E, Schreiber D, Aguirre M. Investigation of diesel ash particulate matter: A scanning electron microscope and transmission electron microscope study. Atmos Environ 2012;49:391–402. doi:10.1016/j.atmosenv.2011.10.035.

[43] Howitt JS, Montierth MR. Cellular Ceramic Diesel Particulate Filter. SAE Tech Pap Ser 1981;810114:1–12. doi:10.4271/810114.

[44] Adler J. Ceramic Diesel Particulate Filters. Int J Appl Ceram Technol 2005;2:429–39. doi:10.1016/B978-0-12-385469-8.00032-0.

[45] Aravelli K, Heibel A. Improved Lifetime Pressure Drop Management for Robust Cordierite (RC) Filters with Asymmetric Cell Technology (ACT). SAE Tech Pap Ser 2007;2007-01–09:1–14. doi:10.4271/2007-01-0920.

[46] Tsuneyoshi K, Yamamoto K. Experimental study of hexagonal and square diesel particulate filters under controlled and uncontrolled catalyzed regeneration. Energy 2013;60:325–32. doi:10.1016/j.energy.2013.07.069.

[47] Konstandopoulos AG, Kostoglou M, Skaperdas E, Papaioannou E, Zarvalis D, Kladopoulou E. Fundamental Studies of Diesel Particulate Filters: Transient Loading, Regeneration and Aging. SAE 2000 World Congr 2000-01-1016 2000:1–23. doi:10.4271/2000-01-1016.

[48] Yu M, Luss D, Balakotaiah V. Regeneration modes and peak temperatures in a diesel particulate filter. Chem Eng J 2013;232:541–54. doi:10.1016/j.cej.2013.08.006.

[49] Masoudi M. Hydrodynamics of Diesel Particulate Filters. SAE Tech Pap Ser 2002;1:1–17.

[50] Gulati S, Widjaja S. New Developments in Diesel Oxidation Catalysts and Diesel Particulate Filters. SAE Tech Pap Ser 2003;26:1–10.

[51] Fino D. Diesel emission control: Catalytic filters for particulate removal. Sci Technol Adv Mater 2007;8:93–100.

[52] Konstandopoulos AG. Technology Evaluation Report for Diesel Engine After-Treatment System. 2013.

[53] Farafontov P, Williams S, Muter J. Flow-Through Filter Technology for Heavy Duty Diesel Engines. ASME 2006 Intern. Combust. Engine Div. Fall Tech. Conf., Sacramento,

California: 2006.
[54] Kamp C, Folino P, Wang Y, Sappok A, Ernstmeyer J, Saeid A, et al. Ash Accumulation and Impact on Sintered Metal Fiber Diesel Particulate Filters. SAE Int J Fuels Lubr 2015;8:487–93.
[55] Ceramic Fibers and Cartridges. DieselNet 2001. https://www.dieselnet.com/tech/dpf_fiber.php (accessed January 16, 2018).
[56] Martins S. Ceramic Fiber in Exhaust System. SAE Tech Pap 1992;921460:1–14.
[57] Mayer A, Buck A. Knitted Ceramic Fibers - A New Concept for Particulate Traps. SAE Tech Pap 1992;920146:1–14.
[58] Bloom R. The Development of Fiber Wound Diesel Particulate Filter Cartridges. SAE Tech Pap 1995;950152:1–12.
[59] Konstandopoulos AG, Zarvalis D, Papaioannou E, Vlachos N. The Diesel Exhaust Aftertreatment (DEXA) Cluster: A Systematic Approach to Diesel Particulate Emission Control in Europe. SAE Tech Pap 2004;2004-01–06:1–18.
[60] Brillant S, Zikoridse G. Metal Fibre Diesel Particulate Filter: Function and Technology. SAE Tech Pap 2005;2005-01–05:1–10.
[61] Park JK, Nguyen TH, Kim CN, Lee SY. Simulation of flow in diesel particulate filter system using metal fiber filter media. Int J Automot Technol 2014;15:361–7.
[62] Meinig U, Spies K, De Bruyne R. Tests on a New Diesel Particulate System with Traps of Metal Fleece. SAE Tech Pap 1998;982597:1–9.
[63] Mehta S, Levendis Y, Adiletta J. A Thermally Regenerated Diesel Particulate Trap Using High-Temperature Glass-Fiber Filters. SAE Tech Pap 1995;950737:1–14.
[64] Gehrke L, Kohberg C, Lücking C, Meisohle K-H, Schumacher U, Woiki D. Particle filter body for filtering internal combustion engine waste gas. WO/2009/003610, 2009.
[65] HJS Emission Technology. Sintered Metal Filter 2018. http://www.hjs.com/aftermarket/products/diesel-particulate-filters/sintered-metal-filter.html (accessed January 16, 2018).
[66] HJS Emission Technology. Product Range. Diesel Particulate filters Modular SMF(R) and SMF(R)-AR Systems. 2013:1–40. https://www.krone-filter.de/assets/files/datasheet-en/soot-filter/SMF.pdf.
[67] Scheffler M, Colombo P. Manufacturing. Honeycombs. Cell. Ceram. Struct. Manuf. Prop. Appl., 2005, p. 57–86.
[68] Mayer A. Particle Filter Retrofit for All Diesel Engines. Die Deutsche Bibliothek; 2008.
[69] Chatterjee D, Rusch K. SCR Technology for Off-highway (Large Diesel Engine) Applications. Urea-SCR Technol. deNOx After Treat. Diesel Exhausts, 2014, p. 33–61.
[70] Benaqqa C, Gomina M, Beurotte A, Boussuge M, Delattre B, Pajot K, et al. Morphology, physical, thermal and mechanical properties of the constitutive materials of diesel particulate filters. Appl Therm Eng 2014;62:599–606. doi:10.1016/j.applthermaleng.2013.10.024.
[71] Majewski WA. Diesel Particulate Filters. DieselNet 2011. https://www.dieselnet.com/tech/dpf.php.
[72] Stratakis GA, Psarianos DL, Stamatelos AM. Experimental investigation of the pressure drop in porous ceramic diesel particulate filters. Proc Inst Mech Eng Part D-Journal Automob Eng 2002;216:773–84.

[73] Heibel A, Bhargava R. Advanced Diesel Particulate Filter Design for Lifetime Pressure Drop Solution in Light Duty Applications. SAE Tech Pap Ser 2007;1:1–12. doi:10.4271/2007-01-0042.
[74] Schejbal M, Marek M, Kubíček M, Kočí P. Modelling of diesel filters for particulates removal. Chem Eng J 2009;154:219–30. doi:10.1016/j.cej.2009.04.056.
[75] Williams AM, Garner CP. Correcting mass measurement of diesel particulate filters at non-ambient temperatures. Proc Inst Mech Eng Part D J Automob Eng 2009;223:99–105.
[76] Nemoto A, Iwasaki K, Yamanishi O, Tsuchimoto K, Uoe K, Toma T, et al. Development of Innovative Diesel Particulate Filters based on Aluminum Titanate: Design and Validation. 2011.
[77] Boger T, Jamison J, Warkins J, Golomb N, Warren C. Next Generation Aluminum Titanate Filter for Light Duty Diesel Applications 2011. doi:10.4271/2011-01-0816.
[78] Tsuneyoshi K, Takagi O, Yamamoto K. Effects of Washcoat on Initial PM Filtration Efficiency and Pressure Drop in SiC DPF. SAE Tech Pap Ser 2011;1:1–10.
[79] Tsuneyoshi K, Yamamoto K. A study on the cell structure and the performances of wall-flow diesel particulate filter. Energy 2012;48:492–9. doi:10.1016/j.energy.2012.10.007.
[80] Zhong D, He S, Tandon P, Moreno M, Boger T. Measurement and Prediction of Filtration Efficiency Evolution of Soot Loaded Diesel Particulate Filters. SAE Tech Pap Ser 2012;1:1–5. doi:10.4271/2012-01-0363.
[81] Lapuerta M, Rodríguez-Fernández J, Oliva F. Effect of soot accumulation in a diesel particle filter on the combustion process and gaseous emissions. Energy 2012;47:543–52. doi:10.1016/j.energy.2012.09.054.
[82] Gulati S. Cell Design for Ceramic Monoliths for Catalytic Converter Application. SAE Tech Pap Ser 1988;881685:1–12.
[83] Liu Z, Miller R. Flow Distributions and Pressure Drops of Wall-Flow Diesel Particulate Filters. SAE Tech Pap Ser 2002;1:1–14.
[84] Bardon S, Bouteiller B, Bonnail N, Girot P, Gleize V, Oxarango L, et al. Asymmetrical Channels to Increase DPF Lifetime. SAE Tech Pap Ser 2004;1:1–14.
[85] Briot A, Carranza F, Girot P, Bardon S. Minimizing Filter Volume by Design Optimization. SAE Tech Pap Ser 2007;1:1–11.
[86] Mizuno Y, Miyairi Y, Katsube F, Ohara E, Takahashi A, Makino M, et al. Study on Wall Pore Structure for Next Generation Diesel Particulate Filter. SAE Tech Pap Ser 2008;1:1–12.
[87] Furuta Y, Mizutani T, Miyairi Y, Yuki K, Kurachi H. Study on Next Generation Diesel Particulate Filter. SAE Tech Pap Ser 2009;1:1–8.
[88] Mizutani T, Iwasaki S, Miyairi Y, Yuuki K, Makino M, Kurachi H. Performance Verification of Next Generation Diesel Particulate Filter. SAE Tech Pap Ser 2010;1:1–9.
[89] Iwasaki S, Mizutani T, Miyairi Y, Yuuki K. New Design Concept for Diesel Particulate Filter. SAE Tech Pap Ser 2011;1:1–10.
[90] Ingram-Ogunwimi RS, Dong Q, Murrin TA, Bhargava RY, Warkins JL, Heibel AK. Performance Evaluations of Aluminum Titanate Diesel Particulate Filters. SAE Tech Pap Ser 2007;1:1–14.
[91] Majewski WA. Diesel Filter Materials. DieselNet 2003. https://www.dieselnet.com/.

[92] Stobbe P, Petersen H, Høj J, Sorenson S. SiC as a Substrate for Diesel Particulate Filters. SAE Tech Pap 932495 1993.
[93] Ohji T, Singh M, Wereszczak A. Advanced Processing and Manufacturing Technologies for Structural and Multifunctional Materials II, Volume 29, Issue 9. Wiley & Sons Ltd; 2009.
[94] Patrianakos G. State of the art study report of low emission diesel engines and after-treatment technologies in rail applications. 2013.
[95] Mizutani T, Ito M, Masukawa N, Ichikawa S, Yuuki K, Kurachi H, et al. The Study for Structural Design of the Segmented SiC-DPF. SAE Tech Pap 2006;2006-01–15:1–10.
[96] Itoh A, Shimato K, Komori T, Okazoe H, Yamada T, Niimura K, et al. Study of SiC Application to Diesel Particulate Filter (Part 1): Material Development. SAE Tech Pap 1993;930360:1–11.
[97] Nakamura K, Vlachos N, Konstandopoulos AG, Iwata H, Kazushige O. Performance Improvement of Diesel Particulate Filter by Layer Coating. SAE Tech Pap 2012;2012-01–08:1–9.
[98] Rose D, Heibel AK, George S, Warkins J, Golomb N, Warren C. A new generation high porosity DuraTrap® AT for integration of DeNOx functionalities. 21st Aachen Colloq. Automob. engine Technol., Aachen: 2012.
[99] Rose D, Boger T, Nicolin P, Ingram-Ogunwumi R, Bischof C, Gunasekaran N. Advanced Filter Technologies to Reduce Particulate Emissions of GDI Engines. Aachener Kolloquium Fahrzeug und Mot., Aachen: 2013.
[100] Bachiorrini A. New Hypotheses on the Mechanism of the Deterioration of Cordierite Diesel Filters in the Presence of Metal Oxides. Ceram Int 1996;22:73–7.
[101] Locker JL, Sawyer CB, Menon S, Floerchinger P, G. CA. Diesel particulate filter operational characterization. SAE Tech Pap 2004;2004-01–09:1–11.
[102] Cutler W, Boger T, Chiffey A, Phillips P. Performance Aspects of New Catalyzed Diesel Soot Filters Based on Advanced Oxide Filter Materials. SAE Tech Pap 2007;2007-01–12:1–7.
[103] Boger T, He S, Collins T, Heibel A, Beall D, Remy C. A Next Generation Cordierite Diesel Particle Filter with Significantly Reduced Pressure Drop. SAE Tech Pap Ser 2011;4:902–12. doi:10.4271/2011-01-0813.
[104] Merkel GA, Tao T. Narrow pore size distribution cordierite filters with reduced pressure drop. US7309371 B2, 2007.
[105] Miao W, Wang J. Reactive binders for porous wall-flow filters. US7575618 B2, 2007.
[106] Yoon J, Kim M, Song S, Chun KM. Calculation of mass-weighted distribution of diesel particulate matters using primary particle density. J Aerosol Sci 2011;42:419–27. doi:10.1016/j.jaerosci.2011.03.005.
[107] Yamamoto K, Fujikake F, Matsui K. Non-catalytic after-treatment for diesel particulates using carbon-fiber filter and experimental validation. Proc Combust Inst 2013;34:2865–75. doi:10.1016/j.proci.2012.09.006.
[108] Petasch U, Adler J. Diesel particulate filters with optimized pressure drop and filtration efficiency. Fraunhofer IKTS Annual Report 2013/14. 2014.
[109] Pontikakis GN, Koltsakis G, Stamatelos AM. Dynamic Filtration Modeling in Foam

Filters for Diesel Exhaust. Chem Eng Comm 2001;0:1–26.
[110] Millo F, Andreata M, Rafigh M, Mercuri D, Pozzi C. Impact on vehicle fuel economy of the soot loading on diesel particulate filters made of different substrate materials. Energy 2015;86:19–30. doi:10.1016/j.energy.2015.03.076.
[111] Millet CN, Ménégazzi P, Martin B, Colas H. Modeling of Diesel Particulate Filter Regeneration , with the Effect of Fuel-Borne Catalyst on Pressure Losses and Soot Oxidation Kinetics. Oil Gas Sci Technlogy 2003;58:151–62.
[112] Johnson T. Diesel Emission Control in Review. SAE Int J Fuels Lubr 2009;2:1–12.
[113] Boger T, Rose D, Tilgner I-C, Heibel AK. Regeneration Strategies for an Enhanced Thermal Management of Oxide Diesel Particulate Filters. SAE Tech Pap Ser 2008;2008-01–03:1–13.

Chapter 3
Materials and methods

In this chapter, a detailed description of the methodology followed in this thesis is presented. The research was planned in two main stages.

- The first stage was devoted to studying the bioSiC filters at the material level. Small laboratory samples were manufactured from different precursors, and a comprehensive characterization study was carried out to obtain a physical and microstructural description representative for the target application.
- In the second stage, a more specific study up to the system level was carried out. After developing a customized fabrication procedure, a real MDF-bioSiC wall-flow prototype was made, and a specific experimental campaign to determine its filtration performance was developed. Then, with the aid of a validated numerical model, the experimental results were scaled up to a real-size DPF and the potential of the system to comply with the current European regulation was analysed.

Accordingly, the first half of the chapter will be dedicated to the fabrication of the laboratory samples and to the characterization study at the material level, while the second half will be dedicated to the fabrication of the prototypes and to the experimental measurements at a system level. Chapter 3 is structured in six sections. Section 3.1 provides a general description of the standard manufacturing process for bioSiC elements. In Section 3.2 the selection criteria for the initial precursors is stated, and a description of the laboratory samples and their manufacturing procedure is provided. Section 3.3 presents all the techniques used to characterize the samples, the theory in which they are based, and the equipment used for the analyses. Then, Section 3.4 presents the customized procedure developed to manufacture bioSiC wall-flow DPFs. Section 3.5 describes the test rig in which the experimental campaign with the prototypes was carried out and the test parameters. Finally, in Section 3.6 the numerical tools used to model the bioSiC wall-flow DPF are presented, and the calibration and validation procedures are described.

The manufacturing processes at both levels are an important focus of attention in this thesis. Unlike granular silicon carbide commercially used in DPFs, bioSiC cannot be manufactured from sludge by a sintering process. BioSiC is manufactured from the pyrolysis of wood blocks and it passes through different stages, but always in solid state. Furthermore, wall-flow DPFs are

systems with complex geometry, not easy to shape. Consequently, the manufacturing strategy is as important as the choice of the precursor, and so sections 3.2 and 3.4 are specifically focused on this issue.

A significant part of the work reported in this thesis is experimental. The characterization study was mainly performed in the Central Services of the University of Seville (CITIUS), except the efficiency tests which were carried out in the Laboratory of Thermal Engines. The experimental campaign with the MDF-bioSiC wall-flow DPF prototypes was carried out in the Laboratory of Environmental Catalysis of the Polytechnic of Torino.

Related publications

1. A. Gómez-Martín, M.P. Orihuela, J.A. Becerra-Villanueva, J. Martínez-Fernández, J. Ramírez-Rico. *Permeability and mechanical integrity of porous biomorphic SiC ceramics for application as hot-gas filters*. Materials & Design, Vol. 107, 450–460, 2016. doi: 10.1016/j.matdes.2016.06.060
2. A. Gómez-Martín, M.P. Orihuela, J. Ramírez-Rico, R. Chacartegui, J. Martínez-Fernández. *Thermal conductivity of porous biomorphic SiC derived from wood precursors*. Ceramics International, Vol. 42, Iss. 14, 16220–16229, 2016. doi: 10.1016/j.ceramint.2016.07.151
3. M.P. Orihuela, A. Gómez-Martín, J.A. Becerra-Villanueva, R. Chacartegui, J. Ramírez-Rico. *Performance of biomorphic Silicon carbide as particulate filter in diesel boilers*. Journal of Environmental Management, Vol. 203, Iss. 3, 907-919, 2017. doi: 10.1016/j.jenvman.2017.05.003
4. M.P. Orihuela, A. Gómez-Martín, P. Miceli, J.A. Becerra-Villanueva, R. Chacartegui, D. Fino. *Experimental measurement of the filtration efficiency and pressure drop of wall-flow Diesel Particulate Filters (DPF) made of biomorphic Silicon Carbide using laboratory generated particles*. Applied Thermal Engineering, Vol. 131, 41-53, 2018. doi: 10.1016/j.applthermaleng.2017.11.149
5. M.P. Orihuela, O. Haralampous, R. Chacartegui, J. Martínez. *Numerical simulation of a wall-flow Diesel Particulate Filter made of biomorphic Silicon Carbide*. SAE international (under review)

3.1. Standard manufacturing process of bioSiC elements

The standard fabrication process of bioSiC has been extensively described in the literature [1–3]. It consists of three main steps as presented in Figure 3.1. The raw material is a vegetal precursor (e.g. wood). The only requirement to manufacture a bioSiC piece and to assure a complete reaction between the carbon preform and the melted silicon, is to have an open porosity with a minimum pore size of about 5 μm [4]. Prior to pyrolyzation, the precursor material is pre-shaped with preliminary dimensions close to the final design and it is dried in a stove. Then it is pyrolyzed in an inert atmosphere at around 1000 ºC. During this process, the organic matter is decomposed,

and water and other volatile compounds evaporate. As a result, a carbon block is obtained with a volume reduction of around 60 ± 5% [2]. This carbon preform keeps the basic microstructure of the departing natural material.

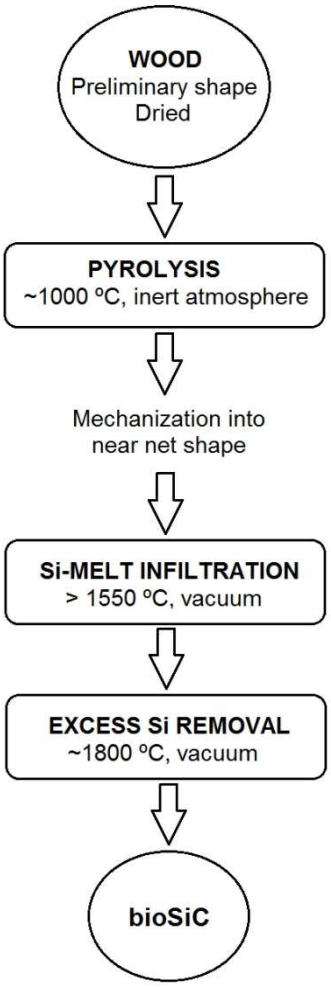

Figure 3.1. Scheme of the bioSiC manufacuting process

Since carbon is softer than silicon carbide, the carbon blocks are now mechanized into near net shape pieces. Next, the carbon matrixes are infiltrated with silicon in order to provoke the SiC forming reaction (C + Si → SiC). To this end, the typical standard procedure is infiltrating the carbon pieces with molten silicon in vacuum over the melting temperature 1550 ºC during at least 30 mn. According to chemical proportions, to perform a stoichiometric reaction, 2.33 grams of silicon are needed for each gram of carbon. Nevertheless, previous studies have demonstrated that the stoichiometric process leaves non-reacted carbon parts due to the preform porosity. Thus, an excess of Si is generally needed to complete the SiC formation. Bautista et al. stated that, using a 50% of silicon in excess, there were no unreacted carbon parts, and no big silicon lumps appeared in the outside [5]. This leads to a Si/C weight ratio of around 3.5.

After the infiltration process, the small pores become filled with residual Si, so the resulting material is a Si/SiC composite. No bulk volume increase is observed after the infiltration step.

To obtain porous biomorphic SiC the unconsumed Si has to be removed. In the methodologies used before this research project, the most commonly used methods to remove the residual Si were based on chemical etching with a solution of hydrofluoric (HF) and nitric acids (HNO_3) [6,7]. Nevertheless, the risks associated with the manipulation of high concentration acids, long etching times and waste disposal, make chemical etching impractical for producing large batches of material. Moreover, the reaction volume of the acid solution is limited by its penetration capacity through the pores. If the carbon matrix is too thick, the acid solution does not penetrate into the core and part of the carbon remains unreacted. As an alternative to this manufacturing process, in this work a different route was proposed which involves removing the excess silicon by capillary extraction and evaporation at high temperature.

In this process bioSiC specimens placed on top of porous carbon slabs are heat-treated up to 1800 °C in vacuum during 4 h. Remnant Silicon evaporates due to the high temperature and gets out of the pores via capillary forces towards the carbons slabs. The final material obtained after the heat-treatment consists of a highly porous silicon carbide scaffold that reproduces the cellular morphology of natural precursor.

3.2. Laboratory scale disk-shaped samples

For characterization purposes, simple geometry samples were proposed. The characterization techniques used in this work require small amounts of material; and to make permeability and filtration tests, samples should rather have a small thickness. Thus, disk-shaped samples with 1 inch in diameter and 3 mm thick were finally used.

Precursors selection

With the manufacturing process presented in Section 3.1 it is possible to tailor the porous microstructure of the final bioSiC. By using an appropriate precursor, its final properties can be adjusted. There are two main differences between the initial biological microstructure of the wood precursor and the final microstructure of the biomorphic ceramic material:

- The tissue constriction produced during the pyrolysis process. Approximately 74% of the starting weight of the wood is lost during the pyrolysis due to the decomposition of the organic matter and the evaporation of water [4]. This leads to a length shrinkage of around 30%, and thus, to a volume reduction of around 60% [2].
- The disappearance of the smallest pores due to the infiltration process with silicon and the impossibility of overcoming the surface tension later in the evaporation process.

Wood has a honeycomb-type microstructure consisting of long pores arranged parallel to the axis of the tree (axial direction). In Section 4.1, SEM micrographs of the microstructure of the carbon matrixes after the pyrolysis process are presented. Although in this stage the organic compounds

have already been decomposed and only carbon remains, the micrographs show that the specimens preserve the microstructure of the biological tissue with its cells and vessels.

Wood can be classified as either softwood or hardwood. Softwoods have one type of pore in the plane perpendicular to the growth direction, while hardwoods tend to have two types of pores in this plane in different size ranges and with different wall thicknesses [8]. On the other hand, wood may also present growth rings and rays. Plants exposed to changing climates and clearly differentiated seasons develop growth rings, in which sequentially growing cells can be observed. Hence, this also affects to the microstructure [8].

In this work, the selection of wood precursors for the characterization study was made trying to encompass a wide range of porosities, pore sizes and densities. Four natural wood precursors and one processed wood were selected: Ayous (*Triplochiton scleroxylon*), Pine (*Pinus sylvestris*), Iroko (*Chlorophora excelsa*), and Oak (*Quercus rubra*); and Medium Density Fibreboard (MDF). Densities range from 0.3 to 0.8 g/cm^3. Ayous and Pine are low density woods, while Iroko and Oak are high density woods. Ayous and Iroko are tropical woods so they don't have growth rings, while Pine and Oak do.

Cutting direction

Natural wood is an anisotropic material; it has two well differentiated microstructural planes. In the axial plane (perpendicular to the axis of the tree), wood presents small round or square pores due to the cross-cutting of the cells. In the radial plane (or any other vertical plane parallel to the axis of the tree), wood presents a distribution of long pores due to the lengthwise-cutting of the cells. From the point of view of filtration processes, this is a critical factor [9]. In any type of filter, there are four main filtration mechanisms: sieving, inertial impaction, interception, and Brownian diffusion. The arrangement of the pores affects directly the result of these mechanisms.

In this work, natural woods were tested in both cross-cutting and lengthwise-cutting. Half of the samples were made cutting the carbon blocks in the axial direction, and the other half of the samples were made cutting the carbon blocks in transverse direction. The resulting samples show a completely different surface aspect despite coming from the same precursor; it can be seen in Figure 3.7 in the following epigraph.

Fabrication process

As previously commented, the samples for the characterization study at laboratory scale were designed with disk-shaped geometry of 1 inch in diameter and 3 mm thick. Their manufacturing process was as follows.

First, the wood was cut into cubic blocks and dried in a stove for 24 hours at 70 ºC to remove the moisture. The wood blocks were pyrolyzed in an inert atmosphere using two successive heating ramps: first, a slow heating ramp of 0.5 °C min^{-1} up to 500 °C to avoid crack formation; and then

a higher heating ramp of 1 °C min^{-1} up to a peak temperature of 900 °C, followed by a soak time of 30 min to complete the pyrolysis process. The time-based pyrolyzation heating programme is represented in Figure 3.2.

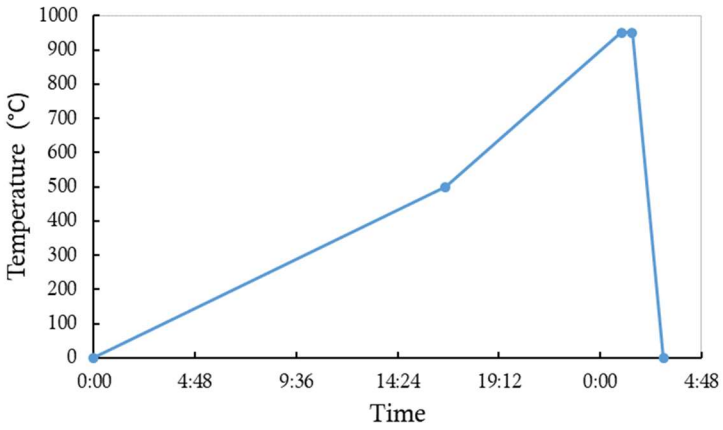

Figure 3.2. Pyrolyzation heating programme

As a result of the process, a number of porous carbon templates were obtained. Figure 3.3 on the left shows the furnace were the controlled pyrolysis process was carried out, and on the right hand side shows the pyrolyzed blocks after the process.

Figure 3.3. Pyrolysis furnace on the left hand side. On the right hand side, inside view of the furnace with the carbon blocks obtained after the pyrolysis

These carbon blocks were then mechanized into disks with the design dimensions. A hollow drill was first used to make cylinders of 1 inch in diameter. Except for the MDF carbon blocks, the drilling direction was set for each block taking into account the arrangement of the cells. Axial samples were drilled in the direction of the cells, that is, parallel to the axis of the tree. Radial samples were drilled perpendicular to the direction of the cells, that is, perpendicular to the axis of the tree. Then, the cylinders were sliced into 3 mm thick disks with the aid of a precision slicer machine (Figure 3.4). MDF samples were all cut in the same direction (the cylinders in the compression direction, and the slices perpendicularly), due to the limited thickness of the MDF panels. Later, in the final analysis at the global system level, a critical revision is done on this

choice since the characteristic geometry of wall-flow DPFs forces the gas flux to flow in the direction perpendicular to the axis of the monolith.

Figure 3.4. Cutting of the carbon cylinders into disks in the precision slicing machine

As a result of the mechanization process, near-net-shape carbon preforms were obtained. These carbon preforms were then placed in a crucible and infiltrated with molten silicon (Silgrain HQ-99.7% purity; Eljem Silicon, Oslo, Norway) using a Si:C weight ratio of 3.5, as previously said. The infiltration process was carried out in a high-temperature furnace (Nabertherm VHT 8/16-MO) at 1550 °C for 30 min in vacuum. Figure 3.5 shows, on the left hand side, the carbon disks covered with Silicon powder before the infiltration process; and, on the right hand side, the same disks converted to SiC after the infiltration process. The furnace is shown in Figure 3.6.

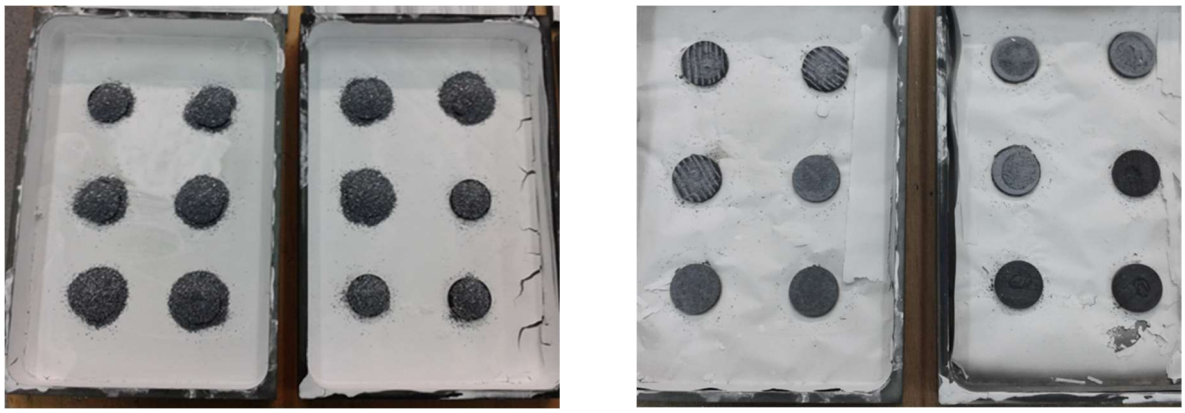

Figure 3.5. Specimens inside the crucible before (left) and after (right) the infiltration process

After the infiltration process, the pores become filled with residual Si, so the resulting material is a Si/SiC composite. Besides, although the process does not modify the size of the samples, it is frequent to find silicon lumps on their outside surface. All this silicon in excess must be removed to obtain the porous material. In this work, the unconsumed Si was removed by capillary extraction and evaporation at high temperature. The specimens, placed on top of porous carbon slabs, were heat treated up to 1800 °C in vacuum at a heating rate of 8 °C min^{-1} followed by a soaking time of 4 h. This process is carried out in the same furnace as the infiltration (Figure 3.6).

Figure 3.6. High-temperature furnace used for the infiltration and the evaporation processes

During the manufacturing period, more than 100 samples were made. At least 12 samples of each type of natural precursor and each cutting direction, and at least 20 from MDF. Hereafter, samples will be identified with the following nomenclature: the first letter indicating the cutting direction; and the second letter indicating the wood precursor (Table 3.1). For instance, RI will stand for Radial Iroko, and AA will stand for Axial Ayous.

Table 3.1. Samples identification nomenclature

First letter		Second letter	
		A:	Ayous
A:	Axial	P:	Pine
R:	Radial	I:	Iroko
		O:	Oak

Figure 3.7 shows the final aspect of the Oak samples: the axial (left) and the radial (right) one. As can be seen, differences between them can be clearly appreciated: the axial sample has well-differentiated frontal pores, while the radial one does not have visible crossing pores but bunches of lengthwise grooves.

Figure 3.7. Final aspect of the Oak samples: AO (left) and RO (right)

3.3. Characterization techniques

The suitability of a material to be used as substrate in DPFs is determined mainly by its filtration efficiency and by the pressure drop it introduces in the flow. At a microstructural level, these properties, filtration efficiency and pressure drop, depend on several parameters: porosity, pore size distribution, specific surface, tortuosity. These microstructural parameters determine the level of hindrance that the material presents against the passage of particles (filtration efficiency). At the same time, they also determine the gas flow resistance or permeability (pressure drop). Thus, a successful combination of these microstructural parameters must be found to keep a good filtration efficiency while reducing/controlling the pressure drop induced in the flow. Apart from the filtration efficiency and the pressure drop, there are also some other physical properties which are desirable to assure the durability of the filter during its lifespan, specially due to the hard conditions that take place during the regeneration process. These are: high thermal conductivity, low thermal expansion coefficient (CTE), and high mechanical resistance. Some of them are especially relevant in automotive applications with variable thermal and mechanical loads (i.e. in engine cold starts, and vibrations derived from road).

This research work features biomorphic silicon carbide as a possible alternative to traditional ceramic granular media. However, the wide variety of vegetal species that can be used for its manufacture, make it difficult to test them all experimentally. In order to identify the most appropriate precursors for developing DPFs, nine options were proposed (4 natural precursors in 2 cutting directions, and one processed precursor), and a comprehensive characterization study was carried out. Functional characterization studies can be done over small simple samples, don't require much time, and provide with abundant information about the material, its microstructure and its physical and chemical properties. Manufacturing wall-flow DPFs with all the precursors would have been time-consuming and it would have only provided information about their filtration performance. Through a previous characterization study, not only all the precursors can be characterized simultaneously in a relatively short time, but also direct relationships between the filtration parameters and the microstructure and properties of the specimens can be drawn as will be shown in Chapter 5.

The study comprises a considerable number of techniques that are described below. In addition to the physical and microstructural parameters previously mentioned, the permeability of the samples was determined with a laboratory-made permeameter in order to get a direct measurement of the pressure drop with an air stream at ambient temperature. Besides, a phase analysis and a thermogravimetry analysis were performed to determine the crystalline composition of the resulting materials, and to identify if residual carbon remains in the material after the manufacturing process.

The different characterization techniques used in this work are explained below. Tests were performed at the General Research Services of the University of Seville (*Centro de Investigación, Tecnología e Innovación*, CITIUS), at the laboratory of Multifunctional Biomimetic Materials, and the laboratory of Thermal Engines of the University of Seville.

3.3.1. Microstructural characterization

In order to observe the microstructure of the samples, to stablish visual differences between precursors, and to identify the features of the filtration surface depending on the cutting direction, a scanning electron microscope (SEM, Jeol 6460-LV) equipped with secondary electron (SE) and backscattered electron (BSE) detectors was used.

Density based porosity

BioSiC is a highly porous material and so it is necessary to differentiate between bulk (apparent) density and real density. The bulk density does not take into account the pores of the material; it is easily calculated by weighting the samples and dividing their weight by their volume, but it does not provide information about the porosity. To estimate the porosity, the real density of the material must be also measured. From both densities, the porosity of the sample may be calculated by comparing them as presented in Eq. 3.1.

$$\varepsilon = 1 - \frac{\rho_{bulk}}{\rho_{real}} \qquad \text{Eq. 3.1}$$

The real density of a porous material can be measured by pycnometry techniques, in which the real volume occupied by the solid is calculated based on the displacement of a gas. For this work, a helium pycnometer Pentapycnometer 5200 (Quantachrome Instruments) has been used. If there are not closed pores in the material, this real density should be similar to the theoretical density of solid (non-porous) silicon carbide, considering that biomorphic silicon carbide is just a sort of porous silicon carbide. Thus, an alternative way to estimate the porosity of a bioSiC sample is to compare its real density with the density of pure non-porous SiC. The theoretical density of monolithic fully dense SiC has been reported to be 3.21 g/cm^3 [10].

Porosity and pore size distribution

To get a more detailed information about the porosity but especially about the pore size distribution, the samples were characterized by mercury intrusion porosimetry. This technique is based upon the physical principle that a non-reactive, non-wetting liquid such as mercury will not penetrate the fine pores of a solid absorbent until sufficient pressure is applied to force its entry. The relationship between the applied pressure and the pore diameter into which mercury will intrude is given by the Washburn equation [11].

$$r_p = \frac{-2\sigma \cos\theta}{P} \qquad \text{Eq. 3.2}$$

where P is the applied pressure, r_p is the pore radius, σ is the surface tension of the mercury (480 dyne/cm) and θ is the contact angle between mercury and the pore wall, usually taken as 140º.

By applying this technique to a sample, several characteristic textural parameters such as the pore size, the pore volume distribution, and the total porosity of the sample, can be obtained. The porous ceramic samples made in this research work were characterized with a Mercury porosimeter Pore Master 60 GT (Quantachrome Instruments). To measure pore sizes above 7 μm, the low pressure system was used (0.2-50 psi), where mercury is pushed into the pores of the material through air injection. To measure smaller pores, a higher pressure is needed (20-60000 psi), so the high pressure hydraulic system was activated.

Specific surface

The technique of physisorption is based on the adsorption phenomenon, and it describes the interaction between the surface of a solid and the molecules of a gas or a fluid when they get in contact. The adsorbate (gas or liquid) gets in contact with the adsorbent (solid) and become weakly bonded by Van der Waals forces. In the process of adsorption, a known amount of a gas such as N_2, CO_2, or Kr is injected in a cell containing the material under study, and the amount of gas adsorbed by the sample is determined as a function of the equilibrium pressure of the solid-gas system at constant temperature.

The adsorption isotherm curve is the most direct way to log the adsorption experimental data, and it consists of a representation of the pressure of the adsorbable gas versus the amount of adsorbate gas sticked to the solid. The pressure is usually expressed as relative pressure (the ratio between the absolute pressure P and the gas saturation pressure P_0).

By using Kr at 77 K as adsorbate gas, and by applying the BET (Brunauer, Emmett and Teller) theory [12], the specific surface of the bioSiC samples was determined from the adsorption isotherm curves and from the amount of adsorbed gas. Kr was used as adsorbate instead of N_2 due to the low specific surface of the samples.

The equipment used in this work to make the measurements was an analyser Micromeritics ASAP 2420, which has twelve ports and allows to degasify the samples by heating the glass containers with thermal jackets up to 450 ºC. The degasification was made at 450 ºC during 4 hours to eliminate the absorbed water and other environmental pollutants. This way, a satisfactory cleaning of the surface of the samples was accomplished, and therefore optimal and reproducible results in the adsorption isotherm curves were obtained.

3.3.2. Thermal and mechanical characterization

Diesel filters are exposed to variable thermal and mechanical loads. During a normal drive, variations in the engine temperature affect the thermal loads in the exhaust system, while the contact with the ground transmits mechanical vibrations to the whole vehicle. If a DPF is installed in the exhaust pipe, the regeneration cycles will produce an even higher thermal stress. Consequently, substrates should have high thermal stability and low thermal expansion coefficient. Current SiC DPFs are fabricated in segments and joined together through bonding

layers so that the thermal expansion of the whole DPF is absorbed by these layers. Nevertheless, the manufacturing cost of these segment-type DPFs is high and the material loss is significant as compared to monolith-type DPFs [13]. This problem is intensified when the material is exposed to an additional mechanical stress as happens with the vibrations in a vehicle.

In this work, the thermal expansion coefficient of bioSiC has been determined and compared to that of traditional SiC or cordierite in order to compare their performance under variable thermal loads. This study is required to evaluate the necessity of segmentation in a full-scale filter under variable thermal load operating conditions as those that appear in automotive applications.

The use of bioSiC at high operating temperatures takes advantage of properties such as high thermal conductivity and thermal diffusivity and, due to its controllable microstructure, bioSiC could be a promising candidate in high temperature applications. Heat dissipation is an important property in those scenarios, and a high thermal conductivity provides a more homogeneous temperature distribution in the material, leading to a better thermal shock resistance.

Investigation of thermal conductivity has attracted attention for wood-derived carbon preforms and for biomorphic SiC ceramics with excess of silicon [14–16]; but thus far, these studies have been basically performed at temperatures not much greater than room temperature. Due to the potential applications of these materials at higher temperatures and their low processing cost, some recent studies have analysed the thermal conductivity of carbon and ceramic composites and of porous wood-derived ceramics at temperatures near 1000 °C [17–19]. Some authors have assessed the thermal properties of biotemplated SiC materials removing the excess of silicon by chemical etching. For instance, Pappacena et al. [17] investigated the dependence between thermal conductivity and microstructure of porous bioSiC at temperatures ranged from room temperature to 1100 °C. Nevertheless, as previously mentioned, they used chemical etching to remove the residual silicon after the infiltration while, in this work, the excess silicon has been removed through thermal means. In this work, the thermal conductivity of porous bioSiC from different precursors have been determined for both the axial and the radial directions, at temperatures ranging from room temperature to 700 °C.

To cope with the large pressure gradients that take place during the filtration process, DPFs must also have good mechanical properties. Much attention has also been paid to this issue. Some previous studies have already explored the mechanical properties of bioSiC-Si composites [20–22], and bioSiC porous ceramics [4,23] at high temperatures. At this point, the microstructure, the porosity and the residual carbon play an important role in the resulting mechanical strength [8], so in this work a specific study on the mechanical behaviour of bioSiC made with the chosen precursors has been carried out.

Thermal expansion coefficient

The thermal expansion coefficient (CTE) defines the relative change in length that one material experiments when it is subjected to a change in temperature. In this work, to measure the CTE of

the bioSiC samples, a TMA PT1000 dilatometer (Linseis) was used. Small parallelepiped blocks of (3 × 3 × 5) mm^3 were cut from each sample and placed inside a quartz sample-carrier. A contact force was applied between the upper surface of the sample and a quartz cylindrical piston to be able to evaluate the change in length. The tests were carried out in inert atmosphere (Ar) to avoid the oxidation of the samples with a heating ramp of 10 ºC min^{-1} up to 1000 ºC. Besides, to take into consideration the thermal expansion of the pistons during the heating process, a blank test with a quartz pattern in the same conditions was performed.

Thermal conductivity

The thermal conductivity (k) can be determined from the sample thermal diffusivity (α), the specific heat (C_p) and the density (ρ) by using the following equation:

$$k(T) = C_p(T)\ \alpha(T)\ \rho \qquad \text{Eq. 3.3}$$

The thermal diffusivity of the bioSiC specimens was measured by the Laser Flash method [24]. In this method one side of a plane-parallel sample was heated by a laser pulse. The energy of the pulse was absorbed on the front surface of the specimen and the resulting rear face temperature rise was recorded by an InSb infrared (IR) detector. The thermal diffusivity value was calculated from the specimen thickness and the time required for the rear face temperature rise to reach a certain percentage of its maximum value [25] as follows:

$$\alpha(T) = \frac{\omega\ L^2}{\pi^2\ t_{1/2}} \qquad \text{Eq. 3.4}$$

where α is the thermal diffusivity in cm^2/s, L is the sample thickness, ω is a constant determined by the Clark and Taylor approximation [26] and $t_{1/2}$ is the half time, which is the time it takes for the temperature on the back of the sample to reach half of its maximum value.

Thermal diffusivity in both axial and radial orientations was measured by the Laser Flash method in vacuum to avoid oxidation of the samples (Linseis LFA1600). Measurements were performed from room temperature to 700 °C in intervals of 100 °C [25]. The reported diffusivity corresponds to the mean of three measurements at each temperature for each precursor. One sample from each wood precursor type and orientation was tested. The laser pulse was applied both parallel (axial samples) and perpendicular (radial samples) to the direction of the channels in order to consider the anisotropy in the microstructure. Before testing, samples were spray coated with a thin layer of colloidal graphite (10 mm nominal thickness) for an increase in the absorption efficiency of the laser pulse and to prevent the direct laser radiation from reaching the infrared detector [25].

Once the thermal diffusivity was measured, the thermal conductivity was calculated from the experimental values of thermal diffusivity, specific heat capacity and density according to Eq. 3.3. The bulk densities used to obtain the value of thermal conductivity were assumed constant due

to the very small thermal expansion of SiC over the measured temperature range [10]. For the specific heat capacity, reference values for SiC from the literature were considered [10]. The specific heat C_p (J/kg K) can be calculated with an approximated correlation for standard silicon carbide as follows:

$$C_p(T) = 925.65 + 0.3772\,T - 7.9259 \cdot 10^{-5}\,T^2 - \frac{3.1946 \cdot 10^7}{T^2} \qquad \text{Eq. 3.5}$$

where the temperature is in K. It has been shown that SiC materials show very similar heat capacities regardless the microstructure, the grain size, or the α to β SiC content [25].

Compressive-strength

For the study of the mechanical robustness of the samples, compressive-strength tests were performed [27]. Diesel particulate filters in automotive applications will be used under severe vibration conditions. This study is oriented to identify the mechanical behaviour of bioSiC as DPF substrate.

The mechanical characterization was made in terms of compressive strength because a majority of compressive loads are foreseen. The monolith filter is enclosed in a metal housing, so pressure loads may appear due to thermal expansion. On the other hand, due to the channel geometry, no bending or shear loads are expected. Apart from that, compressive strength values can offer an estimation of the resistance to vibrations required for this application.

Parallelepipeds with dimensions of (3 × 3 × 5) mm^3 were cut with a diamond saw and then tested in compression up to failure at a constant strain rate of $2{\cdot}10^{-4}$ s^{-1} at room temperature, using a screw-driven universal testing machine (Microtest EM1/20/FR, Madrid, Spain). The compressive load was applied along the long axis of the samples using alumina rods. The reported maximum compressive strength was the average of a minimum of five measurements for each wood-bioSiC and loading conditions in both directions (axial and radial).

3.3.3. Phase and TGA-DSC analysis

During the manufacturing process of bioSiC elements, the conversion of the carbon matrix into silicon carbide is promoted by the reaction with molten silicon at temperatures above 1500 ºC. At this temperature the silicon melts and is able to permeate trough the pores of the solid carbon structure. The wood precursors used to make the filter samples were all chosen with open porosity; so in general, the silicon reaches the whole internal structure of the carbon matrix. However, the presence of some inaccessible pores, or the insufficient time for reaction in some points, may leave some zones in the carbon matrix unreacted. To check if the structure has reacted completely, or if there is some unreacted carbon, a thermogravimetric analysis has been performed over the bioSiC samples.

On the other hand, to obtain porous biomorphic SiC, the excess Si has to be removed. In this work, the silicon in excess has been removed by capillary extraction and evaporation at high temperature, which means heating the Si/SiC piece up to 1800 ºC. Above 1700 ºC, silicon carbide is susceptible to suffer phase changes in its crystalline structure, from the cubic 3C β-SiC to the high temperature hexagonal 6H α-SiC [28]. This may affect the specific surface of the porous material and to the filtration behaviour. Thus, a phase analysis has been also performed over the samples to identify all major phases present in terms of their crystal structure.

This study is important as long as the elementary composition of the material and its phase structure directly affects its properties. The presence of amorphous carbon for instance reduce the strength and the hardness of the ceramic composite, while the different crystalline phases of silicon carbide present different melting points or stability ranges.

X-Ray diffraction

The X-ray diffraction is based on the scattering that a monochromatic X-ray beam undergoes when it interacts with the atoms of a crystalline material. The interaction of an incident beam with the sample produces a bunch radiation peaks, with different positions and intensities, characteristic of each crystalline substance. By comparing the obtained peaks with the available patterns in the data bases, the crystalline phases can be identified and quantified [29]. The interpretation of XRD is based on Brag law. When an X-Ray beam with a known wavelength is incident to a crystalline solid, the crystalline planes may produce constructive interference or a diffracted ray. According to Bragg`s Law the deflected waves will not be in phase except when the following relationship is satisfied:

$$n\lambda = 2L \sin\theta \qquad \text{Eq. 3.6}$$

where n is a positive integer, θ is the diffraction angle (Bragg angle) for a lattice spacing L and λ is the wavelength of the X-rays. In this work, phase analysis was performed by X-ray diffraction (XRD) employing an X-ray diffractometer (Bruker D8 advance), fitted with a Cu cathode using monochromated Cu Kα radiation (λ = 1.5406 Å). Analyses were carried out in samples before and after the heating process used to remove the excess of silicon.

TGA (Thermogravimetry) + DSC (Differential scanning calorimetry) analysis

To determine the percentage of residual unreacted carbon present in the samples after the infiltration process, thermogravimetry (TGA) and differential scanning calorimetry (DSC) have been used. Thermogravimetry measures the mass change of a sample over time as the temperature evolves. Differential scanning calorimetry, in turn, measures the amount of energy absorbed or released by the sample when it is heated. Both techniques can be applied simultaneously as they use identical test conditions (same atmosphere, gas flow rate, vapor pressure of the sample, heating rate, etc.), and they offer more information applied together than when they are applied in separated tests.

To make these measurements a Q-600 SDT analyser from TA Instruments was used. The equipment was first calibrated with a standard sapphire sample. The bioSiC samples were heated in an oxidizing air atmosphere with a heating rate of 10 ºC min^{-1} up to 1000 ºC (temperature above the combustion temperature of carbon). The residual amount of carbon was estimated from the weight loss associated to the carbon oxidation.

3.3.4. Permeability and intrinsic filtration efficiency

For filtration applications, the permeability is one of the most important properties because it is directly related to the pressure losses in the flow [30]. Recent studies have been conducted on some ceramic materials to determine their permeability and to assess the influence of their microstructure on the resulting pressure drop and capture efficiency [31,32]. These parameters have been demonstrated to depend on volume fraction of porosity as a first approximation, but also on the pore size and connectivity [33]. If the permeability is known as a function of the microstructure, then the pressure drop can be predicted under a given flow rate and the microstructure can be improved by tailoring pore characteristics [34]. However, high values of porosity cause lower mechanical strength and stability [6,8,23], despite the high permeability [35], and thus finding the balance between the two parameters is one of the main challenges in making a suitable material for filtering applications.

Permeability

The pressure drop of a gas flowing through a porous material is described as follows through the Forchheimer's equation [36], determined by the Darcy's law and Forchheimer's extension:

$$\frac{\Delta P}{L} = \frac{\eta}{k_1} v + \frac{\rho}{k_2} v^2 \qquad \text{Eq. 3.7}$$

where ΔP is the pressure drop (Pa), L is the thickness of the sample (m), η is the dynamic viscosity (Pa·s), v is the gas velocity ($m \cdot s^{-1}$), ρ the gas density ($kg \cdot m^{-3}$) and k_1 and k_2 are the Darcian (m^2) and inertial (m) permeabilities respectively. In the case of compressible fluids, the pressure is determined by the difference in the squares of input (P_i) and output (P_o) pressure, and is determined as follows:

$$\Delta P = \frac{P_i^2 - P_o^2}{2P_o^2} \qquad \text{Eq. 3.8}$$

A laboratory-made gas permeameter device was designed and built within this research work to characterize the permeability of the bioSiC specimens. Figure 3.8 shows a photo of the manufactured apparatus and Figure 3.9 presents its basic operating diagram. This experimental apparatus has been described in [23,37].

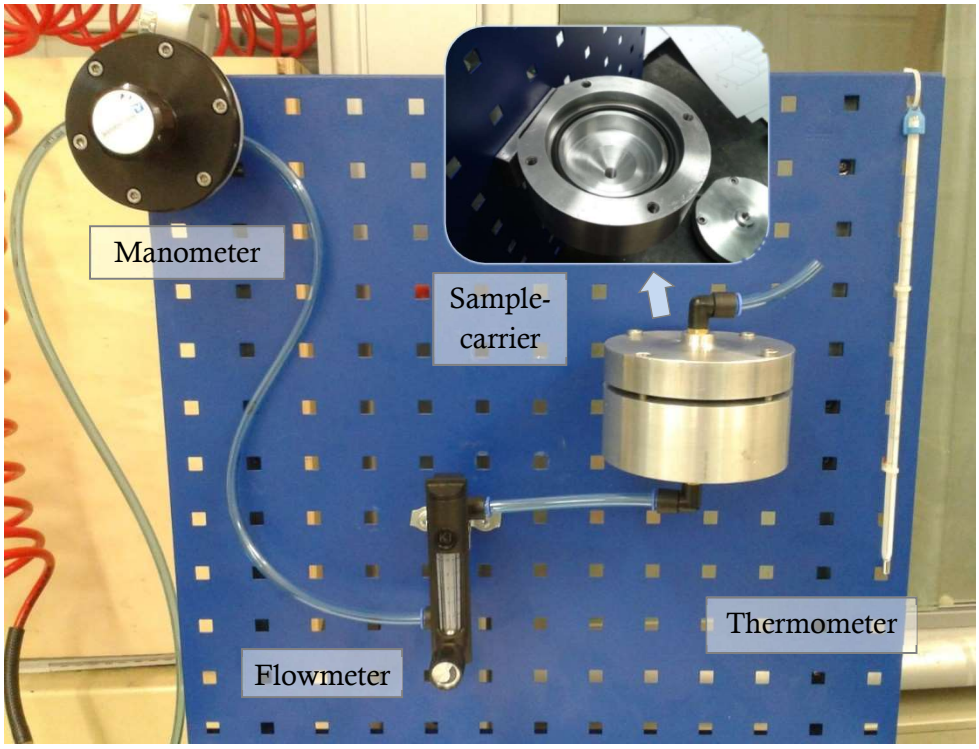

Figure 3.8. Laboratory-made permeameter built for this work

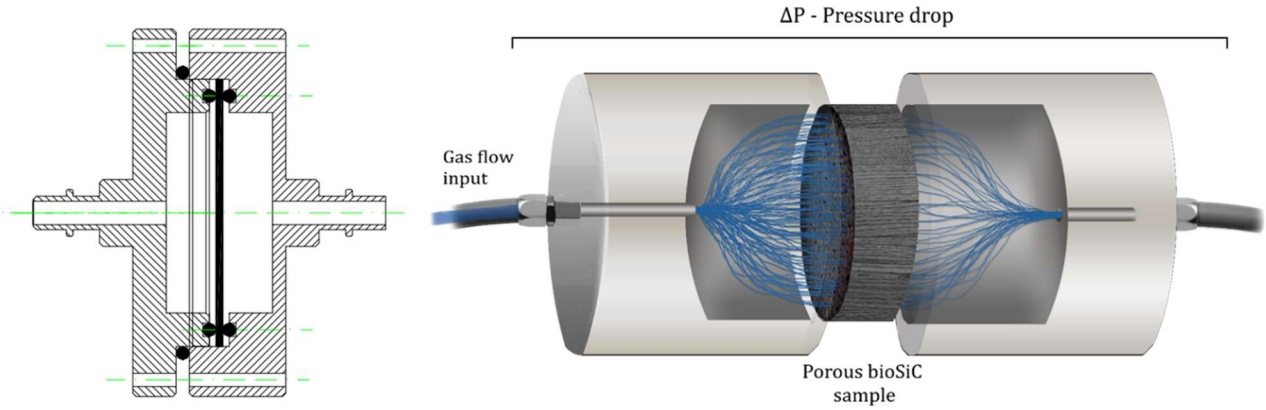

Figure 3.9. Design sketch of the sample carrier and operating diagram of the permeameter

The disk-shaped samples were inserted in this permeameter in sealed clamps, and a gas flow was forced to cross them while the pressure and the gas flow were being measured. The gas flow through the sample was measured with a rotameter, while the pressure drop was measured with a gas manometer with measurement range from 1 to 9 kPa. Compressed air at room temperature was used as working fluid. The density and the dynamic viscosity for the room temperature were taken from the general literature ($\eta = 1.8 \cdot 10^{-5}$ Pa·s, $\rho = 1.17$ kg·m^{-3}) [38]. The system calibration was made measuring the pressure drop without any sample. The gas-flow velocity ν was determined by the measured volumetric flow rate Q per unit of cross-sectional area A (m^2) perpendicular to the flow direction (ν = Q/A).

The experimental curves of pressure drop as a function of flow velocity were fitted according to Forchheimer's equation for compressible fluids. From these quadratic fits, permeability constants, k_1 and k_2, were determined according to Eq. 3.7. Both parameters were considered constant and independent of the flow conditions because they have been found to depend only on the relevant microstructural parameters, such as morphology, pore-size distribution, porosity fraction or connectivity [32]. Darcy's law considers only the pressure drop associated with laminar viscous effects at very low flow velocities, reflecting a linear behaviour between the pressure drop and the air-flow velocity in a porous medium. However, also considering Forchheimer's extension for higher velocities, the pressure gradient shows a more realistic parabolic trend due to turbulence and inertial effects [39]. The permeability values reported in the following chapter (Chapter 4) are the average of the measurement of three samples for each type of wood precursor and orientation.

Intrinsic filtration efficiency

Before tackling the manufacture of the final filter prototypes with the complex geometry of an automotive wall-flow DPF, it was convenient to get a first idea of the filtration performance of the different bioSiC specimens included in this characterization study (made from different precursors and with different cutting directions). The filtration efficiency of a filter depends on its thickness and on the flow velocity [40], which in turn depends on the filtration area. Hence, despite being made from the same material, the filtration efficiency of a wall-flow DPF differs from that of a simple disk-shaped filter. Nevertheless, to make a comparative analysis between the different bioSiC specimens, and to help in making a decision on which precursor to use for manufacturing the final prototypes, a preliminary study on the filtration efficiency of the disk-shaped samples has been carried out.

The study was carried out taking advantage of the facilities already operating in the Laboratory of Thermal Engines of the University of Seville. An experimental test bench was designed and built in order to extract a fraction of the exhaust gases coming from a diesel boiler, and to direct it towards the measurement section of the rig, where the filtering performance of the bioSiC disk-shaped specimens was tested under controlled conditions, suitable for the size of the samples.

For this study, a small industrial diesel-fuelled boiler was used. This thermal system integration is considered suitable to evaluate the filtering performance of simple disk-shaped samples. At the Laboratory of Thermal Engines, this boiler is used to heat thermal oil up. This thermal oil flows through a closed loop: it comes from a storage tank, it is heated up in the boiler, then it is cooled down in a heat exchanger, and finally it returns to the tank. The boiler doesn't operate constantly but through temperature regulated start-stop cycles as a function of the oil temperature. Therefore, the system performance is characterized by frequent start-stop cycles where certain amount diesel soot is generated. Table 3.2 shows the main technical specifications of the boiler.

Table 3.2. Technical specifications of the boiler

SOGECAL Thermal Oil Boiler [41]

Manufacturer	SOGECAL
Model	ORK KONUS-ORBUS
Type	CL-100
Power	116 kW
Thermal fluid	Oil
Oil Max. Temperature	400 °C
Oil Max. Pressure	20 bar

In this work an experimental test bench has been designed and built to extract a fraction of the boiler exhaust flow and filter it under controlled conditions, adequate for the samples size and for the integrity of the measurement equipment. The bench was integrated with the boiler by connecting the sampling pipe to the boiler exhaust. Figure 3.10 depicts the general scheme of the test bench, with the sampling point located in the centre of the flue gases pipe. In Figure 3.11 two images of the experimental facility are presented. On the left hand side, a photograph of the boiler is presented; and in the right hand side, a detail of the test rig.

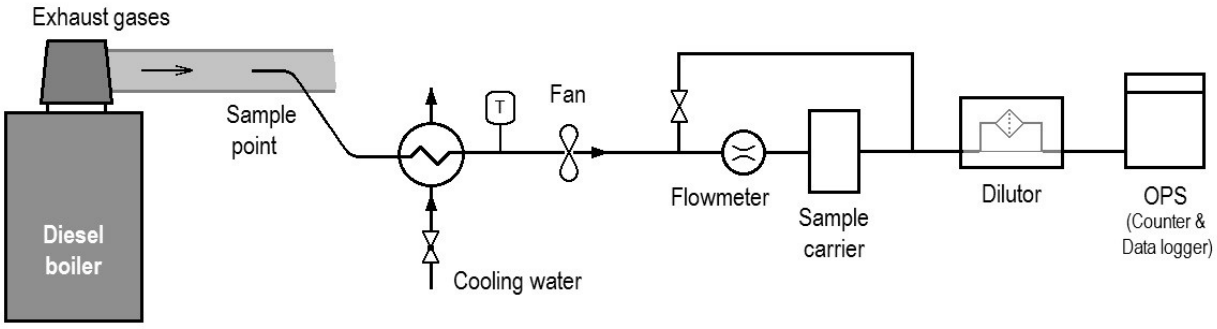

Figure 3.10. Test bench layout for the measurement of the intrinsic filtration efficiency of the lab-scale bioSiC samples (tests in a diesel boiler)

First checks included measuring the temperature of the exhaust gases as a function of the oil target temperature in order to ensure that the gas sample didn't exceed the thermal limit of the components downstream. When the target temperature of the oil was set to 50 ºC, the temperature of the flue gases was up to 190 ºC in the sampling point, and up to 65 ºC at the end of the flexible metal pipe. To maintain the integrity of the particles measurement equipment, a plate water-cooled heat exchanger was placed just between the connection flexible pipe and the measuring space. It assures a safe 35 ºC temperature at the inlet of the particle counter.

Figure 3.11. Experimental facility for the preliminary measurement of the filtration efficiency: diesel boiler (left) and test rig (right).

The thermo-couple located just after the heat exchanger provided a live measurement of the sample temperature. To compensate the pressure losses produced by the heat exchanger, a small blower was placed at its outlet. Both, thermocouple and blower, were attached to a metal tube (Figure 3.12) with an ending conical section manufactured to adapt the section of the heat exchanger to the section of the remaining piping. All metal components in this first area of the bench were provided with an earth connection to avoid particulates to stick due to accumulated static charge. Right after it, in the measuring space of the bench, all the piping was designed with antistatic tubes.

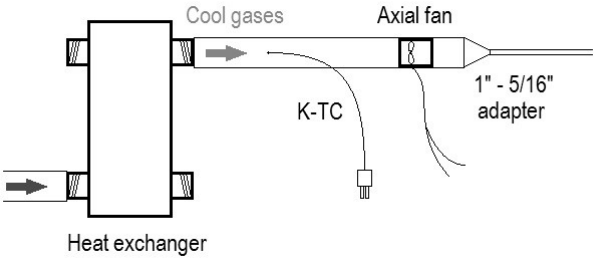

Figure 3.12. Attachment of the thermocouple (K-TC) and the fan to the heat exchanger

From this point, gases may be carried directly to the measuring area if the original particulate concentration produced by the boiler is going to be measured, or forced to pass through the filter when testing any sample. The sample-carrier used for these test was the same sample-carrier used for the permeability tests, which consisted of an airtight chamber with a junction-sealed support (see Figure 3.9). Both inlet and outlet sections of the chamber were turned and provided with smooth conical shapes to improve its aerodynamics. The sample is placed in the carrier laying between two o-rings in order to force the gas to pass through it.

To measure the number and the distribution of particles in the gas stream an Optical Particle Sizer has been used (TSI Optical Particle Sizer, OPS 3330). The general specifications of the particle meter may be seen in Table 3.3. To avoid surpassing the limit of 3000 particles/cm^3 imposed by the OPS, a stream dilutor was placed upstream the measuring device. Eventually, this dilutor might be detached if the concentration of particles was low enough. The flow rate that enters the

OPS is governed by an internal pump and is set to 1 LPM. To check the correct performance of the pump and to be able to calibrate the flow, an analogic rotameter was placed between the dilutor and the OPS.

Table 3.3. Technical specifications of the optical particle sizer

OPS 3330 Optical Particle Sizer [42]	
Manufacturer	TSI
Model	OPS 3330
Measurement Principle	120° light scatter
Flow rate	1 LPM ± 5%
Sampling time	≥ 1 s
Particle size range	0.3-10 μm
Channels no.	16
Size resolution	5% at 0.5 μm
Particle concentration limit	3000 particle/cm^3

3.4. Small-scale prototypes of wall-flow DPFs made of bioSiC

As explained at the beginning of this chapter, this thesis was developed in two main stages.

The first stage was devoted to manufacture the laboratory samples and to perform the complete material characterization study. This study allows a better understanding of the material properties and the potential of the different bioSiC specimens for their integration in a real DPF prototype.

The second stage was focused on manufacturing a wall-flow DPF prototype with real geometry and evaluating its filtration performance through an experimental campaign. The prototypes were characterized at lab-scale by means of a Soot Generator (SG). A SG produces a controlled concentration of particles in terms of mass and distribution. They are frequently used for characterizing automotive filters as they can generate particles distributions similar to the ones produced by a diesel engine. Their use facilitates the control of the test conditions, provides a higher accuracy in the results, and assures the repeatability of the experiments allowing a better understanding of the effect of different factors in the filters performance.

The SG test bench could not hold large-scale filters, so the prototypes had to be designed at a smaller scale. The final size of the prototypes was 9.2 mm x 9.2 mm x 31 mm. They were made with a total of 45 channels: 21 inlet and 24 outlet channels, which results in a cell density of 57.59 cell/cm^2 (371.6 cpsi). The results of the experimental study were scaled up to a full-size DPF by means of a validated numerical model, adapted to the specific microstructural features of bioSiC, as will be explained in Section 3.6.

Precursor selection

The wall-flow prototypes were manufactured from MDF. This decision was based on the results of the precursors characterization study, which will be presented in the following chapter (see Section 4.5). Results revealed that MDF had, along with Axial Pine, one of the best filtration efficiencies among all studied precursors. The precursor selection for the manufacture of a pilot-scale prototype was based mainly on efficiency criteria. The reason for this is because the only objective limitation over these systems is imposed by the regulations and it affects the number and the mass of particles they can retain. However, the choice of the precursor was in this case due to both technical and practical reasons. MDF-bioSiC is easier to process than natural precursors: it is a transversely isotropic material with homogeneous microstructure, that remains homogeneously soft after the pyrolysis. This in practice eased the mechanizing process. In contrast, the densest fringes of the growth rings of Pine wood became too hard in the resulting carbon pieces, and they could not be mechanized with the same fine tools.

Cutting direction

From the initial characterization study, it was determined that, when an MDF-bioSiC filter is arranged with the compression direction parallel to the gas flow (perpendicular to the fibres), its permeability is around $1 \cdot 10^{-12}$ m^2 [27], and an initial (clean) filtration efficiency higher than 80% may be expected [9] (the values of permeability and intrinsic filtration efficiency obtained from the characterization study are presented in Section 4.4).

In a wall-flow DPF, the crossing direction of the gases through the porous substrate is perpendicular to the direction of the channels. In a bioSiC DPF this fact is especially significative due to its natural anisotropy. In particular, in a MDF-bioSiC filter, if the channels are mechanized in the compression direction, then the gas flows perpendicular to the compression direction. In this work, the mechanizing direction was chosen based on manufacturing criteria. MDF is generally served in thin panels (no thicker than 2-3 cm); and taking into account the mechanizing process followed in this work (described below in the text) this resulted the simplest way.

No data have been found about its behaviour in the other direction, with the compression direction perpendicular to the gas flow, but the homogeneity in the arrangement of the fibres leads to think that maybe a lower permeability and a higher filtration efficiency can be expected. As a part of this study, the permeability of MDF-bioSiC in the direction perpendicular to the compression one has been determined.

Fabrication process

After selecting the most appropriate precursor, and upgrading the manufacturing process, the real prototypes of wall-flow DPFs were manufactured. The prototypes were manufactured following the manufacturing procedure described in Section 3.2, but adapting the process to the complex geometry of wall-flow DPFs and paying special attention in the mechanizing stage to the

geometry and optimal design of the honeycomb structure required for diesel engine applications. Figure 3.13 shows a diagram with the main stages of the process after the adaptation.

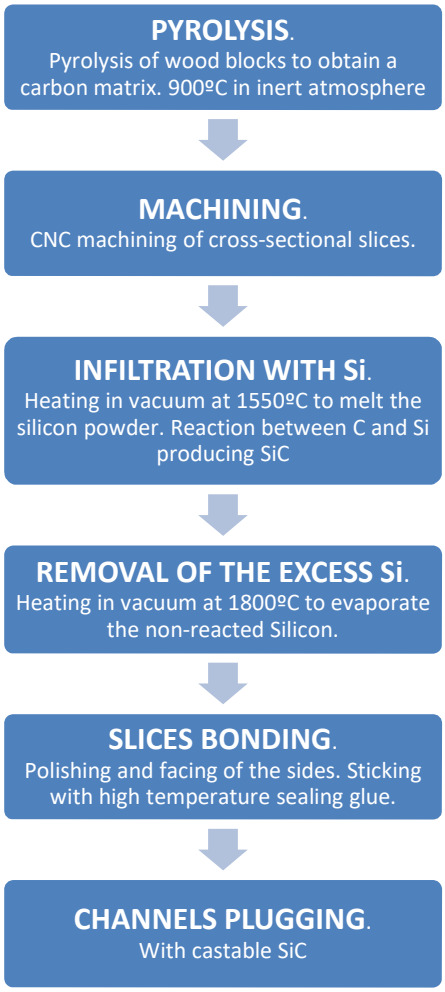

Figure 3.13. Main stages of the manufacturing process of bioSiC

The starting material was a panel of MDF. It was at this stage of the research when the implications of the wall-flow DPF geometry and the direction of the gas flux within were assumed. Due to the limited thickness of the MDF panels, during the characterization study, MDF samples were cut and tested in only one direction. The lab-scale disk-shaped samples were cut with the axis parallel to the compression direction; and all the tests were performed as if the gas flux was going to cross the MDF porous substrate in this same direction. Nevertheless, in a wall-flow DPF, the gas flows across the walls of the channels. Depending on how the MDF panels are cut and arranged to make the prototype, the final crossing direction of the gas may result perpendicular to the compression direction of the fibres instead of parallel. In order to take this into consideration, the permeability study of the MDF-bioSiC specimens was complemented with additional permeability tests over the final prototypes.

The MDF panels were pyrolyzed heating them up to 900 °C in an oxygen-poor atmosphere using a slow heating ramp in order to obtain carbon plates. The main novelty of the process followed in this work is the way the wall-flow samples were mechanized from the carbon plate. In this

work the wall-flow filters were constructed by manufacturing a number of cross-sectional slices and sticking them later with high temperature sealing glue. The cross-sectional slices were mechanized in a Computer Numerical Control (CNC) milling machine (EMCO Concept Mill 105). Figure 3.14 shows one of the mechanized slices, and the aspect of the samples, still made of carbon and not stuck.

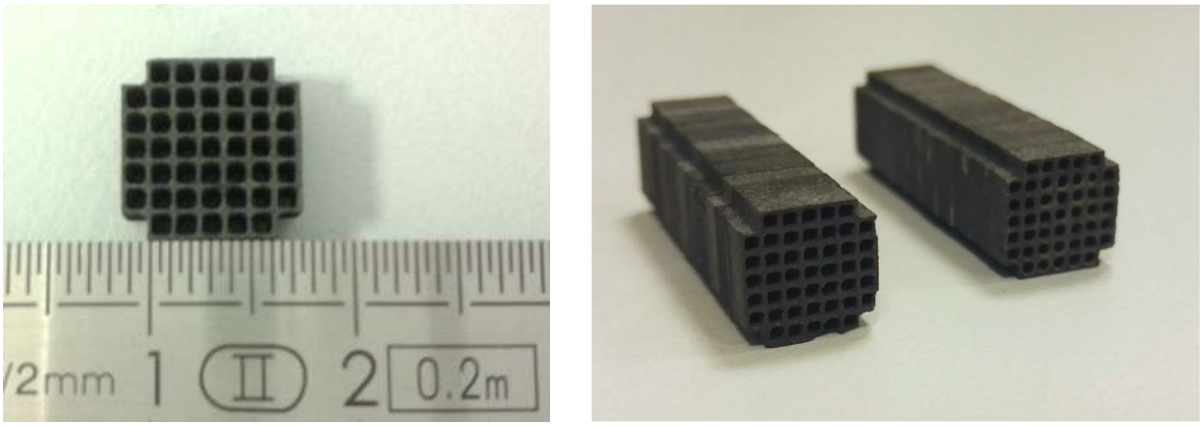

Figure 3.14. One of the mechanized slices (left) and final aspect of the whole prototypes before the infiltration with silicon

These carbon slices were then infiltrated with silicon in order to get the final product of silicon carbide. For this purpose, they were placed in a crucible, covered with silicon powder (Silgrain HQ-99.7% purity; Eljem Silicon) with a Si:C mass ratio of 3.5, and then heated up to 1550 °C for 30 minutes in vacuum (Figure 3.15).

Figure 3.15. Carbon slices of the prototype in the crucible covered with silicon

After the infiltration process, the initial carbon structure has turned into silicon carbide and the unconsumed silicon is filling and blocking the pores. This excess silicon is removed by evaporation at high temperature. The pieces were placed again in crucibles surrounded by carbon pieces and heated up to 1800 °C in vacuum. After this process, the cross-sectional slices of the wall-flow filter are already made of porous bioSiC.

To assure a perfect joint between them, their sides are first faced and polished. The slices were stuck with high temperature sealing glue (Nural 30, Pattex) paying special attention to cover the whole surface of the channels, but without blocking the path for the gas. The microstructure of the resulting biomorphic SiC filter from MDF wood was analysed by X-ray computed tomography (XCT) in order to check the reliability of the bonding stage. Measurements were carried out using a tomographic scan model Y.Cougar SMT (YXLON), which consisted of a cone-beam system with a total rotational angle of 360º equipped with a microfocus tube and a target transmissive of Tungsten. While the sample was rotating, 1024 radiographic projections of the internal structure of the material were collected by a CCD camera. The data output from XCT was processed (filtered and segmented into two phases: pores and the ceramic phase of SiC) using the software Avizo Fire 8.1. which allows to render and visualize the full three- dimensional features of the biomorphic wall-flow filter. A three-dimensional rendering of the X-ray Computed Tomography analysis is shown in Figure 3.16 to illustrate the structure of the bioSiC filter, where it can be observed the appearance and interconnection of the square parallel cells characteristic of honey-comb structures. As can be appreciated in Figure 3.16, the bonding was made successfully since all the slices were sticked without leakages and none of the channels was blocked.

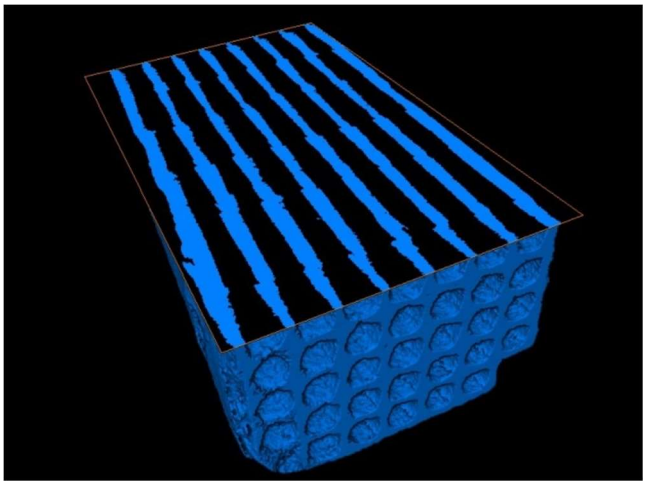

Figure 3.16. Three-dimensional rendering of the XCT analysis carried out over the wall-flow bioSiC filter prototype

The last stage of the manufacturing process is plugging the ends of the channels. To make this, a Castable Refractary Alumina (Rescor castable ceramics 780, Cotronics) was used mixing 1 part of activator with 4 part of powder and putting the resulting slurry in the end of the channel carefully with a needle. After 1 hour at ambient temperature the mixture sets hard. The aspect of the plugged channels can be seen in Figure 3.19.

Following the procedure described above, up to six MDF-bioSiC wall-flow DPF prototypes were manufactured. The manufacturing process was challenging and it involved mainly manual work procedures. After an inspection of final products, the two best prototypes were chosen for the final tests and the rest was disregarded. Throughout the text, these samples will be referred as to S1 and S2. Table 3.4 summarizes the main geometrical specifications of the samples. In principle,

both samples were made equally, so that no difference in behaviour between them might be expected except for the arbitrariness of the microstructure in the wooden precursor and manufacturing accuracy and tolerances.

Table 3.4. Geometrical specifications of the prototypes

MDF-bioSiC wall-flow DPF prototypes	
External dimensions	9.2 mm x 9.2 mm x 31 mm
Frontal area	$7.814 \cdot 10^{-5}$ m^2
Volume	$2.422 \cdot 10^{-6}$ m^3
Number of channels	45
Inlet channels	21
Outlet channels	24
Cell density	57.59 cell/cm^2 (371.6 cpsi)

3.5. Experimental measurement of filtration efficiency and pressure drop

The prototypes described above, were characterized at lab-scale by means of a Soot Generator (SG). The SG produces a gas stream with a controlled emission of particles. They can generate particles concentrations and distributions similar to those produced by internal combustion engines, but they have several advantages. Their use facilitates the control of the test conditions, provides a higher accuracy in the results, and assures the repeatability of the experiments allowing a better understanding of the effect of different factors in the filters performance. Each prototype was subject to three filtration tests and regenerated after each one to remove the deposited soot and start over again with the clean filter. A Scanning Mobility Particle Sizer (SMPS) was used to measure the concentration of particles upstream and downstream the filter, so that the filtration efficiency of the samples could be calculated. At the same time, a differential pressure sensor was used during the tests in order to determine the pressure drop introduced by the filter and to monitor it as a function of the soot load. Tests were performed at constant flow rate, setting a value of Space Velocity that the author considered illustrative for the application as explained below.

Experimental setup

The test bench was designed to carry out filtration tests but included a reactor to regenerate the samples too. The experimental layout is shown in Figure 3.17.

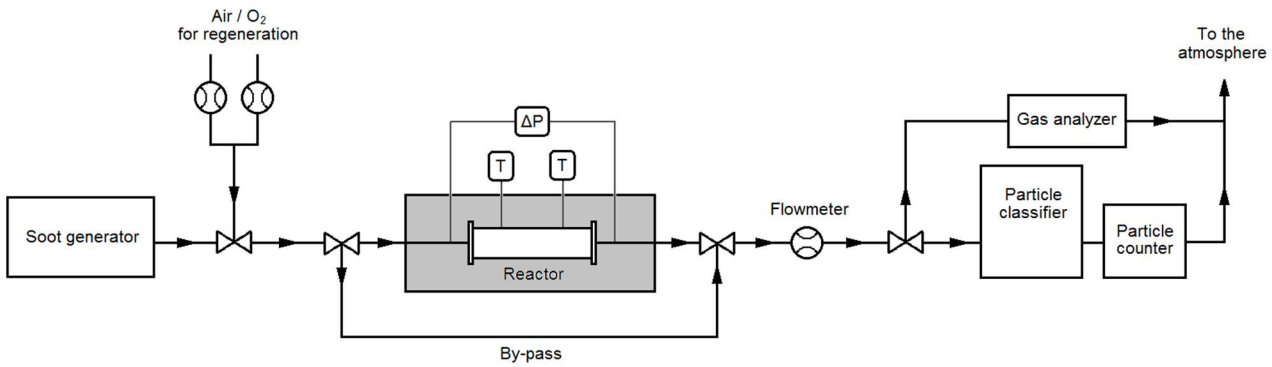

Figure 3.17. Test bench layout

The SG (PALAS GFG 1000) generates a condensation aerosol from monolithic graphite within an argon stream. Each sample was subject to three successive filtration tests. The tests were performed setting the argon volume flow to 5 LPM (1.2 bar). Taking into account the volume of the samples, this implies a Space Velocity of around 120000 h^{-1}. According to the specifications of the SG, a spark frequency of 200 sparks/s leads in those conditions of pressure to a production of 4 mg of soot per hour. This value was checked afterwards with the measurements of the SMPS and the CPC (Condensation Particle Counter). Table 3.5 summarizes all the experimental procedure followed with the samples.

Figure 3.18. Photograph of the test bench

A by-pass loop was mounted in order to measure the distribution of particles upstream the filter samples, just as it comes from the SG. The filter samples were placed inside a canning, where two k-type thermocouples and a differential pressure sensor were connected. The thermocouples, which were not necessary during the filtration tests, since they were performed at ambient temperature, were used to register the evolution in temperature during the regeneration processes.

Table 3.5. Summary of the experimental procedure

Number of samples	2 (S1, S2)
Number of filtration tests	3 for each sample
Test conditions	5 LPM Argon ; 200 sparks/s
Space velocity	120000 h^{-1}
Test length	> 5 h
Measured parameters	ΔP, N_{in}, N_{out}
Regeneration	2.5 LPM air + 2.5 LPM N_2 5 ºC/min up to 650 ºC 3 hours dwell

Downstream the reactor, a flow-meter was used to check the correct gas flow. After that, a valve leads the exhaust gases towards the measuring area where the SMPS (TSI 3080 SMPS), consisting of an impactor (0.0508 cm), an electrostatic classifier, a differential mobility analyser (TSI 3081), and a condensation particle counter (TSI 3025A), was used to count and measure the distribution of particles at the outflow. The length of the filtration tests was around 5 hours to assure the formation of the cake on the surface of the substrate. In the SMPS, a scan length of 135 s is set. The filtration tests were carried out without dilution since the reduction in particles concentration due to the filters was enough to fit the requirements of the SMPS. However, during the measurement of the original particles distribution of the SG, a dilution system was used consisting of two ejector diluters in series (Dekati Ltd.). Each stage provided a dilution factor of about 8, so an overall dilution factor of 64 was obtained.

Figure 3.19. Final aspect of the samples in the cordierite adaptor (left) and fitting of the samples inside the canning (right)

In order to fit the samples inside the canning and assure that there were not any leakages, a cordierite holder and a vermiculite mop were used, both covered with a sealant layer of Castable Refractary Alumina as the one used to plug the ends of the channels. Usage of the adaptor has been necessary since we wanted a little DPF, with great possibility of ranging in special velocities, to be tested in cylindrical canning with enough space for thermocouples and pressure sensors. The result can be seen in Figure 3.19.

The position of the thermocouples was also meticulously controlled. Since the canning was long and opaque, two guides were manufactured to guide the thermocouples along the axis of the canning and place their tips just next to the filter surfaces. Being aware of the extra pressure drop that all these devices (the holder for the sample and the guides for the thermocouples) may produce, it was decided to perform a zero test with all the elements except the samples. The results of this zero test are presented in Chapter 4 along with the rest of the results of the experimental campaign.

After each filtration test, the samples were regenerated with a heating rate of 5 °C/min up to 650 °C followed by a soak time of 3 hours. A gas stream with 50% nitrogen and 50% air was used. This makes a mixture with 10% oxygen, according to the standard testing procedure described by Miceli et al. [43], which recreates the same air mixture of a real scale DPF regenerating. This gas stream was connected to the bench through a valve before the canning. The flow rates of nitrogen and air are set with the aid of two flow-meters.

The heat for the regeneration is supplied in the reactor. The reactor encloses the canning of the filter and acts as a furnace by means of a number of electrical resistances. Finally, in order to vent the dirty gases out of the room, a venting pipe was connected that carried the gases directly to the exterior. Before starting the experimental campaign, all flow-meters and analysers were calibrated and a characterization of the SG was done as presented in Chapter 6 (Section 6.2.2).

3.6. Numerical model

3.7. Summary of the methodology

This chapter gathers all the experimental and numerical procedures used for the development of this thesis. As recurrently commented, the research was planned in two well differentiated stages. In the first stage, laboratory samples were manufactured from different precursors, and a comprehensive characterization study was carried out to obtain a physical and microstructural description representative for the target application, which is the use of this material as substrate for DPFs in automotive engines. In the second stage, a more specific study up to the system level was carried out. An MDF-bioSiC wall-flow DPF prototype with real geometry was manufactured, tested under real operating conditions, and numerically scaled up to a real-scale system.

This chapter has provided a detailed description of the manufacturing processes at both scales, but specially for the wall-flow prototypes since it differs considerably from the manufacturing process of the extruded ceramic monoliths currently used in commercial DPFs, and it was specifically designed for the development of this thesis.

In this chapter, the techniques used to characterize the material have been presented with an explanation of the theory that support them, and specific information about the equipment used for the analyses has been provided. In the following chapter, Chapter 4, the results of the characterization study are shown with a preliminary analysis, which is further extended in Chapter 5. This chapter has also described the experimental procedure to test the prototypes and the numerical model used to simulate their performance. The results corresponding to this part of the research are presented in Chapter 6.

References

[1] Bautista MA, De Arellano-López AR, Martínez-Fernández J, Bravo-León A, López-Cepero JM. Optimization of the fabrication process for medium density fiberboard (MDF)-based biomimetic SiC. Int J Refract Met Hard Mater 2009;27:431–7. doi:10.1016/j.ijrmhm.2008.10.016.

[2] De Arellano-López AR, Martínez-Fernández J, González P, Domínguez C, Fernández-Quero V, Singh M. Biomorphic SiC: A New Engineering Ceramic Material. Int J Appl Ceram Technol 2005;1:56–67.

[3] Singh M, Martínez-Fernández J, De Arellano-López AR. Environmentally conscious ceramics (ecoceramics) from natural wood precursors. Curr Opin Solid State Mater Sci 2003;7:247–54. doi:10.1016/j.cossms.2003.09.004.

[4] Varela-Feria FM, Martínez-Fernández J, De Arellano-López AR, Singh M. Low density biomorphic silicon carbide: microstructure and mechanical properties. J Eur Ceram Soc 2002;22:2719–25.

[5] Bautista MA. Fabricación, caracterización y propiedades mecánicas del SiC biomórfico obtenido a partir de paneles de fibra de madera de densidad media. 2014.

[6] Torres-Raya C, Hernández-Maldonado D, Ramírez-Rico J, Garcia-gañan C, De Arellano-López AR, Martínez-Fernández J. Fabrication, chemical etching, and compressive strength of porous biomimetic SiC for medical implants. J Mater Res 2008;23:3247–54. doi:10.1557/JMR.2008.0392.

[7] Schwartz B, Robbins H. Chemical Etching of Silicon. J Electroch Soc 1961;108:365–72.

[8] Kaul VS, Faber KT, Sepúlveda R, De Arellano-López AR, Martínez-Fernández J. Precursor selection and its role in the mechanical properties of porous SiC derived from wood. Mater Sci Eng A 2006;428:225–32. doi:10.1016/j.msea.2006.05.033.

[9] Orihuela MP, Gómez-Martín A, Becerra-Villanueva JA, Chacartegui R, Ramírez-Rico J. Performance of biomorphic Silicon Carbide as particulate filter in diesel boilers. J Environ Manage 2017;203:907–19. doi:10.1016/j.jenvman.2017.05.003.

[10] Snead LL, Nozawa T, Katoh Y, Byun T, Kondo S, Petti DA. Handbook of SiC properties for fuel performance modeling. J Nucl Mater 2007;371:329–77. doi:10.1016/j.jnucmat.2007.05.016.

[11] Leon y Leon C. New perspectives in mercury porosimetry. Adv Colloid Interface Sci 1998;76:341–72.

[12] Lowell S, Shields JE, Thomas MA, Thommes M. Surface Area Analysis from the

Langmuir and BET Theories. Charact Porous Solids Powders Surf Area, Pore Size Density 2004;16:58–81.

[13] Nemoto A, Iwasaki K, Yamanishi O, Tsuchimoto K, Uoe K, Toma T, et al. Development of Innovative Diesel Particulate Filters based on Aluminum Titanate: Design and Validation. 2011.

[14] Parfen'eva LS, Orlova TS, Kartenko NF, Sharenkova N V., Smirnov BI, Smirnov IA, et al. Thermal and electrical properties of a white-eucalyptus carbon preform for SiC/Si ecoceramics. Phys Solid State 2006;48:441–6. doi:Doi 10.1134/S1063783406030061.

[15] Parfen'eva LS, Orlova TS, Kartenko NF, Sharenkova N V., Smirnov BI, Smirnov IA, et al. Thermal conductivity of high-porosity heavily doped biomorphic silicon carbide prepared from sapele wood biocarbon. Phys Solid State 2009;51:2023–31. doi:10.1134/S1063783412080240.

[16] Parfen'eva LS, Orlova TS, Kartenko NF, Sharenkova N V., Smirnov BI, Smirnov IA, et al. Thermal conductivity of high-porosity biocarbon preforms of beech wood. Phys Solid State 2010;52:1115–22. doi:Doi 10.1134/S1063783410060028.

[17] Pappacena KE, Faber KT, Wang H, Porter WD. Thermal conductivity of porous silicon carbide derived from wood precursors. J Am Ceram Soc 2007;90:2855–62. doi:10.1111/j.1551-2916.2007.01777.x.

[18] Pappacena KE, Johnson MT, Wang H, Porter WD, Faber KT. Thermal properties of wood-derived copper-silicon carbide composites fabricated via electrodeposition. Compos Sci Technol 2010;70:478–84. doi:10.1016/j.compscitech.2009.11.011.

[19] Johnson MT, Childers AS, Ramírez-Rico J, Wang H, Faber KT. Thermal conductivity of wood-derived graphite and copper-graphite composites produced via electrodeposition. Compos Part A Appl Sci Manuf 2013;53:182–9. doi:10.1016/j.compositesa.2013.06.009.

[20] Greil P, Lifka T, Kaindl A. Biomorphic cellular silicon carbide ceramic from wood: II. Mechanical Properties. J Electrochem Soc 1998;18:1975–83.

[21] Martínez-Fernández J, Varela-Feria FM, Singh M. High Temperature Compressive Mechanical Behavior of Biomorphic Silicon Carbide Ceramics. Scr Mater 2000;43:813–8.

[22] Presas M, Pastor JY, LLorca J, De Arellano-López AR, Martínez-Fernández J, Sepúlveda RE. Mechanical behavior of biomorphic Si/SiC porous composites. Scr Mater 2005;53:1175–80. doi:10.1016/j.scriptamat.2005.07.033.

[23] Bautista MA, Cancapa JQ, Martínez-Fernández J, Rodríguez MA, Singh M. Microstructural and mechanical evaluation of porous biomorphic silicon carbide for high temperature filtering applications. J Eur Ceram Soc 2011;31:1325–32. doi:10.1016/j.jeurceramsoc.2010.06.014.

[24] Parker WJ, Jenkins RJ, Butler CP, Abbott GL. Flash method of determining thermal diffusivity, heat capacity, and thermal conductivity. J Appl Phys 1961;32.

[25] Gómez-Martín A, Orihuela MP, Ramírez-Rico J, Chacartegui R, Martínez-Fernández J. Thermal conductivity of porous biomorphic SiC derived from wood precursors. Ceram Int 2016;42:16220–9. doi:10.1016/j.ceramint.2016.07.151.

[26] Clark LMI, Taylor RE. Radiation loss in the flash method for thermal diffusivity. J Appl Phys 1975;46.

[27] Gómez-Martín A, Orihuela MP, Becerra-Villanueva JA, Martínez-Fernández J, Ramírez-

Rico J. Permeability and mechanical integrity of porous biomorphic SiC ceramics for application as hot-gas filters. Mater Des 2016;107:450–60. doi:10.1016/j.matdes.2016.06.060.

[28] Rashed H. Properties and Characteristics of Silicon Carbide. Decatur TX: Poco Graphite Inc.; 2002.

[29] Warren BE. X-ray Diffraction. Courier Co. 1969.

[30] Adler J. Ceramic Diesel Particulate Filters. Int J Appl Ceram Technol 2005;2:429–39. doi:10.1016/B978-0-12-385469-8.00032-0.

[31] Dey A, Kayal N, Chakrabarti O, Caldato RF, André CM, de Mello Innocentini MD. Permeability and Nanoparticle Filtration Assessment of Cordierite-Bonded Porous SiC Ceramics. Ind Eng Chem Res 2013;52:18362–18372.

[32] Moreira EA, de Mello Innocentini MD, Coury JR. Permeability of ceramic foams to compressible and incompressible flow. J Eur Ceram Soc 2004;24:3209–18. doi:10.1016/j.jeurceramsoc.2003.11.014.

[33] Topates G, Petasch U, Adler J, Kara F, Mandal H. Production and permeability of porous Si3N4 ceramics produced by starch addition. J Asian Ceram Soc 2013;1:257–61. doi:10.1016/j.jascer.2013.06.002.

[34] Topates G, Mammitzsch L, Petasch U, Adler J, Kara F, Mandal H. Microstructure–permeability relation of porous β-Si3N4 ceramics. J Eur Ceram Soc 2013;33:1545–51. doi:10.1016/j.jeurceramsoc.2012.12.022.

[35] Kumar A, Mohanta K, Kumar D, Parkash O. Low cost porous alumina with tailored gas permeability and mechanical properties prepared using rice husk and sucrose for filter applications. Microporous Mesoporous Mater 2015;213:48–58. doi:10.1016/j.micromeso.2015.04.004.

[36] Najmi H, El-Tabach E, Chetehouna K, Gascoin N, Falempin F. Effect of flow configuration on Darcian and Forchheimer permeabilities determination in a porous composite tube. Int J Hydrogen Energy 2016;41:316–23. doi:10.1016/j.ijhydene.2015.10.054.

[37] Wang B, Zhang H, Phuong HT, Jin F, Yang JF, Ishizaki K. Gas permeability and adsorbability of the glass-bonded porous silicon carbide ceramics with controlled pore size. Ceram Int 2015;41:2279–85. doi:10.1016/j.ceramint.2014.10.032.

[38] Kadoya K, Matsunaga N, Nagashima A. Viscosity and Thermal Conductivity of Dry Air in the Gaseous Phase. J Phys Chem Ref Data 1985;14:947.

[39] de Mello Innocentini MD, Salvini VR, Pandolfelli VC, Coury JR. Assessment of Forchheimer's Equation to Predict the Permeability of Ceramic Foams. J Am Ceram Soc 1999;82:1945–8.

[40] Yang J, Stewart M, Maupin G, Herling D, Zelenyuk A. Single wall diesel particulate filter (DPF) filtration efficiency studies using laboratory generated particles. Chem Eng Sci 2009;64:1625–34. doi:10.1016/j.ces.2008.12.011.

[41] ORK-Generators. ORK KONUS-ORBUS-Thermal Oil Gener 2017. https://www.sogecal.com/en/ork-konus-orbus-thermal-oil-generators/ (accessed January 1, 2017).

[42] TSI. OPS 3330. TSI Opt Part Sizer 3330 2017. http://tsi.com/optical-particle-sizer-3330/ (accessed January 1, 2017).

[43] Miceli P, Bensaid S, Russo N, Fino D. Effect of the morphological and surface properties of CeO2-based catalysts on the soot oxidation activity. Chem Eng J 2015;278:190–8. doi:10.1016/j.cej.2014.10.055.
[44] Axisuite®. Axitrap: Catalyzed Diesel Particulate Filter Simulation. Exothermia SA. 4.02.4. Thessaloniki, Greece: Exothermia SA; 2015.
[45] Pulkrabek WW, Ibele WE. The effect of temperature on the permeability a porous material. Int J Heat Mass Transf 1987;30:1103–9.
[46] Steffens J, Coury JR. Collection efficiency of fiber filters operating on the removal of nano-sized aerosol particles: I — Homogeneous fibers. Sep Purif Technol 2007;58:99–105. doi:10.1016/j.seppur.2007.07.011.
[47] Lee KW, Liu BYH. Theoretical Study of Aerosol Filtration by Fibrous Filters. Aerosol Sci Technol 1982;1:147–61. doi:10.1080/02786828208958584.
[48] Liu BYH, L. R. Efficiency, pressure drop and figure of merit of high efficiency fibrous and membrane filter media. Proc. Fifth World Filtr. Congr., Nice: 1990.
[49] Liu BYH, Rubow KL. Efficiency, pressure drop and figure of merit of high efficiency fibrous and membrane filter media. Proc. Fifth World Filtr. Congr., Nice: 1990.
[50] Schneider J, Weimer S, Drewnick F, Borrmann S, Helas G, Gwaze P, et al. Mass spectrometric analysis and aerodynamic properties of various types of combustion-related aerosol particles. Int J Mass Spectrom 2006;258:37–49. doi:10.1016/j.ijms.2006.07.008.
[51] Wentzel M, Gorzawski H, Naumann KH, Saathoff H, Weinbruch S. Transmission electron microscopical and aerosol dynamical characterization of soot aerosols. J Aerosol Sci 2003;34:1347–70. doi:10.1016/S0021-8502(03)00360-4.
[52] Exothermia SA 2017. www.exothermia.com (accessed January 1, 2017).
[53] Gysel M, Laborde M, Mensah AA, Corbin JC, Keller A, Kim J, et al. Technical note: The single particle soot photometer fails to reliably detect PALAS soot nanoparticles. Atmos Meas Tech 2012;5:3099–107.
[54] Orihuela MP, Gómez-Martín A, Miceli P, Becerra-Villanueva JA, Chacartegui R, Fino D. Experimental measurement of the filtration efficiency and pressure drop of wall-flow diesel particulate filters (DPF) made of biomorphic Silicon Carbide using laboratory generated particles. Appl Therm Eng 2018;131:41–53. doi:10.1016/j.applthermaleng. 2017.11.149.
[55] Stratakis GA, Psarianos DL, Stamatelos AM. Experimental investigation of the pressure drop in porous ceramic diesel particulate filters. Proc Inst Mech Eng Part D-Journal Automob Eng 2002;216:773–84.
[56] Ma Y, Zhu M, Zhang D. Effect of a homogeneous combustion catalyst on the characteristics of diesel soot emitted from a compression ignition engine. Appl Energy 2014;113:751–7. doi:10.1016/j.apenergy.2013.08.028.
[57] Lapuerta M, Martos FJ, Herreros JM. Effect of engine operating conditions on the size of primary particles composing diesel soot agglomerates. Aerosol Sci 2007;38:455–66. doi:10.1016/j.jaerosci.2007.02.001.
[58] Haralampous O, Payne S. Experimental testing and mathematical modelling of diesel particle collection in flow-through monoliths. Int J Engine Res 2016;17:1045–61.

Chapter 4
Microstructural and physical characterization of biomorphic Silicon Carbide

Chapter 3 dealt with Materials and Methods. It covered the theory and experimental bases applied in the different experimental tests and numerical simulations performed in this thesis. The first part of the chapter was dedicated to relating and describing all the experimental techniques used to characterize the small lab-scale samples. While in the second part, the manufacturing of the DPF prototypes, the experimental measurement of their filtration performance, and the additional numerical study, were addressed. Both parts can be considered relatively independent, and both yield a great deal of data and results.

Chapter 4 presents the main results of the characterization study, including all the representative data obtained through each technique. All results presented in this chapter correspond to the disk-shaped lab-scale samples that were manufactured during the first part of the research. In some tests (density, permeability, thermal conductivity), samples were tested entire; although in other tests (porosity, mechanical strength) they had to be cut into smaller pieces.

As shown in Chapter 3 (Section 3.2), up to five precursors were chosen for this research study and, in the case of natural ones, two possible cutting directions were considered: axial and radial. The characterization techniques were applied over the nine resulting typologies of bioSiC. For the sake of clarity, many figures of this chapter will be presented in two parts: the left side for the axial samples, and the right one for the radial ones. Besides, when necessary, the same nomenclature than in Chapter 3 will be used to identify with short acronyms the samples through their precursor and their cutting direction (see Table 3.1 in Chapter 3).

This chapter is divided into four sections following with the same structure of Section 3.3 in Chapter 3. The first section (Section 4.1) presents the results of the microstructural characterization, while the second one (Section 4.2) presents the thermal and mechanical behaviour. The third section (Section 4.3) presents the results of crystallography, thermo-gravimetry and differential scanning calorimetry; that is, those techniques aimed at identifying possible compositional deviations derived from the manufacturing process. And finally, Section 4.4 will present the results of the permeability and filtration tests. The results presented in this chapter are directly linked to the analyses presented in Chapter 5, where practical relationships

between functional and microstructural parameters are presented. Later, Chapter 6 will deal exclusively with the results of the experimental campaign with the prototypes, and with the results of the numerical study

Related publications

1. A. Gómez-Martín, M.P. Orihuela, J.A. Becerra-Villanueva, J. Martínez-Fernández, J. Ramírez-Rico. *Permeability and mechanical integrity of porous biomorphic SiC ceramics for application as hot-gas filters*. Materials & Design, Vol. 107, 450–460, 2016. doi: 10.1016/j.matdes.2016.06.060
2. A. Gómez-Martín, M.P. Orihuela, J. Ramírez-Rico, R. Chacartegui, J. Martínez-Fernández. *Thermal conductivity of porous biomorphic SiC derived from wood precursors*. Ceramics International, Vol. 42, Iss. 14, 16220–16229, 2016. doi: 10.1016/j.ceramint.2016.07.151
3. M.P. Orihuela, A. Gómez-Martín, J.A. Becerra-Villanueva, R. Chacartegui, J. Ramírez-Rico. *Performance of biomorphic Silicon carbide as particulate filter in diesel boilers*. Journal of Environmental Management, Vol. 203, Iss. 3, 907-919, 2017. doi: 10.1016/j.jenvman.2017.05.003

4.1. Microstructural characterization

In this section the different bioSiC specimens are characterized in terms of microstructural arrangement, density, porosity and pore size distribution. In the following figures, micrographs of carbon preforms obtained by pyrolysis (prior to infiltration) are shown. Figure 4.1 shows two images, with two different magnification levels, of the carbon preform obtained from Medium Density Fibreboard (MDF) for a section perpendicular to the direction of compacting fibres (radial).

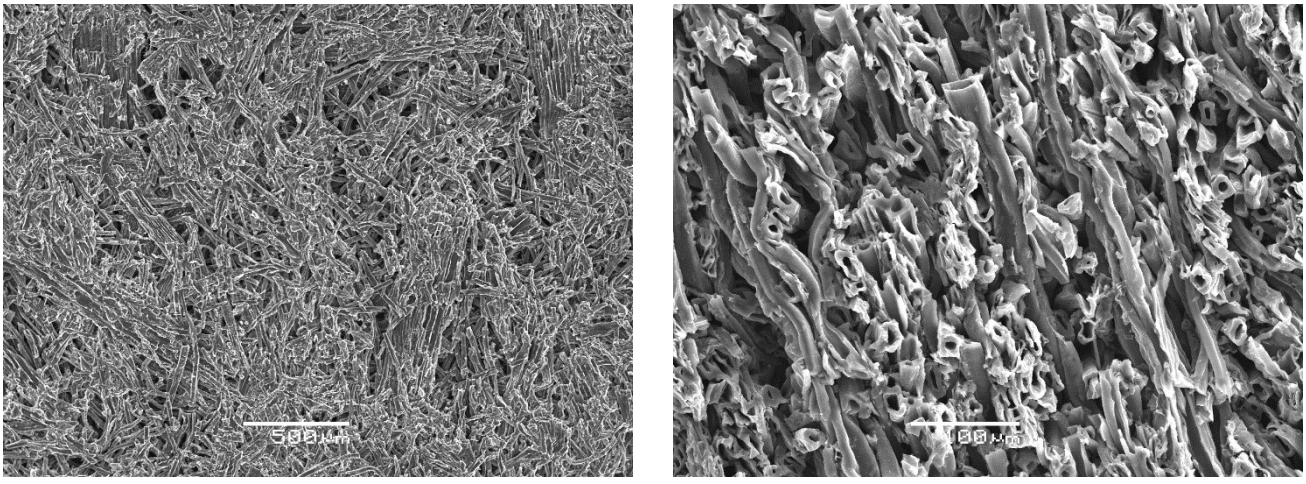

Figure 4.1. SEM images of the carbon matrix obtained from the pyrolysis of MDF

Figure 4.2 shows SEM images of the carbon matrixes obtained from the natural precursors, for sections perpendicular to the growth direction (axial).

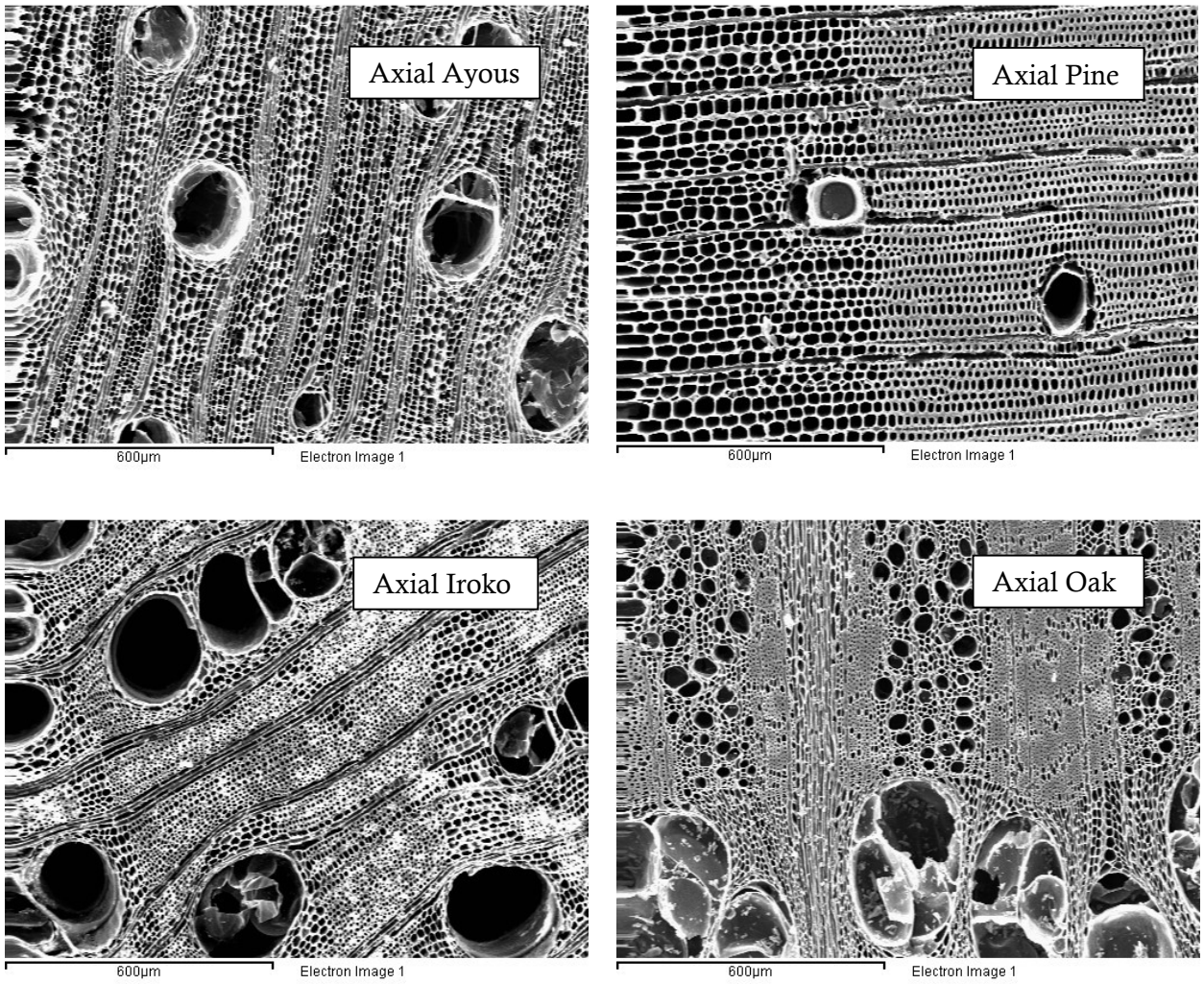

Figure 4.2. SEM images of the carbon matrixes obtained from the pyrolysis of natural woods

Carbon preforms of all types of natural wood studied (Figure 4.2) show high porosities which reproduce the structure of the original wood with channels aligned with the tree growth direction [1]. Small pores are generally located where the wood density is higher and the carbon wall is thicker; this happens usually in the growth rings of the tree. On the other hand, the microstructure of the carbon preforms made from processed fibreboards (Figure 4.1) consists of an agglomeration of cellulose fibres. It shows a large amount of short pores delimited by the fibres and interconnected according to the particular accommodation that the fibres experience during the compaction process. Above all, is remarkable that the microstructure of this carbon preforms made from artificial wood is more homogeneous than that of natural wood precursors, which sometimes presents local variations due to the presence of growth rings.

The microstructure of the resulting porous SiC specimens obtained after the reactive infiltration with molten silicon and the evaporation treatment to remove the excess of silicon from the pores, are shown in the following figures.

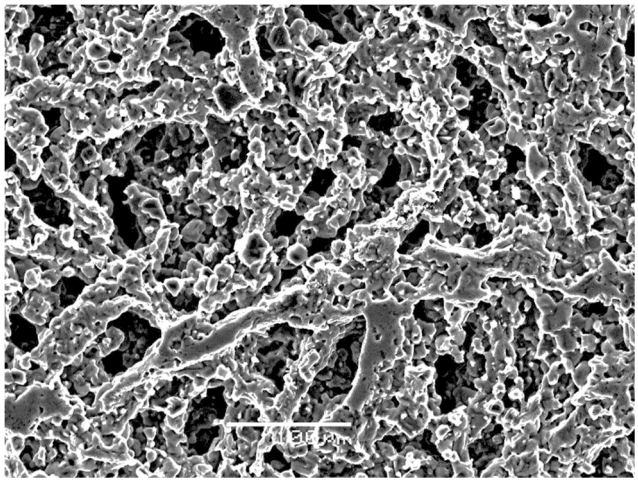

Figure 4.3. SEM image of the MDF-bioSiC specimen

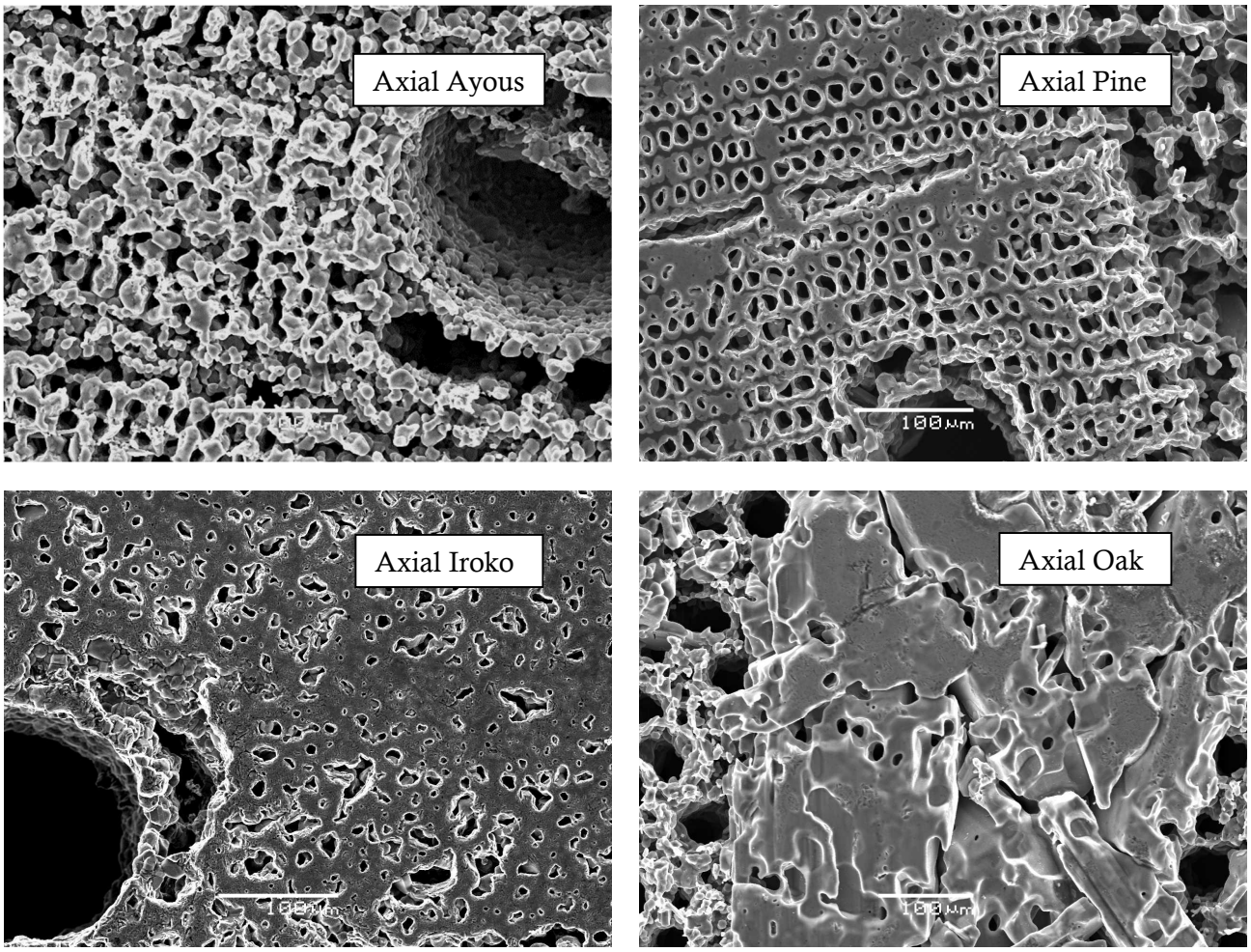

Figure 4.4. SEM images of the bioSiC specimens (axial samples)

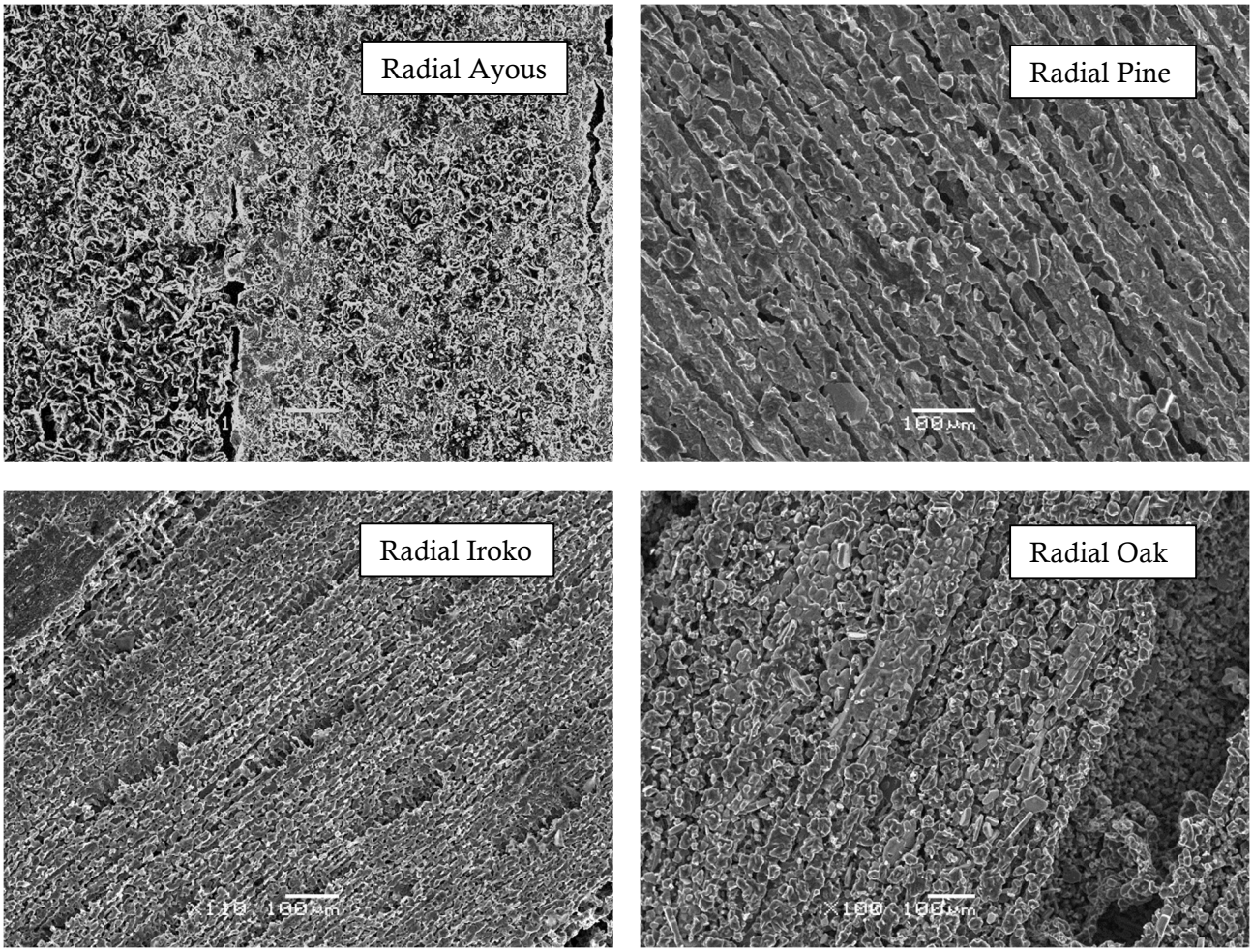

Figure 4.5. SEM images of the bioSiC specimens (radial samples)

Figure 4.3 shows a micrograph of the bioSiC specimen made from MDF. Figure 4.4 and Figure 4.5 show micrographs of the other bioSiC specimens made from natural precursors. Figure 4.4 presents the axial samples, while Figure 4.5 presents the radial ones. SEM images in Figures 4.3 to 4.5 show that most of the remaining silicon has been removed, at least in the large pores, resulting in a continuous SiC scaffold with elongated channels and highly interconnected porosity that resembles the morphology of the original wood precursor. Some of the smallest pores still present some residual silicon. The resulting material is clearly anisotropic, just like the original wood material, but still with long interconnected channels. The connection between the channels can be observed more clearly in the micrographs of the radial samples (Figure 4.5), where they are mainly arranged in the visible cutting plane (upper surface) of the samples.

In the case of bioSiC specimens made from MDF, the micrographs were taken in a section perpendicular to the direction of fibre compaction. Also in this case, the microstructure presents an anisotropic character [2] determined by the manufacturing and compaction process. Due to their microstructure of oriented fibres and their visual similarities with bioSiC specimens made from natural precursors, MDF-bioSiC samples (sections perpendicular to the direction of compacting fibres) were classified as "radial" samples. At the earliest stages of the research, the limited thickness of the fibreboards supposed a limitation for the fabrication of samples in a

different direction and, consequently, the functional characterization of the MDF-bioSiC was only made for one kind of samples. Later, with the development of the prototypes, the consideration of the alternative direction was, not only possible, but necessary.

4.1.1. Density based porosity

This section gathers the results of the direct weighing of the samples, the measurement of their density by pycnometry, and the calculated porosity from the relationship between bulk and real density. The density-based porosity can be calculated as follows:

$$\varepsilon = \frac{\rho_{pyc} - \rho_{bulk}}{\rho_{pyc}} \cdot 100 \qquad \text{Eq. 4.1}$$

in case of using the measured density of the pycnometer ρ_{pyc}. Or:

$$\varepsilon = \frac{\rho_{th} - \rho_{bulk}}{\rho_{th}} \cdot 100 \qquad \text{Eq. 4.2}$$

in case of using the theoretical real density of Silicon Carbide ρ_{th}.

If there is no closed porosity, the density measured by pycnometry should be similar to the theoretical real density of silicon carbide (3.21 g/cm^3 for β-SiC [3]). In Table 4.1 the results of the measurements and the calculated density-based porosities are presented. In all cases, the difference between the two calculated porosities is smaller than 3%.

Table 4.1. Bulk density, real density and density-based porosity of the bioSiC samples

Sample		**Bulk density (g/cm^3)**	**Real density (g/cm^3)**	**Density-based porosity**	
				ρ_{pyc}-based (%)	ρ_{th}-based (%)
Ayous	Axial	0.87	3.37	74.2	73.0
	Radial	0.91	3.32	72.6	71.7
Pine	Axial	1.43	3.19	55.2	55.4
	Radial	1.35	3.27	58.7	57.8
Iroko	Axial	1.73	3.25	46.8	46.2
	Radial	1.57	3.28	52.1	51.2
Oak	Axial	1.87	3.26	42.6	41.8
	Radial	1.66	3.26	49.1	48.3
MDF	Radial	1.73	3.32	47.9	49.1

As can be appreciated, despite the blocking of the smallest pores due to the silicon infiltration, the resulting bioSiC specimens still preserve porosities over 40%, even in the least porous samples. Besides, with the chosen precursors, a wide range of densities and porosities is

obtained, which may be of great interest to effectively evaluate the influence of some microstructural parameters on the thermal and mechanical properties under study.

4.1.2. Porosity and pore size distribution

For further understanding of the porosity for each bioSiC sample, mercury intrusion porosimetry was used. Figure 4.6 shows the pore distribution curves, where the volume of pores is plotted as a function of the diameter.

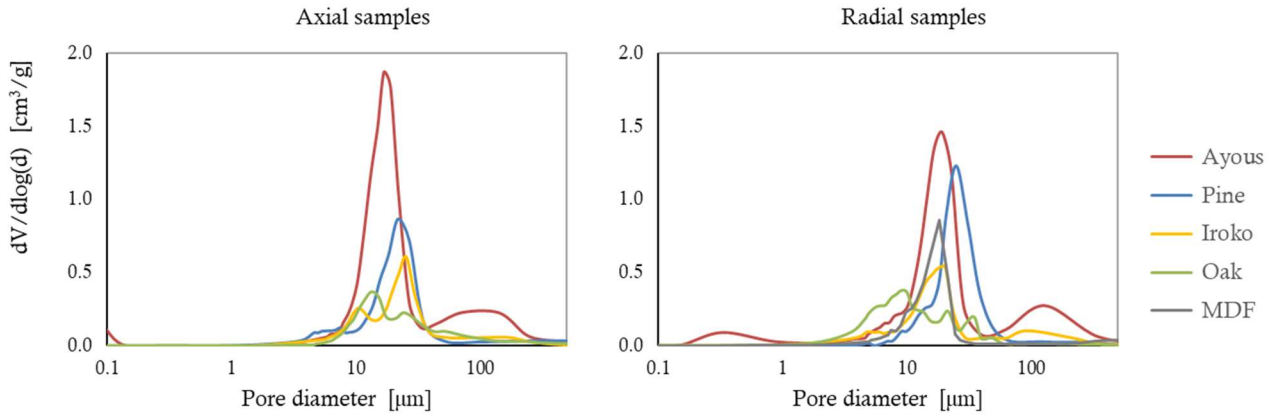

Figure 4.6. Pore size distributions of bioSiC specimens from different wood precursors

Commonly, pores with diameter lower than 30 µm are completely filled up with silicon after the infiltration process [4]. However, after removing the excess silicon by evaporation in the last stage of the manufacturing process, multi-modal pore volume distributions with pore sizes in a wide range are obtained. BioSiC specimens show multi-modal pore distributions, where the pores are irregularly distributed in a range from 0.1 to 400 µm depending on the wood precursor. The pore size range and peak pore size for each sample are detailed in Table 4.2.

Table 4.2. Porosities and pore size ranges of the bioSiC samples

Sample		Porosity (%)	Pore size range (µm)	Peak pore size (µm)
Ayous	Axial	70.8	0.1, 2-40, 40-300	~17, ~105
	Radial	68.9	0.1-2, 2-40, 40-440	~0.3, ~20, ~150
Pine	Axial	56.0	2-50	~21
	Radial	57.6	8-60	~25
Iroko	Axial	44.4	1-15, 15-40, 40-300	~10, ~25, ~150
	Radial	48.5	1-8, 9-35, 40-300	~5, ~18, ~120
Oak	Axial	43.7	5-20, 20-50, 50-350	~15, ~25, ~100
	Radial	45.1	2-15, 15-30, 30-100	~8, ~20, ~40
MDF	Radial	44.2	3-30	~18

Despite the slight differences between them, the results in the mercury intrusion porosimetry measurements of axial and radial samples have been presented separately in this work. The reason is that the processes of mechanizing and cutting prior to pyrolysis and infiltration may have not been applied in zones with similar porosity distributions, causing a deviation in the results depending on the sample and the cut section.

As shown in Table 4.2, pore size distributions of Ayous, Iroko and Oak-bioSiC samples present different pore size ranges where the sample has porosity. In this sense, it is noted that Pine and MDF-bioSiC showed narrower pore distributions than the other wood precursors.

The pore size distribution of Ayous-derived bioSiC shows three ranges of pore size: small pores with sizes ranging from 0.1 to 2 μm, pores with sizes ranging from 2 to 40 μm, and a third interval of very large pores with size between 40 and 440 μm. Pine-derived bioSiC shows a unimodal distribution with pores size depending on the growth ring of the tree but approximately 20-25 μm in size (Figure 4.6). Iroko-derived bioSiC presents a trimodal distribution with small pores ranging from 1 to 15 μm, medium pores ranging between 10 and 40 μm, and large pores ranging between 40 and 300 μm. Oak-bioSiC shows a trimodal distribution too, with small pores ranging from 2 to 20 μm, medium sized pores from 15 to 50 μm, and large pores from 30 to 350 μm. Finally, MDF-bioSiC shows a characteristic pore size of around 20 μm.

4.1.3. Specific surface

The specific surface was determined from the adsorption isotherm curves through the technique of physisorption. Due to the low specific surface of the samples, it was not possible to use N_2 as adsorbate gas; instead Kr was used at 77 K. The resulting adsorption isotherm curves are presented in Figure 4.7, where the adsorbed amount of gas (at standard temperature and pressure, STP) is plotted as a function of the ratio between the equilibrium pressure P and the saturation pressure P_0 for the different bioSiC samples.

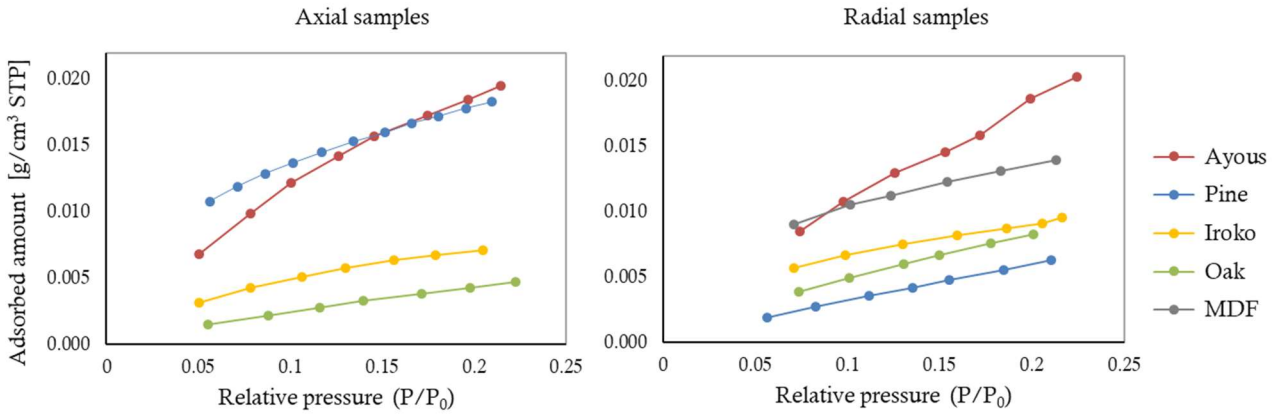

Figure 4.7. Adsorption isotherm curves of bioSiC specimens from different wood precursors

The specific surface is obtained from the adsorption curves by means of the BET model, which is based in the lineal dependence of the term $\frac{1}{w\left(\frac{P_0}{P}-1\right)}$ with the ratio of pressures $\left(\frac{P}{P_0}\right)$.

$$\frac{1}{w\left(\frac{P_0}{P}-1\right)} = \frac{c-1}{c\,w_m}\left(\frac{P}{P_0}\right) + \frac{1}{c\,w_m} \qquad \text{Eq. 4.3}$$

In this linear relationship, w is the adsorbed gas weight, w_m is the weight of adsorbate as monolayer, and c is the BET constant.

The value of the slope (A) and the y-intercept (Y) of the line are used to calculate the monolayer adsorbed gas quantity and the BET constant.

$$w_m = \frac{1}{A+Y} \qquad \text{Eq. 4.4}$$

$$c = 1 + \frac{A}{Y} \qquad \text{Eq. 4.5}$$

And once the monolayer adsorbed gas quantity w_m has been determined, the total surface area S_{tot} and the specific surface area S_{BET} are calculated as follows:

$$S_{tot} = \frac{w_m\,N\,s}{V} \qquad \text{Eq. 4.6}$$

$$S_{BET} = \frac{S_{tot}}{a} \qquad \text{Eq. 4.7}$$

Where N is Avogadro's number, s the adsorption cross section of the adsorbing species, V the molar volume of the adsorbate gas, and a the mass of the solid sample or adsorbent.

Table 4.3. Specific surface of the bioSiC samples

Sample	**Specific surface (m^2/g)**
Ayous	0.13
Pine	0.08
Iroko	0.04
Oak	0.05
MDF	0.07

In Table 4.3 the mean values of the specific surface are shown depending on the wood precursor but not on the cutting direction due to the negligible influence of this latter on the specific surface. In general, it can be observed that the resulting specific surface is low in all the cases. Compared to other advanced materials such as activated carbons, this specific surface is very

reduced, which might be in principle a negative influence in the abatement capacity of nanoparticles.

4.2. Thermal and mechanical characterization

The ceramic materials studied in this work are expected to be used as filtering materials at high temperature and, in particular, as substrate in DPFs. During the regeneration process, DPFs are exposed to sudden and severe temperature fluctuations, so there is a higher risk of crack formation and propagation. Failure in the material due to thermal shock can be prevented by increasing the thermal conductivity, by reducing the coefficient of thermal expansion, or by increasing its strength among others. In the following epigraphs, the results of the thermal and mechanical tests are presented. When possible, these properties have been measured at high temperature.

4.2.1. Thermal expansion coefficient

Along with thermal conductivity and mechanical strength, the thermal expansion coefficient is especially important due to its influence in the thermal shock resistance (TSR). Silicon Carbide is known to have higher thermal conductivity and tensile strength than Cordierite. However, its high coefficient of thermal expansion usually affects negatively its TSR [5,6]. In Figure 4.8, the thermal expansion coefficient is presented as a function of the temperature for the different bioSiC specimens made from each precursor. Temperature ranges from 200 to 1000 °C. The thermal expansion coefficient of monolithic β-SiC is also shown.

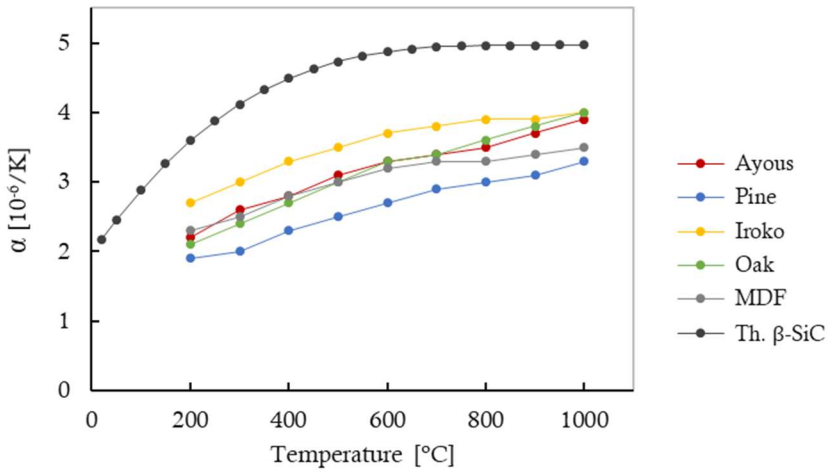

Figure 4.8. Thermal expansion coefficient of bioSiC specimens from different wood precursors

Due to small impurities of carbon in the final composition, or to the presence of residual silicon in the ceramic samples, the thermal expansion coefficient of bioSiC is in all cases lower than that of β-SiC. The smaller expansion that bioSiC experiences with a variation in temperature is

a positive effect in the final behaviour of the filter respect to a traditional SiC substrate, due to the reduction in the thermal stresses.

4.2.2. Thermal conductivity

The thermal conductivity of the different bioSiC samples has been characterized from ambient temperature to 700 ºC from experimental measurements of the thermal diffusivity and the calculation of the specific heat. It is calculated by means of the following expression:

$$k(T) = C_p(T)\,\alpha(T)\,\rho \qquad \text{Eq. 4.8}$$

where ρ is the bulk density of the samples, α the thermal diffusivity, and C_p the specific heat.

The density of the samples was measured at the beginning of the characterization study by direct dimensioning and weighting (see Table 4.1).

The thermal diffusivity of each sample was experimentally measured by using the Laser Flash method (see Section 3.3.2). Figure 4.9 shows the results of the measurements, from ambient temperature to 980 ºC, with the axial samples at the left hand side, and the radial ones at the right hand side.

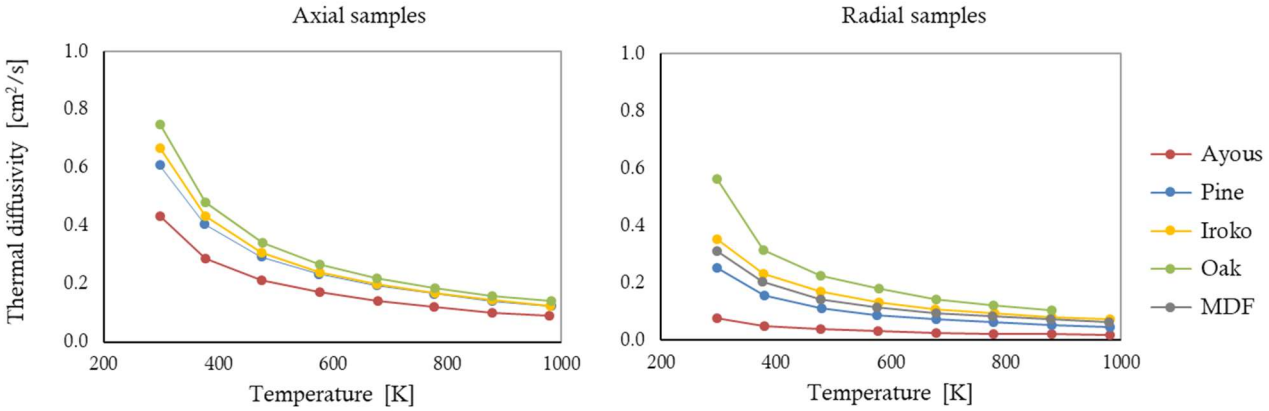

Figure 4.9. Thermal diffusivity of bioSiC specimens from different wood precursors

By multiplying bulk density, diffusivity and specific heat, the thermal conductivity is obtained. Figure 4.10 shows the resulting values of conductivity for the bioSiC samples. For comparative purposes, in the same graphs, the thermal conductivity of dense small-grained polycrystalline SiC ceramics [3] has been also represented.

As shown in Figures 4.9 and 4.10, at room temperature thermal diffusivities and thermal conductivities of the bioSiC samples were in the range of approximately 0.07–0.75 $cm^2 \cdot s^{-1}$ and 4–88 $W \cdot m^{-1}K^{-1}$ respectively, and significantly decreased with increasing temperature showing a decrease of about ~57–67% over the range of temperature measured.

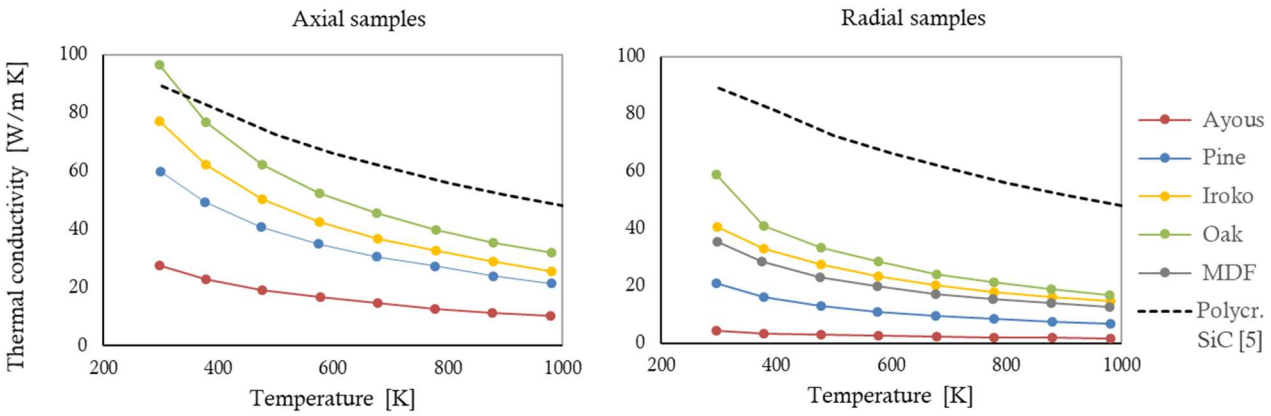

Figure 4.10. Thermal conductivity of bioSiC specimens from different wood precursors

The calculated numerical values of thermal conductivity can be seen in Table 4.4. As will be explained later in Chapter 5, due to the characteristic porosity of the biomorphic samples, their bulk thermal conductivity is always lower than that of dense SiC.

Table 4.4. Thermal conductivity of the bioSiC samples

Sample		Thermal conductivity ($W \cdot m^{-1}K^{-1}$)	
		Ambient temperature	**700 ºC**
Ayous	Axial	26	10
	Radial	4	2
Pine	Axial	55	20
	Radial	23	7
Iroko	Axial	74	24
	Radial	39	14
Oak	Axial	88	29
	Radial	60	19
MDF	Radial	34	12

The specific heat capacity of SiC increases with an increase in temperature (Eq. 3.5), thus the decrease in diffusivity values with temperature is more remarkable. The differences between the values for bioSiC obtained from different wood precursors with the temperature were higher at low temperatures.

4.2.3. Compressive strength

To study the mechanical strength, compression tests were carried out at constant strain rate at ambient temperature. The compressive load was applied considering the two possible cutting directions: axial and radial. Mechanical properties vary depending on the starting wood: hard woods, with higher densities, present better mechanical performances than soft ones [7]. But,

along with density and porosity values, also the microstructure (pores and defects) plays a relevant role because the presence of porosity acts in detriment of the mechanical strength.

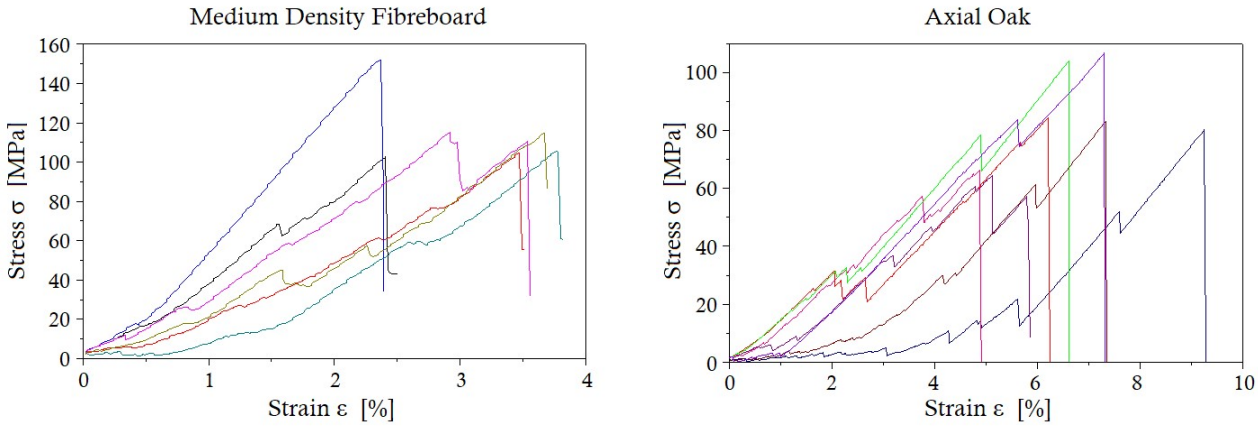

Figure 4.11. Stress-strain curves from compressive-strength tests of two bioSiC specimens: MDF and Axial Oak

Figure 4.11 shows some examples of stress-strain curves generated from uniaxial compressive-strength tests. As can be seen, the stress-strain curves present the typical saw-tooth shape characteristic of macroporous ceramic materials. Porous biomorphic ceramics break down before any plastic deformation happens in response to any load. The fracture of the samples is in all cases catastrophic and brittle.

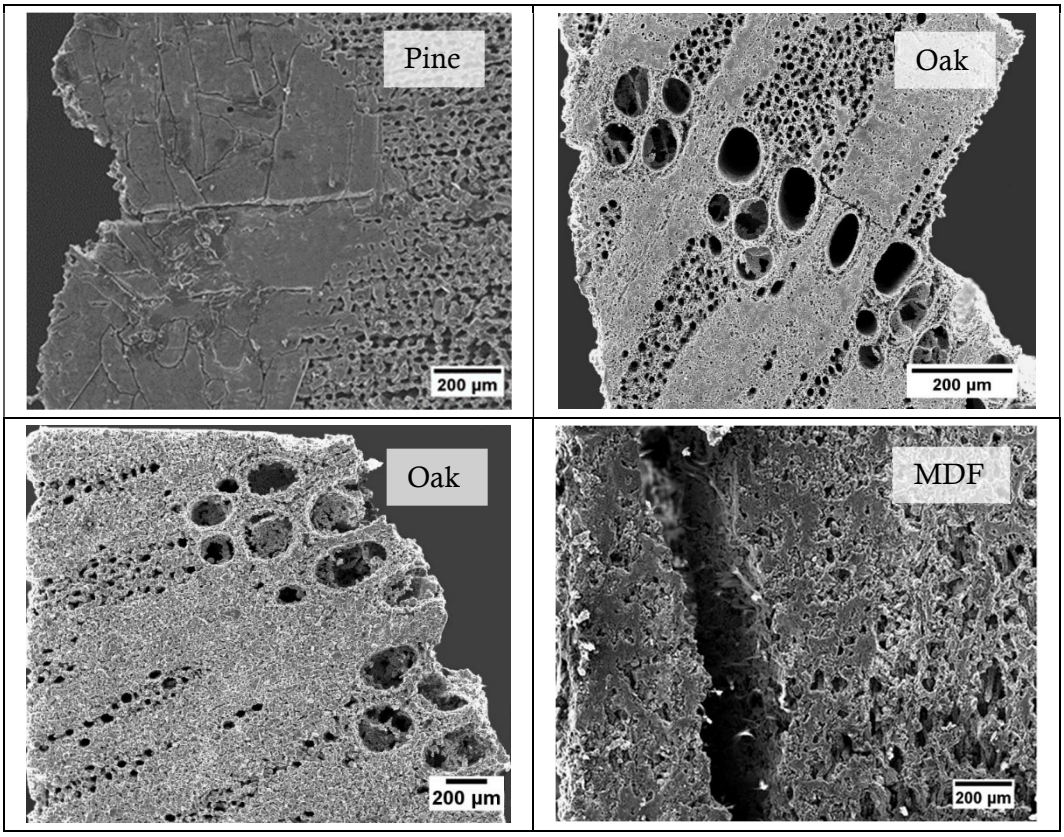

Figure 4.12. Compressive fractography of bioSiC specimens from different wood precursors

This process of brittle fracture involves the formation and propagation of cracks, favoured in this case by the pores present in the bioSiC samples. Figure 4.12 shows the compressive fractography of the samples, where evidence of a preferential fracture line can be observed. The presence of small defects in the material, as pores are in this case, act as stress concentrators, that is, places where the stress magnitude is amplified. The level of amplification of the stress depends on the size of the pore, being higher for long and sharp defects.

The average of the maximum strength was determined from a minimum of five measurements for each precursor. The results are presented in Table 4.5.

Table 4.5. Maximum compressive strength of the bioSiC samples

Sample		**Maximum compressive strength (MPa)**	$\frac{\sigma_{max}^{axial}}{\sigma_{max}^{radial}}$
Ayous	Axial	8	2.7
	Radial	3	
Pine	Axial	25	2.1
	Radial	12	
Iroko	Axial	22	1.4
	Radial	16	
Oak	Axial	84	3.2
	Radial	26	
MDF	Radial	115	

The anisotropic character of bioSiC clearly affects its compressive strength. Maximum compressive strength is proved higher when the load is applied parallel to the growth direction (axial) ranging from 8 to 88 MPa, resulting in a greater mechanical stability. In contrast, when measurements were made in the radial orientation, maximum compressive strengths were 1.4–3.2 times lower, ranging from 2 to 10 MPa in bioSiC derived from natural wood. Although samples from MDF-wood were considered radial samples due to their microstructure, their compressive strength differ greatly from natural wood-derived bioSiC because of the difference in microstructure and because of a more homogeneous pore size distribution.

The compressive strengths of bioSiC specimens measured in this work were slightly lower or comparable to other values reported in the literature in relation to their densities [7,8]. Lower values could be due to two factors. BioSiC specimens could contain a small proportion of unreacted carbon after molten silicon infiltration, which has been demonstrated to weaken mechanical properties [9]. Additional differences could be due to the use of capillary extraction and evaporation instead of chemical etching used in other works [8].

Apart from the effect of the anisotropy, Table 4.5 suggests that there might be a relationship between mechanical strength and density of the samples. In Chapter 5, a further analysis is made on this effect.

4.3. Phase and TGA-DSC analysis

Some of the experimental facts observed during the characterization study suggest that slight deviations from the sought composition could be actually happening. The low specific surface of the samples, or their low thermal expansion coefficient compared to that of pure β-SiC, may be indications of the presence of impurities or phase changes within the material.

As explained in Section 3.3.3, the presence of some inaccessible pores in the initial carbon matrix, or the insufficient time for reaction in some points, may leave some unreacted carbon in the infiltrated piece. Besides, the high temperatures in the specimens during the Si-evaporation process, may induce a phase change from β-SiC to α-SiC. The following analyses have allowed to identify and quantify these deviations.

4.3.1. X-ray diffraction

Figure 4.13 shows the X-Ray diffractograms of an MDF-based bioSiC specimen before and after removing the non-reacted silicon by evaporation.

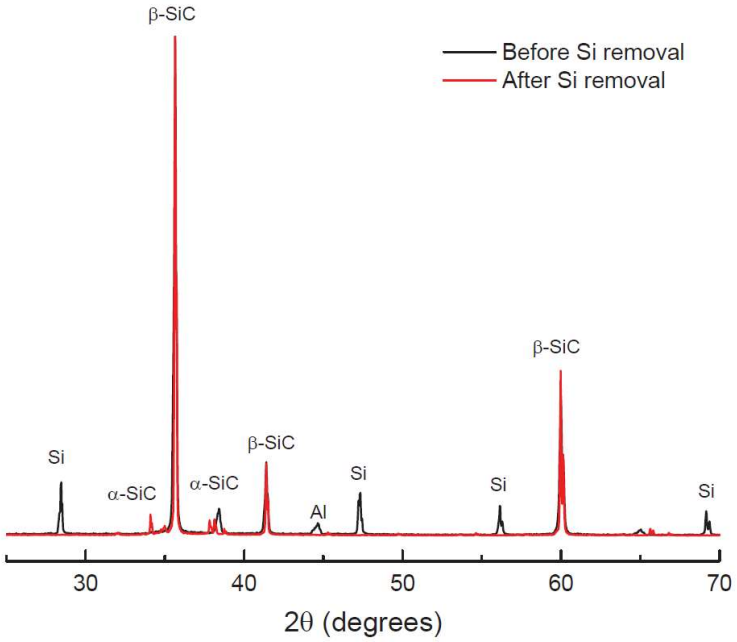

Figure 4.13. X-ray diffraction patterns of an MDF-bioSiC specimen before and after residual Si removal by capillary extraction at high temperature

The initial diffraction pattern, the one obtained before the silicon removal, presents three diffraction peaks at 2θ = 35.6°, 41.3°, 60.0° corresponding to the (111), (200), (220) planes in β–SiC (cubic) respectively and four diffraction peaks corresponding to free silicon (FCC) were found. At this stage of the manufacturing process, the material was essentially a β-SiC/Si crystalline composite with a main phase of SiC and a secondary phase of Si. After removing the silicon by evaporation, the free Si peaks are absent and small peaks attributed to α-SiC are found around the main (111) β-SiC reflection. It can be inferred that the highly localized exothermic reaction between gaseous Si and free carbon lead to the transformation of β-SiC to α-SiC taking place at 1800 °C [10,11]. A small Al peak can also be observed, which can be attributed to surface contamination during processing.

4.3.2. TGA (Thermogravimetry) + DSC (Differential Scanning Calorimetry) analysis

In order to evaluate the amount of residual carbon present in the samples after the infiltration process, they were pulverized and studied through thermogravimetry and DSC (Differential Scanning Calorimetry). Samples were heated up to 1000 ºC with a heating ramp of 20 ºC/min in a 100 ml/min air stream. In this process, the residual carbon reacts with the oxygen producing carbon dioxide, which volatilizes and leaves in the crucible only the SiC fraction.

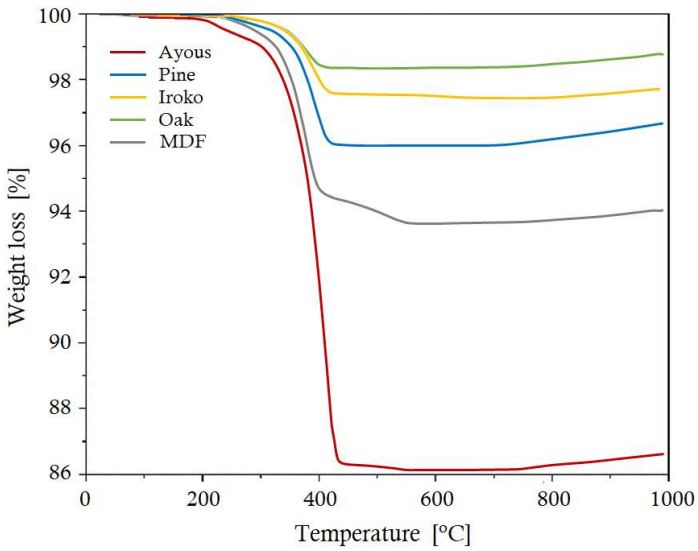

Figure 4.14. TGA analysis of bioSiC specimens from different wood precursors

Figure 4.14 represents the weight loss of the bioSiC samples with the increase in temperature. In this case samples were milled to powder, and no difference was studied between axial and radial specimens. At around 400 ºC, all the residual carbon reacts with the air producing carbon dioxide and abandoning the crucible in gaseous state. In the crucible only remains the ceramic fraction of the sample; the fraction of material successfully converted to SiC during the infiltration process.

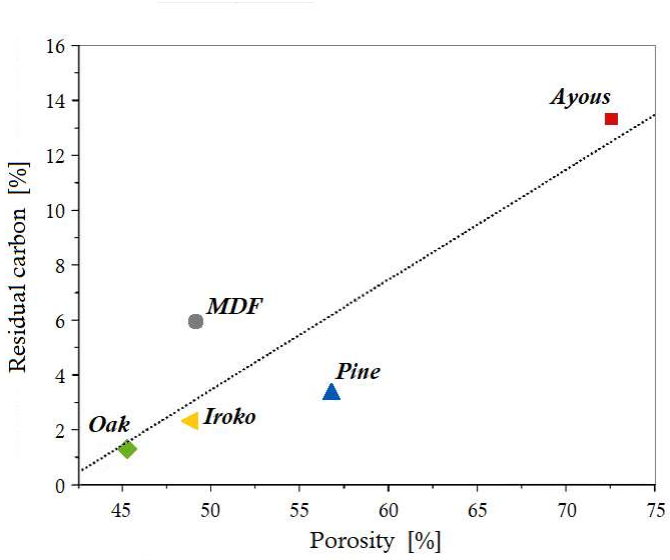

Figure 4.15. Percentage of residual carbon in the samples after the infiltration process versus porosity

In Figure 4.15, the percentage of residual carbon of each specimen has been represented versus the porosity. This figure suggests a relationship between both variables, and shows that the higher the porosity of the samples, the higher the amount of residual carbon. Previous studies have shown that the degree of molten silicon infiltration has a strong effects on the final density of the sample and, consequently, on the mechanical properties of the porous biomorphic material [12]. This fact was overlooked at the beginning of this study. In this study, all the samples were made with the same proportion of silicon. As a result, the most porous samples, especially the ones made from Ayous wood, resulted mechanically weaker.

4.4. Permeability and intrinsic filtration efficiency

Up to now, bioSiC specimens made from a number of different wood precursors have been studied through a number of general techniques, the results of which are useful to understand and predict their behaviour in any application. In order to get a more precise idea of how suitable these bioSiC specimens are for their application as DPF, two specific test campaigns have been carried out: one to determine their permeability, which is closely related to the pressure drop; and another one to determine their filtration efficiency.

In both cases, the measurements presented in this section correspond to the small disk-shaped lab-samples made for the characterization study. This implies that the resulting values of permeability and filtration efficiency won't be the final exact permeability and filtration efficiency of a full shape wall-flow filter. However, these preliminary measurements allowed to stablish a comparison between the different specimens and to make decisions about which precursor might be more suitable to manufacture the prototype.

Besides, the results here presented correspond mainly to the initial stage of a filtration process, that is the starting point in which the substrate is completely clean and free from deposited particles. In the case of permeability measurements this is clear, since the tests were made with only clean air over the clean samples. As explained in Chapter 2, the particles captured by the filter remain within the pores of the substrate generating an additional resistance to the passage of gas flux and particles, until the filter is regenerated and all the particles are removed by any technique. This means that the accumulation of particles in the filter decreases its permeability and increases its filtrations efficiency.

In this work, to make the preliminary study on the filtration efficiency, a diesel boiler was used. The working fluid was the soot laden exhaust gas stream coming from the boiler, and an approximation to the transient behaviour of the filter with the soot load could be obtained. Nevertheless, since the diesel boiler didn't operate continuously, but through intermittent start-stop cycles, the results cannot be directly extrapolated to the performance with a continuous soot load that takes place in an automotive application.

4.4.1. Permeability

The determination of the permeability of the bioSiC specimens was done controlling the pressure and the flow rate across the samples, as described in the experimental procedure in Section 3.3.4. In order to ensure repeatability, three samples of each precursor and orientation (axial and radial) were tested. The averaged experimental pressure drops per unit of length as a function of air-flow velocities for each bioSiC sample is plotted in Figure 4.16 along with the fit to Forchheimer's equation (Eq. 3.7).

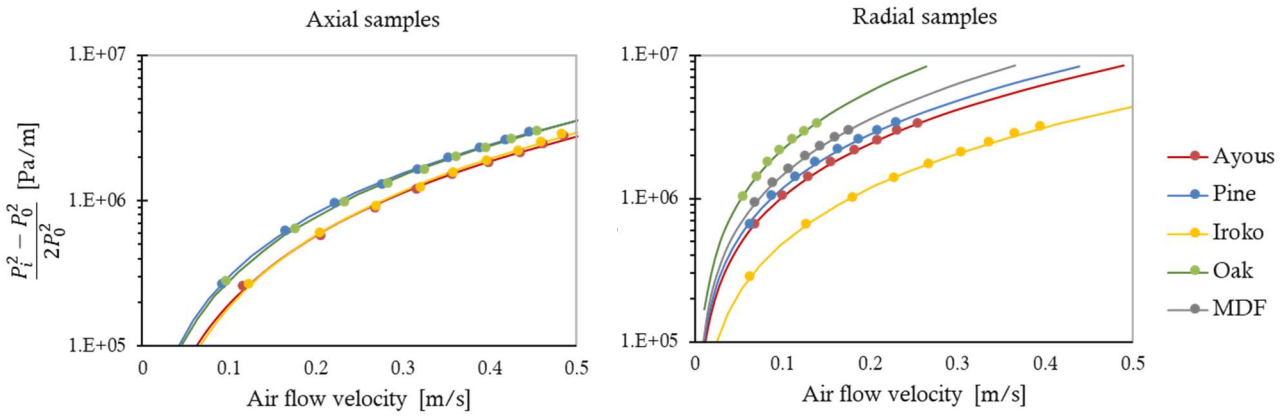

Figure 4.16. Pressure drop per unit of length as a function of air-flow velocity of bioSiC specimens from different wood precursors

It can be noted that the pressure drop increases with the gas-flow velocity. The experimental data generally showed a good fit to the quadratic dependence with air-flow velocity, with least-squares coefficients $r^2 > 0.998$. Darcian and inertial permeability parameters k_1 and k_2, respectively [13], were calculated from these fits and are shown in Table 4.6.

Table 4.6. Permeability constants of the bioSiC samples

Sample		**Darcian permeability k_1 (10^{-12} m^2)**	**Inertial permeability k_2 (10^{-8} m)**
Ayous	Axial	36.0	13.0
	Radial	2.2	6.7
Pine	Axial	9.4	11.4
	Radial	1.8	5.7
Iroko	Axial	46.0	11.6
	Radial	5.4	10.0
Oak	Axial	12.0	11.2
	Radial	1.1	2.2
MDF	Radial	1.0	2.1

For all bioSiC samples in the axial direction, except for Pine-bioSiC, k_1 was at the same order of magnitude (10^{-11} m^2) in contrast to radial samples for which all values were around 10^{-12} m^2, an order of magnitude lower. k_2 for all axial samples was in the range of 10^{-7} m, and 10^{-8} m in the case of radial samples. A more detailed analysis is made in the following chapter regarding these values and the resulting applicability of bioSiC as filter material.

4.4.2. Intrinsic filtration efficiency

As explained in Section 3.3.4, an experimental study of the intrinsic filtration efficiency of the different bioSiC specimens was done using for the tests the exhaust gases of a diesel boiler. A fraction of the particle laden exhaust gases from the boiler was forced to pass through the lab-scale specimens, so that they acted as a filter. The efficiency of a particle filter can be evaluated as follows:

$$\eta_N = \frac{N_u - N_d}{N_u} \qquad \text{Eq. 4.9}$$

where N_u is the number of particles per unit volume upstream the filter (Eq. 4.10), and N_d is the number of particles per unit volume downstream the filter (Eq. 4.11).

$$N_u = N_b = \frac{n_b}{V_b} \qquad \text{Eq. 4.10}$$

$$N_d = \frac{n_d}{V_d} \qquad \text{Eq. 4.11}$$

In this case, the particle counter was not able to measure simultaneously in two points, so first the particle production of the boiler was measured using the empty sample carrier to evaluate the equivalent $N_u = N_b$.

Due to its temperature control system (ON/OFF control), the boiler operates on a cyclic basis. It works at full load while the temperature is below the set point, and then turns off until oil temperature decreases 10 ºC below the set point. Each cycle lasts around 20 min, during which the recorded number of particles follows a bell-shaped distribution (Figure 4.17). The OPS allows for the selection of different sampling and logging times. Since the efficiency of a particle filter is not constant but it increases as the porous media loads with particles [14], the minimal logging time, 1 s, was set. This choice not only allowed us to study the transient behaviour of the filtration efficiency with the soot load, but also eased the calculation procedures with time based variables. Furthermore, the sampling time was set to 1 h 40 min, that is, 5 full operation cycles of the boiler. According to the levels of particle production in the boiler, this sampling time is high enough for the soot cake formation, and for the samples to reach their maximum efficiency. Once the production of particles in the boiler and its time distribution in a 100-min-period was determined, tests placing the different samples under the same operation profiles were performed.

The flow rate was set to 1 LPM by the internal pump of the OPS ($V_d = V_b$) and it was constant, so the efficiency could be measured only in terms of the number of particles, as can be seen in Eq. 4.12:

$$\eta_N = \frac{n_b - n_d}{n_u} \qquad \text{Eq. 4.12}$$

In order to study the dependence of the filtration efficiency on the particle size, 14 channels have been arranged in the OPS. Most of the particles produced by the boiler were smaller than 600 nm, and the minimum particle size detected by the OPS was 300 nm, so the channels were arranged logarithmically between 300 and 600 nm as shown in Table 4.7.

Table 4.7. Particle size arrangement in the OPS channels: diameter range, logarithmic mean diameter, and effective density samples

	Channel						
	1	**2**	**3**	**4**	**5**	**6**	**7**
Lower diameter (nm)	300	317	335	354	374	395	417
Upper diameter (nm)	317	335	354	374	395	417	440
Lmd (nm)	308	326	344	364	384	406	428
Effective density (g/cm^3)	0.223	0.214	0.206	0.198	0.191	0.184	0.177

	Channel						
	8	**9**	**10**	**11**	**12**	**13**	**14**
Lower diameter (nm)	440	465	491	519	548	579	612
Upper diameter (nm)	465	491	519	548	579	612	10000
Lmd (nm)	452	478	505	533	563	595	2474
Effective density (g/cm^3)	0.17	0.164	0.158	0.152	0.146	0.14	0.052

For each of these channels, collection efficiency might be calculated with the same formula (Eq. 4.12) but applied only to that particle sizes range (j).

$$\eta_{Nj} = \frac{n_{uj} - n_{dj}}{n_{uj}} \qquad \text{Eq. 4.13}$$

The transient evolution of the filtration efficiency during the tests was studied as a function of two different parameters: time and soot load. The first is direct since measurements were made on a time basis, but the second allows comparing different precursors performance. In both cases, curves were smoothed by averaging the efficiency every 120 s.

The instantaneous soot load was calculated by adding up the mass of all the particles retained within the filter up to that instant. In general, if a particle is spherical, its mass can be calculated from its volume and its density. However, due to their fractal like morphology, soot particles are usually characterized by their effective density [15], defined as particle mass divided by its mobility equivalent volume, that is, the volume of a sphere with the same mobility than the particle in an electric field [16]:

$$\rho_e = \frac{m}{V_m} \qquad \text{Eq. 4.14}$$

From Eq. 4.14, the mass of the particles can be calculated as:

$$m = \rho_e V_m = \frac{\rho_e \pi {d_m}^3}{6} \qquad \text{Eq. 4.15}$$

Besides not knowing the effective density ρ_e, this expression assumes the diameter of a particle is equal to its electrical mobility diameter d_m [17]. The optical sizing method that the OPS uses reports an optical particle diameter which is often different from the electrical mobility diameter [18].

Some authors choose to combine the OPS data with the data from another kind of sizer (SMPS or DMA) and merge when necessary the resulting curves to one single function [18,19]. In this work, in order to observe the trends and compare different precursors, the optical diameter has been used as the mobility diameter. For each channel of the OPS, the logarithmic mean diameter (Lmd) was calculated from the lower diameter (Ld) and the upper diameter (Ud) using Eq. 4.16. Results can be seen in Table 4.7.

$$\log Lmd = \frac{\log Ld + \log Ud}{2} \qquad \text{Eq. 4.16}$$

On the other hand, with respect to the effective density, we have used the correlation found by Maricq for fractal-like diesel soot particles [20], which is based on several DMA measurements on diesel engines at various vehicle speeds:

$$\rho_e = \rho_0 \left(\frac{d_m}{d_0}\right)^{(D_f-3)} \qquad \text{Eq. 4.17}$$

Here d_0 and ρ_0 are the primary particle diameter and density, and D_f is the fractal dimension. Acceptable values for d_0 and ρ_0 are respectively 60 nm and 0.7 g/cm^3 [20]; and the fractal dimension of diesel vehicle soot is $D_f = 2.3$ [21]. Assuming these values, the calculated effective densities for the particle size ranges of this work (Table 4.7) are very similar to those measured by Maricq [20] and Wierzbicka [22]. This effective density is known to decrease with increasing particle size owing to the rising fraction of voids caused by aggregation [21].

A quick glance at the first results reveals that the cutting direction of the wood is a critical factor in the performance of bioSiC. Radial samples show a much better performance than axial ones in terms of efficiency and capacity of retaining particles. In order to better distinguish trends and orders of magnitude, figures will be presented in two parts as in previous sections: the left side for axial samples, and the right one for the radial samples.

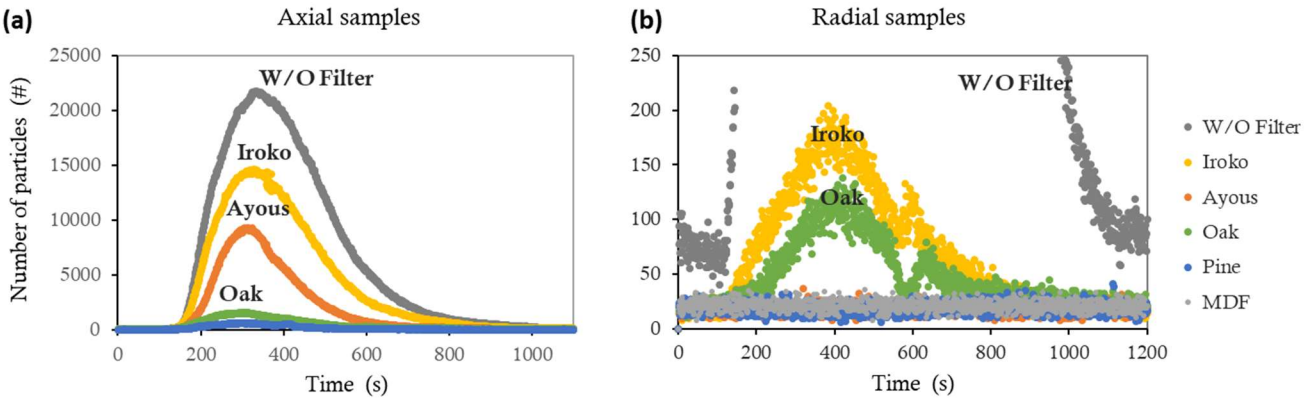

Figure 4.17. Number of particles measured downstream the filter samples during boiler's first cycle. (a) Axial samples (b) Radial samples

In Figure 4.17 the number of particles measured downstream the filter samples during the first cycle is presented for axial and radial samples with the filters fabricated from Iroko, Ayous, Oak, Pine and MDF and compared with the distribution by the boiler without filter (W/O Filter). The grey curve corresponding to the situation without filter (W/O Filter) is included in both graphs (a) and (b), to serve as a reference for the rest of the curves corresponding to the situation with the different filters.

As can be seen in Figure 4.17, the amount of particles that achieves to cross a radial filter in each moment is about two orders of magnitude smaller than the one that crosses an axial filter (15000 particles vs. 200 for Iroko sample) due to the pores size and distribution. The y-axis in Figure 4.17b was zoomed in accordingly to this reduction of the number of particles despite the scale of the grey "W/O Filter" curve. MDF has also a good performance, similar to that of the radial samples, which was to be expected due its microstructure of oriented fibres perpendicular to the compacting direction.

Even in the case of axial samples, where we find a low initial performance, an increase in the efficiency can be noticed as the test continues and the filter start accumulating particles. Except axial Iroko, all other samples reduce below 1% the amount of non-captured particles after five cycles of operation of the boiler (Figure 4.18). This behaviour has been extensively studied and demonstrated to be consequence of the accumulation of particles within the filtering media (depth filtration) and the later formation of a soot cake in its surface (soot-cake filtration) [14].

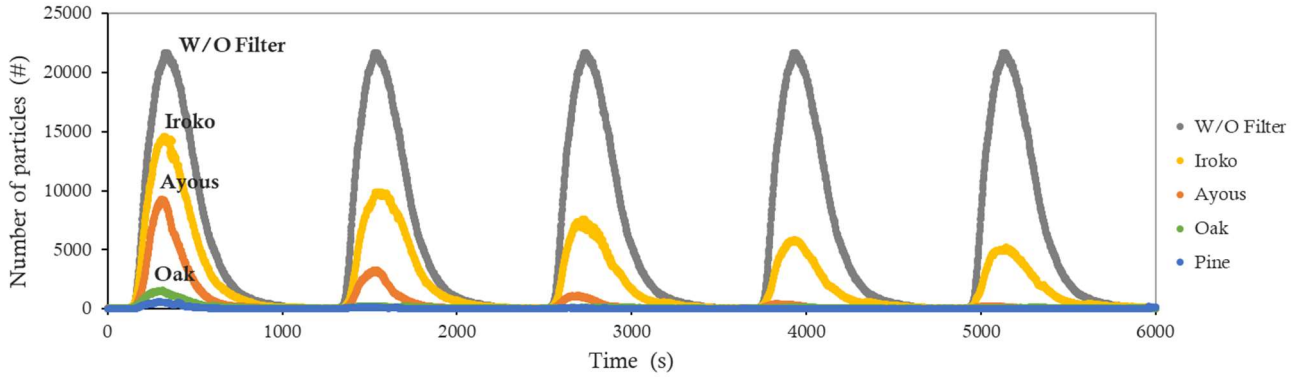

Figure 4.18. Number of particles measured downstream the axial filter samples along five full cycles of operation of the boiler

The non-constant mode of operation of the boiler has revealed through this work the probabilistic nature of the particle trapping phenomenon. Along one single cycle, filtration efficiency of the samples does not display a monotonically increasing function as would be expected in a stationary test, but varies depending on the moment and, possibly, on the amount of particles it has to face in one particular moment. Figure 4.19 shows this effect in the first cycle, and Figure 4.20 shows the evolution all through the entire test. Although the final efficiency of any cycle is higher than the initial one, and so the net efficiency grows every cycle, there's a maximum around 500-600 seconds after the cycle begins which leads us to suppose a dependency on the particle concentration.

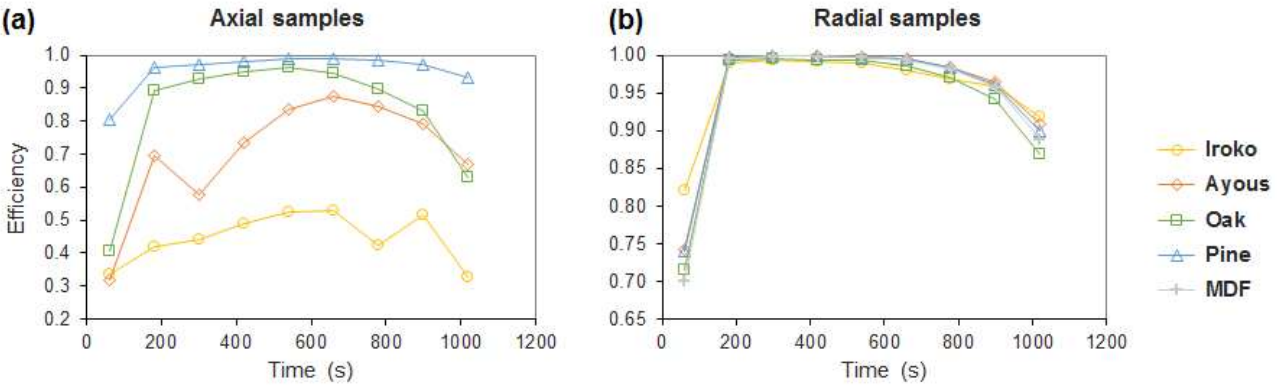

Figure 4.19. Efficiency evolution, averaged every 150 s, during boiler's first cycle, (a) Axial samples (b) Radial samples

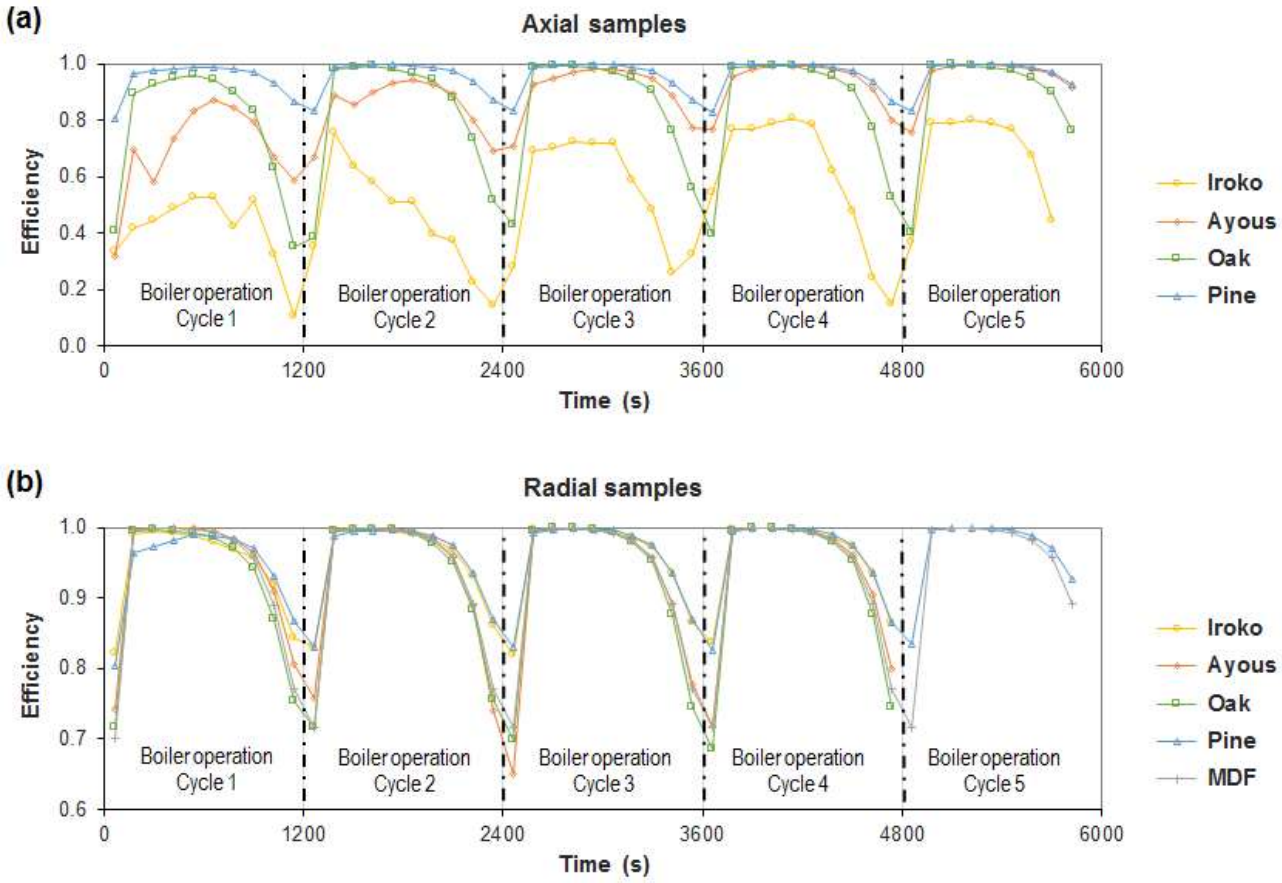

Figure 4.20. Efficiency evolution, averaged every 120 s, along the whole test,
(a) Axial samples (b) Radial samples

In order to compare the particles retention capacity of the samples, similar graphs have been made where efficiency is represented versus soot load (Figure 4.21). The higher the filtration efficiency of the sample, the higher the soot load it reaches. In radial samples, where the efficiency is always above 95%, differences between efficiency-soot load curves are almost unnoticeable.

This dependency of the efficiency on other parameters unrelated to the intrinsic nature of the precursors and the soot load, make it hard to set characteristic values for filtration efficiency for the samples, in isolated time moments like, for example, the very initial one. For this study, we have characterized the samples by averaging the efficiency values along complete cycles of boiler operation. Results are shown in Table 4.8. Results of Table 4.8 show that the initial efficiency of filters made from natural precursors is severely determined by the cutting direction. When the wood is cut radially, the initial efficiency of the resulting bioSiC filter is higher than 95%. Nevertheless, when the cut of the wood is axial, the efficiency depends on the pore size and the permeability, reaching in some cases values in the range 70-90%.

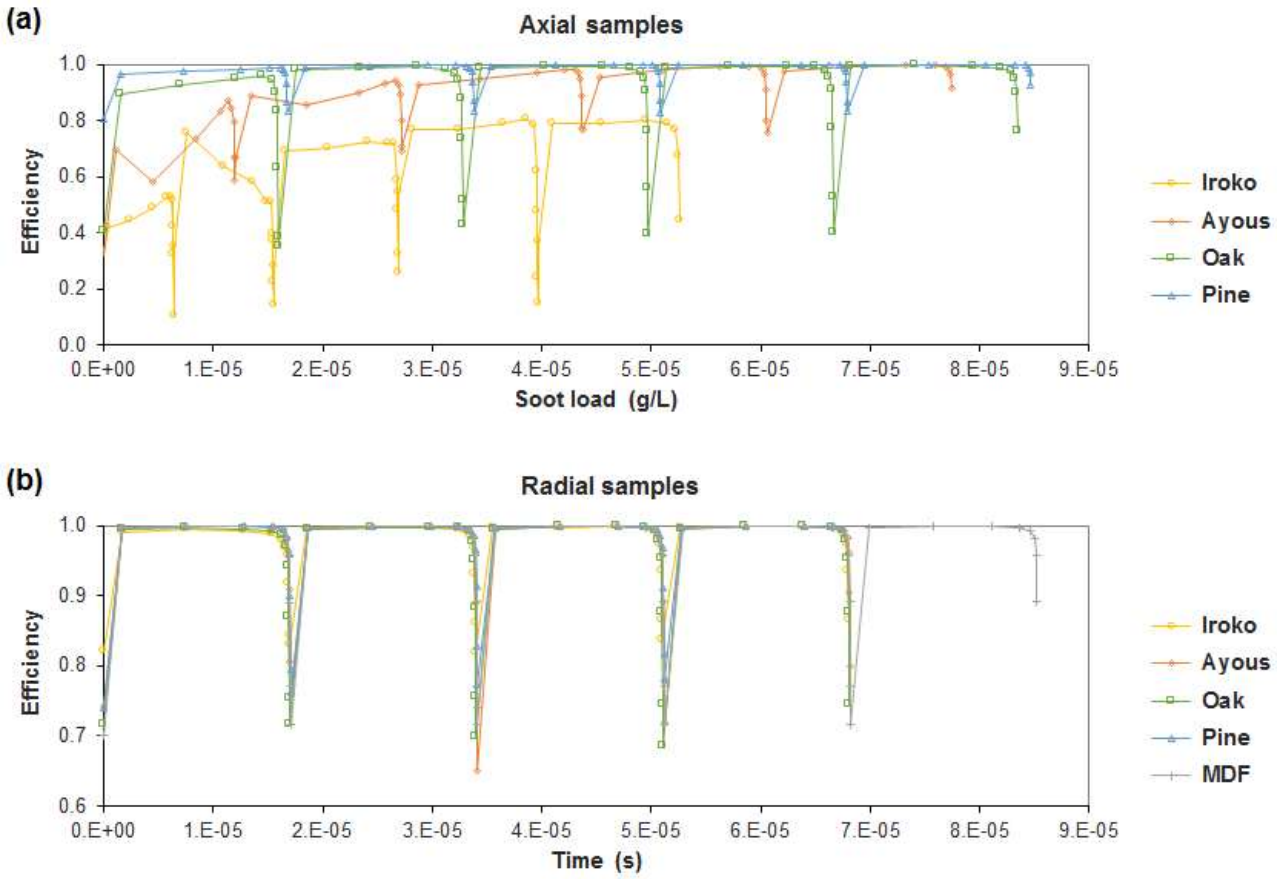

Figure 4.21. Efficiency evolution with soot load, averaged every 120 s, along the whole test, (a) Axial samples (b) Radial samples

When considering these average values of efficiency in every independent cycle, the evolution with the soot load do follow a monotonically increasing function as it is repeatedly reported in the literature [23,24]. In general, after several operation cycles, all samples reach more than 95% efficiency except axial Iroko. Figure 4.22 shows the evolution of the filtration efficiency along the complete test.

Table 4.8. Evolution of the average efficiency in the 5 cycles of the tests

Sample		Cycle 1	Cycle 2	Cycle 3	Cycle 4	Cycle 5
Ayous	Axial	0.703	0.89	0.96	0.983	0.99
	Radial	0.997	0.997	0.996	0.997	
Pine	Axial	0.978	0.993	0.996	0.997	0.997
	Radial	0.997	0.997	0.997	0.998	
Iroko	Axial	0.374	0.527	0.659	0.739	0.749
	Radial	0.988	0.993	0.995	0.996	
Oak	Axial	0.934	0.981	0.987	0.988	0.988
	Radial	0.992	0.995	0.996	0.996	
MDF	Radial	0.996	0.996	0.996	0.996	0.996

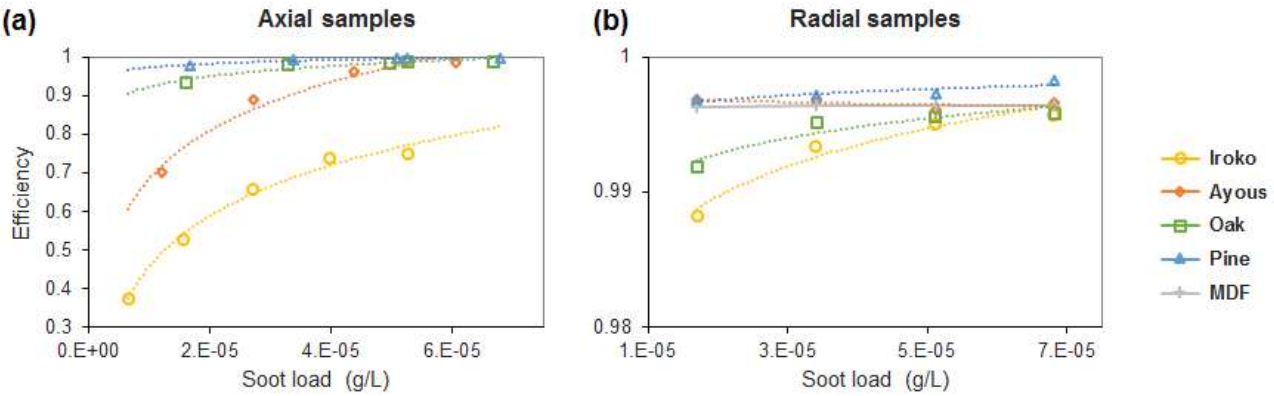

Figure 4.22. Evolution of the filtration efficiency with the soot load
(a) Axial samples. (b) Radial samples

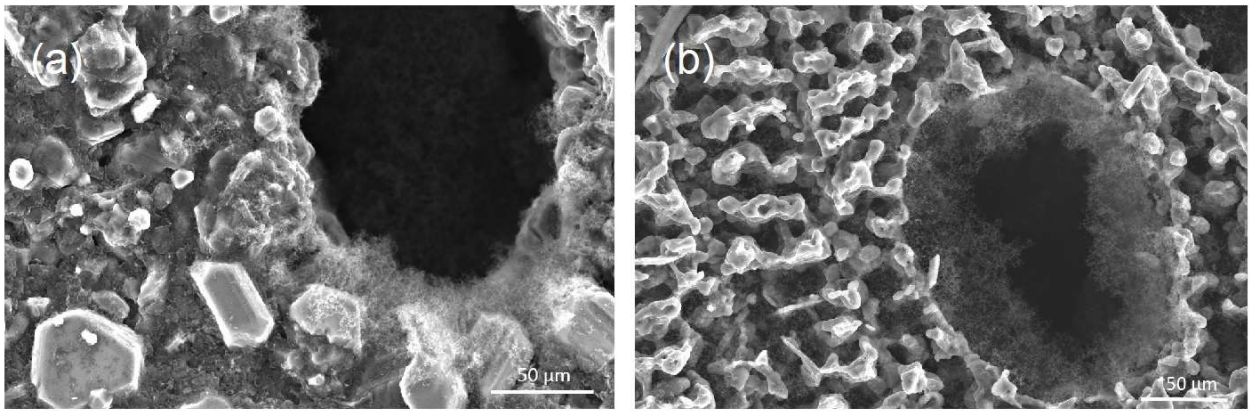

Figure 4.23. SEM micrographs taken after the tests of two soot loaded samples
(a) BioSiC from axial Iroko (b) BioSiC from axial Ayous

The growth rate in the efficiency of axial-Iroko-bioSiC is noticeably lower, likely due to the little tortuosity and low specific surface of its large macroscopic pores (see tables 4.2 and 4.3). Despite having similar pores sizes, Iroko and Ayous samples show different performances. The internal tortuosity and specific surface of some samples may cause a higher accumulation of particles in the walls of the pores and lead eventually to the closure of these pores (Figure 4.23).

4.5. Summary of microstructural, physical and chemical parameters of the studied bioSiC specimens

The most notable feature of bioSiC compared to traditional granular SiC is its hierarchical microstructure that replicates the microstructure of the original biological tissue. With the chosen precursors, a wide variety of porosities is obtained. Some of them below and some of them above the typical values of porosity in commercial filters. The porosimetry study reveals that, except pine, all bioSiC samples made from natural precursors present a trimodal

distribution of pores. Among the three present ranges of pores, the first one (the one corresponding to the nanopores) can be ignored due to its limited influence in the filtration process. On the contrary, the third range (corresponding to the largest pores) will be decisive in the applicability of the material to filtration processes since, as demonstrated in the last part of the study, the presence of these macropores may reduce considerably the filtration efficiency of the material. In the last chapter of this thesis, the possibility of choosing these precursors with large pores to reduce the pressure drop of the filter will be analysed, since the filtration efficiency of the manufactured prototypes turned out to be at the end of the day more than enough to comply with the European Regulations. Finally, the second range of pores (the one including pores between 2 and 60 microns, is relevant due its similarity with the typical pore size in a commercial substrate. The specific surface has turned out to be low in this biomorphic materials. However, further analysis is needed to understand the consequences of this fact in its filtration performance.

The thermal and mechanical properties of bioSiC have demonstrated to be highly dependent on the cutting direction of the wood. Unfortunately, the coefficient of thermal expansion was measured only in one direction, but both the thermal conductivity and the mechanical strength have turned out to be higher for axial samples than for radial ones. The reason for that can be directly associated to the microstructure: to the orientation of the pores and the fibres. In axial samples, the heat flux is applied in the same direction than the pores are arranged, so the diffusion is favoured. Besides, in axial samples, the mechanical load is also applied in the same direction than the fibres, so they exert a higher resistance. Despite that, both the thermal conductivity and the mechanical strength of bioSiC are lower than those of monolithic β-SiC. This may have a negative effect on its performance during the regeneration process, but may be compensated by the coefficient of thermal expansion. These three properties are responsible of the response of this material against thermal shock. In Chapter 6, a deeper analysis on the Thermal Shock Resistance of biosiC will be addressed.

The phase and the TGA-DSC analysis have shown that possible compositional deviations from the expected one could have taken place. The TGA-DSC analysis has shown the presence of some residual carbon in the samples after the silicon infiltration. On the other hand, the X-ray diffraction patterns shows the presence of α-SiC, which could have been formed during the silicon evaporation at temperatures above 1800 ºC.

BioSiC anisotropy is also reflected in its permeability and its filtration efficiency. The arrangement of the pores sets the crossing path for both the gas flux and the particles, so that axial samples are more permeable to gas, but also easier to be traversed by particles (they have less efficiency). On the contrary, radial samples are less permeable but have higher filtration efficiencies. The presence of large pores (> 200 μm) may also affect significantly the permeability or the filtration efficiency. The soot particles cannot easily create bridges and accumulate in large pores so the soot cake in these specimens is interrupted by holes that continue letting particles pass. As a result, the filtration efficiency of these specimens don't reach values close to 100% as in other samples.

As a summary, a qualitative heatmap has been constructed, where the suitability of each bioSiC for its use as substrate for DPFs is indicated through a color scale.

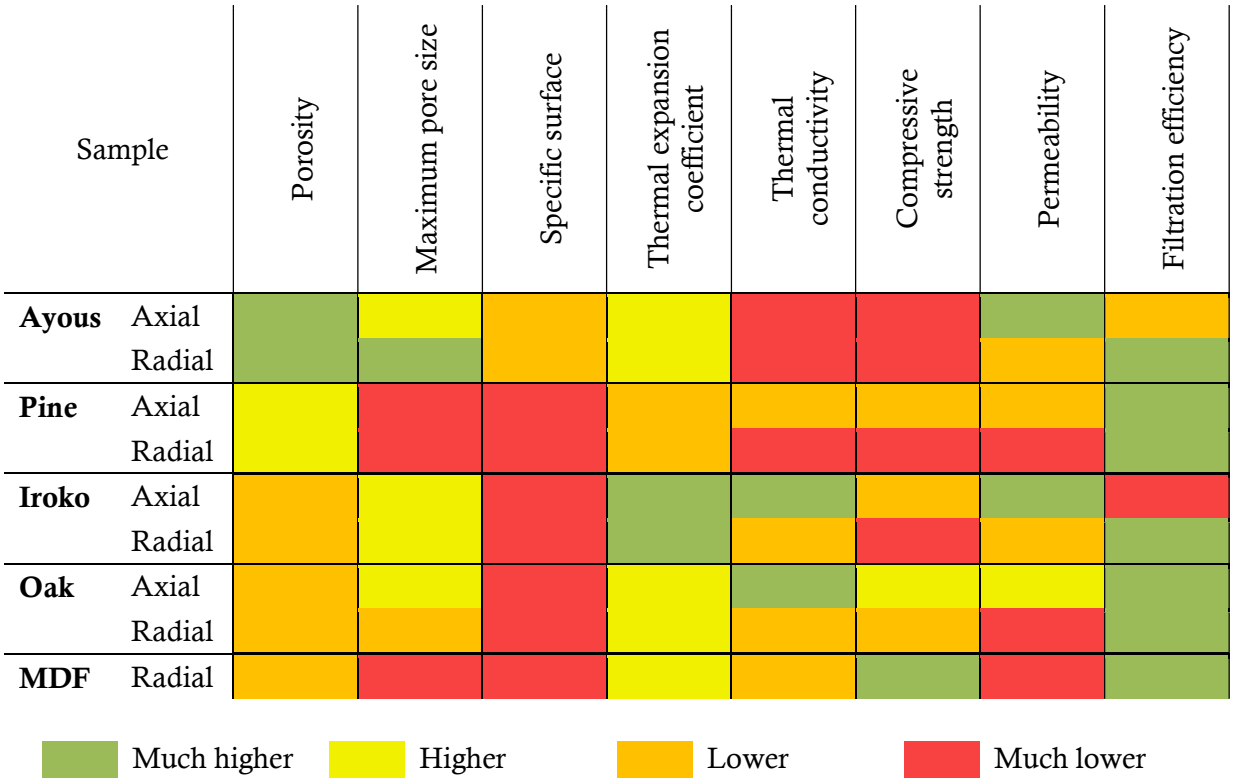

Figure 4.24. Summary of microstructural, physical and chemical parameters of the studied bioSiC specimens

Taking these results into account, a selection of a suitable precursor for manufacturing a prototype was made. In principle, there is not any precedent study about bioSiC Diesel Particulate Filters, so the transfer from laboratory scale to pilot scale could generate not predictable results. Considering that the only objective limitation over these systems is imposed by the regulations and affects only the number and the mass of particles they can retain, the selection was based mainly on efficiency criteria. That is, the choice was made over those precursors that yielded higher filtration efficiencies. At this point, the cutting direction was a double-edged sword. On the one hand, radial samples presented higher filtration efficiency. On the other hand, the arbitrariness of the vegetal tissue, along with the sensibility of the manufacturing process to small deviations in the cutting of the wood, could lead to a large scattering in the results when using a natural precursor for making the first prototypes. Hence, based on practical and manufacturing reasons, the first prototypes were finally made of Medium Density Fibreboard instead of using any of the natural precursors that had shown higher efficiencies when tested in the radial direction during the preliminary study.

In line with this choice, Chapter 6 will analyse the use of MDF in the substrate of a wall-flow DPF automotive filter. In DPFs, not only the capture efficiency is relevant but also the effect on

engine's exhaust backpressure, that directly affects to the global engine's efficiency. The results presented in Chapter 6 will reveal that other relevant criteria should be taken into account for the selection of the precursor apart from the filtering capacity.

Bibliography

[1] De Arellano-López AR, Martínez-Fernández J, González P, Domínguez C, Fernández-Quero V, Singh M. Biomorphic SiC: A New Engineering Ceramic Material. Int J Appl Ceram Technol 2005;1:56–67.

[2] Orlova TS, Popov V V., Quispe-Cancapa J, Hernández-Maldonado D, Enrique Magarino E, Varela-Feria FM, et al. Electrical properties of biomorphic SiC ceramics and SiC/Si composites fabricated from medium density fiberboard. J Eur Ceram Soc 2011;31:1317–23. doi:10.1016/j.jeurceramsoc.2010.06.015.

[3] Snead LL, Nozawa T, Katoh Y, Byun T, Kondo S, Petti DA. Handbook of SiC properties for fuel performance modeling. J Nucl Mater 2007;371:329–77. doi:10.1016/j.jnucmat.2007.05.016.

[4] Greil P, Lifka T, Kaindl A. Biomorphic Cellular Silicon Carbide Ceramics from Wood: I. Processing and Microstructure. J Eur Ceram Soc 1998;18:1961–73.

[5] Uchida Y, Ichikawa S, Harada T, Hamanaka T. Durability Study on Si-SiC Material for DPF. SAE Tech Pap 2003;2003-01–03:1–6.

[6] Miwa S, Abe F, Hamanaka T, Yamada T, Miyairi Y. Diesel Particulate Filters Made of Newly Developed SiC. SAE Tech Pap 2001;2001-01–01:1–8.

[7] Kaul VS, Faber KT, Sepúlveda R, De Arellano-López AR, Martínez-Fernández J. Precursor selection and its role in the mechanical properties of porous SiC derived from wood. Mater Sci Eng A 2006;428:225–32. doi:10.1016/j.msea.2006.05.033.

[8] Torres-Raya C, Hernandez-Maldonado D, Ramírez-Rico J, García-Gañán C, De Arellano-López AR, Martínez-Fernández J. Fabrication, chemical etching, and compressive strength of porous biomimetic SiC for medical implants. J Mater Res 2008;23:3247–54. doi:10.1557/JMR.2008.0392.

[9] Calderon NR, Martinez-Escandell M, Narciso J, Rodríguez-Reinoso F. The role of carbon biotemplate density in mechanical properties of biomorphic SiC. J Eur Ceram Soc 2009;29:465–72. doi:10.1016/j.jeurceramsoc.2008.05.049.

[10] Frevel LK, Petersen DR, Saha CK. Polytype distribution in silicon carbide. J Mater Sci 1992;27:1913–25. doi:10.1007/BF01107220.

[11] Eom J-H, Kim Y-W, Song I-H, Kim H-D. Processing and properties of polysiloxane-derived porous silicon carbide ceramics using hollow microspheres as templates. J Eur Ceram Soc 2008;28:1029–35. doi:10.1016/j.jeurceramsoc.2007.09.009.

[12] Singh M, Salem JA. Mechanical properties and microstructure of biomorphic silicon carbide ceramics fabricated from wood precursors. J Eur Ceram Soc 2002;22:2709–17. doi:10.1016/S0955-2219(02)00136-X.

[13] Najmi H, El-tabach E, Chetehouna K, Gascoin N, Falempin F. Effect of flow configuration on Darcian and Forchheimer permeabilities determination in a porous

composite tube. Int J Hydrogen Energy 2016;41:316–23. doi:10.1016/j.ijhydene.2015.10.054.

[14] Tandon P, Heibel A, Whitmore J, Kekre N, Chithapragada K. Measurement and prediction of filtration efficiency evolution of soot loaded diesel particulate filters. Chem Eng Sci 2010;65:4751–60. doi:10.1016/j.ces.2010.05.020.

[15] Tritscher T, Zerrath AF, Elzey S, Han HS. Data Merging of Size Distributions from Electrical Mobility and Optical Measurements. Eur. Aerosol Conf. Handb., 2013.

[16] DeCarlo PF, Slowik JG, Worsnop DR, Davidovits P, Jimenez JL. Particle Morphology and Density Characterization by Combined Mobility and Aerodynamic Diameter Measurements. Part 1 Theory. Aerosol Sci Technol 2004;38:1185–205. doi:10.1080/02786826.2004.10399462.

[17] Tien C, Brenner H. Mechanisms of Particle Deposition. Granul. Filtr. Aerosols Hydrosols, Butterworths Series in Chemical Engineering; 1989, p. 103–38.

[18] Ohara E, Mizuno Y, Miyairi Y, Mizutani T, Yuuki K, Noguchi Y, et al. Filtration Behavior of Diesel Particulate Filters (1). SAE Tech Pap 2007 World Congr Detroit, MI; United States 2007.

[19] Mizutani T, Kaneda A, Ichikawa S, Miyairi Y, Ohara E, Takahashi A, et al. Filtration Behavior of Diesel Particulate Filters (2). SAE Tech Pap 2007 World Congr (SAE Tech Pap 2007) 2007.

[20] Matti Maricq M. Chemical characterization of particulate emissions from diesel engines: A review. J Aerosol Sci 2007;38:1079–118. doi:10.1016/j.jaerosci.2007.08.001.

[21] Park K, Feng C, Kittelson DB, McMurry PH. Relationship between Particle Mass and Mobility for Diesel Exhaust Particles. Environ Sci Technol 2003;37:577–83.

[22] Wierzbicka A, Nilsson PT, Rissler J, Sallsten G, Xu Y, Pagels JH, et al. Detailed diesel exhaust characteristics including particle surface area and lung deposited dose for better understanding of health effects in human chamber exposure studies. Atmos Environ 2014;86:212–9. doi:10.1016/j.atmosenv.2013.11.025.

[23] Bautista MA, Cancapa JQ, Martínez-Fernández J, Rodríguez MA, Singh M. Microstructural and mechanical evaluation of porous biomorphic silicon carbide for high temperature filtering applications. J Eur Ceram Soc 2011;31:1325–32. doi:10.1016/j.jeurceramsoc.2010.06.014.

[24] De Mello Innocentini MD, Coury JR, Fukushima M, Colombo P. High-efficiency aerosol filters based on silicon carbide foams coated with ceramic nanowires. Sep Purif Technol 2015;152:180–91. doi:10.1016/j.seppur.2015.08.027.

Chapter 5
General applicability of bioSiC as filter material

Along with the geometrical design, the precursor selection of the biomorphic substrate is the most influencing factor in the performance of a final bioSiC wall-flow DPF prototype. The characterization study conducted in this research work includes five precursors, but the variety of plant species in nature is countless. The identification of natural trends or correlations between known (previously measured) microstructural parameters of the wood, and the resulting performance parameters would ease the search of the best precursor for making a bioSiC-based element; not only for this, but for any other application in the market.

In Chapter 4, the main results of the functional characterization study of the bioceramic material were presented. Direct measurements of density, porosity, pore size, thermal conductivity, thermal expansion coefficient, compressive strength, permeability and intrinsic efficiency were provided. The purpose of this chapter is to analyse more deeply the obtained results in order to draw significant relationships between functional parameters, and to foresee the potential of other wood precursors with different microstructure for their application as substrate in wall-flow DPFs.

This chapter is subdivided into eight sections. Sections 5.1 to 5.5 present some useful relationships that can help to predict the thermal and mechanical behaviour of other bioSiC substrates based on their microstructural features. The dependency of the permeability on the pore size explored in Section 5.1 is particularly noteworthy since it is directly related to the pressure drop and, consequently, to the technical feasibility of the filter as aftertreatment system for internal combustion engines. In Section 5.2, an empirical correlation between intrinsic filtration efficiency and permeability is proposed. Section 5.3 analyses the relative contribution of viscous and inertial effects to the total pressure drop. Sections 5.4 and 5.5 address the dependency on the microstructure of the thermal conductivity and the compression strength respectively. The remaining sections make a more general and qualitative approach to the applicability of bioSiC as DPF substrate for automotive applications. Section 5.6 analyses the potential of bioSiC compared to other traditional ceramic substrates; and Section 5.7 reports some economic aspects of the manufacture of this novel system, foreseeing the feasibility of a hypothetical massive production of bioSiC wall-flow DPFs. The results of this chapter might have high interest and

potential impact in the ceramic materials sector. The observations and the empirical relationships presented in this chapter can be also found in the following publications.

Related publications

1. A. Gómez-Martín, M.P. Orihuela, J.A. Becerra-Villanueva, J. Martínez-Fernández, J. Ramírez-Rico. *Permeability and mechanical integrity of porous biomorphic SiC ceramics for application as hot-gas filters*. Materials & Design, Vol. 107, 450–460, 2016. doi: 10.1016/j.matdes.2016.06.060
2. A. Gómez-Martín, M.P. Orihuela, J. Ramírez-Rico, R. Chacartegui, J. Martínez-Fernández. *Thermal conductivity of porous biomorphic SiC derived from wood precursors*. Ceramics International, Vol. 42, Iss. 14, 16220–16229, 2016. doi: 10.1016/j.ceramint.2016.07.151
3. M.P. Orihuela, A. Gómez-Martín, J.A. Becerra-Villanueva, R. Chacartegui, J. Ramírez-Rico. *Performance of biomorphic Silicon carbide as particulate filter in diesel boilers*. Journal of Environmental Management, Vol. 203, Iss. 3, 907-919, 2017. doi: 10.1016/j.jenvman.2017.05.003

5.1. Permeability dependency on the microstructure

Predicting the permeability of a sample attending to its microstructural parameters is useful for assessing the viability of the material in subsequent filtering applications. Recent studies have been conducted on other ceramic materials to determine their permeability and to assess the influence of their microstructure on the resulting pressure drop and efficiency [1,2]. These parameters have been demonstrated to depend on volume fraction of porosity as a first approximation, but also on pore size and connectivity [3]. If the permeability is known as a function of the microstructure, then the pressure drop can be predicted under a given flow rate and the microstructure can be improved by tailoring pore characteristics [4].

Relevant microstructural parameters such as pore size, surface area and total porosity were thoroughly studied in this work to understand their influence in the permeability values because, as observed, the permeability values differed up to one order of magnitude due to the difference in microstructure of each precursor and orientation. In previous works on porous ceramics, gas permeability proved to be directly dependent on the total pore-volume fraction [5], tortuosity, and the average pore size of the sample [5–8].

Furthermore, permeability depends not only on the wood precursor, but on the selected cutting direction. As observed in previous Chapters (see Section 4.4.1), permeability depends mostly on the relative orientation of the gas flow respect to the cells and fibres arrangement. Permeability is inversely proportional to tortuosity [9]. Consequently, in all samples, permeability was higher in the axial direction than in the radial one. This trend is due to the orientation of the elongated pores and their interconnectivity compared with the direction of the gas flow causing less

tortuosity of the air flow. If the material presents large macro-pores, as Iroko-bioSiC does, the resulting permeability is even higher, deviating from the observed general trend. On the contrary, generally accessible techniques for porosity and surface area determination, such as gas adsorption or mercury intrusion porosimetry, yield scalar, volume-averaged values of the pore size distribution even for an anisotropic material. This is so because the gas, or the Hg, penetrates all interconnected pores regardless their orientation, whereas in a permeability experiment only those pores aligned with the gas stream will contribute significantly to flow. This disparity introduces an additional issue to be taken into account when predicting the permeability of any bioSiC specimen from its microstructural characteristics. Despite that, in this work, a direct relationship between the effective pore size and the permeability was obtained as follows [10].

Some theoretical models in the literature proposed a prediction of permeability in porous media by structural parameters, the most popular among these having been developed by Ergun [11]. This model proposes a general correlation between pressure drop and gas-flow velocity when a fluid flows through granular beds. From this model the permeability constants are given by:

$$k_1 \propto \frac{\varepsilon^3 {d_p}^3}{(1-\varepsilon)^2} \qquad \text{Eq. 5.1}$$

$$k_2 \propto \frac{\varepsilon^3 d_p}{(1-\varepsilon)} \qquad \text{Eq. 5.2}$$

where ε is the volume fraction of porosity and d_p is defined as an equivalent particle diameter of the granular media. Based on previous studies of cellular materials, d_p can be replaced by an equivalent pore diameter, d [4,12]. When the grains of the samples are spherical, the following relationship between particle size and pore size is proposed [1]:

$$d_p = \frac{3}{2}\frac{(1-\varepsilon)}{\varepsilon} d \qquad \text{Eq. 5.3}$$

Permeability constants from this modification of Ergun's model, taking into account an equivalent pore size, can be rewritten as:

$$k_1 = \frac{\varepsilon d^2}{A} \; ; \quad k_2 = \frac{\varepsilon^2 d}{B} \qquad \text{Eq. 5.4}$$

In previous works, Ergun equations agreed reasonably well with k_1, but these overestimated the inertial term [1,4]. Since Ergun's model normally did not provide an overall agreement with experimental data because it was developed for granular beds, and this is not suitable for cellular materials, many researchers have considered these equations modifiable and have already proposed different numerical constants and empirical parameters related to the microstructure of each cellular material [2,12]. A review on this subject has been presented by Macdonald et al. [13]. Most previous works assumed a monomodal and isotropic porosity and their applicability to bioSiC is questionable since it exhibits a complex anisotropic porous microstructure consisting

of a SiC scaffold formed by a cluster of SiC grains and a multimodal pore size distribution inherited from the wood precursor, so that it is more difficult to model the gas flow forced to travel through these porous media instead of isotropic materials [14,15]. In particular, for a bimodal pore size distribution such as that observed in bioSiC for the axial direction, there is a difficulty in selecting the equivalent pore size d since the arithmetic mean will be biased towards the most abundant but smaller narrow channels thus underestimating the effective pore size. Fortunately, the effective pore size can be calculated from the pore size distribution accessible through Hg intrusion porosimetry.

Let us consider a set of cylindrical channels of radius r_i and length L, then the flow through them for a given pressure drop ΔP can be calculated using the Hagen-Poiseuille relationship:

$$Q_i = \frac{\Delta P}{8\eta L}\pi {r_i}^4 = \frac{\Delta P}{8\eta L}\pi {r_i}^2 {r_i}^2 \qquad \text{Eq. 5.5}$$

Dividing by the total area we find the flow per unit area:

$$q_i = \frac{\Delta P}{8\eta L}\frac{\pi {r_i}^2}{A}{r_i}^2 = \frac{\Delta P}{8\eta L}\alpha(r_i)\cdot {r_i}^2 \qquad \text{Eq. 5.6}$$

Where $\alpha(r_i)$ represents the area fraction of the pores with radius r_i. If the pores are perfect, aligned cylinders then $\alpha(r_i)$ is equal to $f(r_i)$, the volume fraction of pores of radius r_i, a quantity directly measured by porosimetry. Summing the contribution of all types of and using $v = \varepsilon q$ one finds:

$$v = \varepsilon\frac{\Delta P}{8\eta L}\sum_i f(r_i)\,{r_i}^2 \qquad \text{Eq. 5.7}$$

And thus the linear permeability is, in terms of the pore diameter $d_i = 2r_i$:

$$k_1 = C\varepsilon\bar{d}^2 \qquad \text{Eq. 5.8}$$

Where C is a constant that describes the pore geometry and is equal to $1/32$ for cylindrical pores and:

$$\bar{d}^2 = \sum_i f(r_i)\,{r_i}^2\,; \quad \sum_i f(r_i) = 1 \qquad \text{Eq. 5.9}$$

Thus, according to this calculation, the relevant pore size is not the mean but instead the square root of the quadratic mean, which is biased towards the larger pores. This is reasonable since flow depends on the fourth power of the pore radius and thus pores twice as large will carry 16 times the flow for a given pressure drop.

Due to the anisotropy of bioSiC, if we want to rationalize the measured permeabilities in terms of the microstructure, two equivalent pore sizes should be used: one for the axial and another for

the radial direction. Unfortunately, the measured pore size distribution is an orientation-average of the anisotropic one, so a criterion for the calculation of effective pore sizes needs to be applied. Since bioSiC exhibits large channels only in the axial direction, and these are in general larger than 100 μm, the author proposes using Eq. 5.9 with the whole pore size distribution for the axial direction. On the contrary, in the radial direction there are no large channels, so the author proposes using the same approach but applying a cut-off in the pore size distribution of 100 μm. Up to that pore size, the distribution is mostly monomodal and thus the effective pore size is very close to the mean pore size.

Since the porosities of all the materials studied in this work are similar (except for the Ayous-derived bioSiC), it is foreseeable that k_1 will present a correlation with d. In order to find the trend, Figure 5.1 was built plotting k_1 versus d. Figure 5.1 shows the measured permeability of the specimens as a function of their effective pore size calculated using the criteria described above [10].

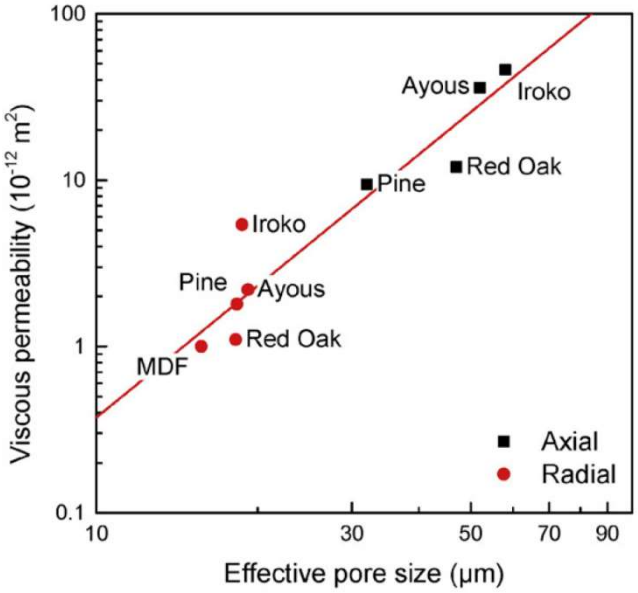

Figure 5.1. Permeability vs. effective pore size for bioSiC samples from different precursors in two orientations [10]

On the other hand, permeabilities can also be described in terms of the surface area per unit volume S_v as [16]:

$$k_1 = \frac{\epsilon^3}{\alpha {S_v}^2 (1-\epsilon)^2} \; ; \quad k_2 = \frac{\epsilon^3}{\beta S_v (1-\epsilon)} \qquad \text{Eq. 5.10}$$

where α and β are parameters that depend on the microstructure and are fitted to each porous material [13]. The geometrical surface area in Eq. 5.10 may be determined either experimentally or by assuming a model that describes the real geometry of the pores. Richardson et al. [16] examined three models [17] for estimating S_v in ceramic foams and found values that were similar to each other and proposed empirical equations for α and β in terms of the average pore size and

porosity, providing a good prediction of permeability constants. In particular, if porosity is described as a set of parallel cylinders with a constant diameter based on the hydraulic diameter model developed by Kozeny, the geometrical surface area may be determined as follows [16]:

$$S_v = \frac{4\varepsilon}{d(1-\varepsilon)} \qquad \text{Eq. 5.11}$$

And substituting Eq. 5.11 in Eq. 5.10 the Ergun model is recovered. The main problem of applying the model of Eq. 5.11 lies in the choice of a relationship between pore size and surface area per unit volume, and again the use of a single parameter for a material with an anisotropic, multimodal pore size distribution is questionable. The surface area can be estimated from the pore size distribution again considering that, for cylindrical pores:

$$S = 2\int_0^{V_\varepsilon} \frac{dV}{r} = 2V_\varepsilon \int_0^1 \frac{dV}{r} \qquad \text{Eq. 5.12}$$

Which is deduced from the area to volume ratio of a cylinder; V_ε is the volume of pores. Dividing by the total volume and writing the equation in discrete form:

$$S_v = 2\varepsilon \sum_i \frac{f(r_i)}{r_i} = 4\varepsilon \sum_i \frac{f(d_i)}{d_i} \qquad \text{Eq. 5.13}$$

Thus we could use Eq. 5.13 in conjunction with the Kozeny-Carman relationship of Eq. 5.10 to estimate an equivalent pore size. The validity of Eq. 5.13 for bioSiC can be tested by plotting the values of S_v measured directly from Kr adsorption against those calculated from pore size distribution data [10]. Figure 5.2 shows that this correlation is reasonable.

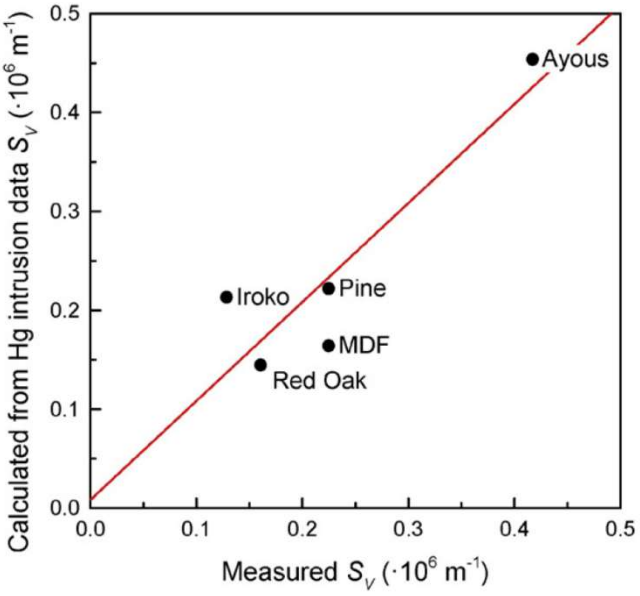

Figure 5.2. Specific surface area per unit volume calculated from the pore size distribution vs. S_v measured from Kr adsorption [10]

However, calculations of equivalent pore sizes from this approach yielded values in the 5–7 μm which are clearly too low to adequately represent the microstructural average in these materials. In the same way as the quadratic mean estimate results in effective pore sizes larger than the mean because it is weighted towards the larger channels, effective pore sizes calculated from surface areas are biased towards the smaller channels, which contribute the most to the surface area.

Panels A and B of Figure 5.3 plots measured viscous and inertial permeabilities against εd^2 and $\varepsilon^2 d$ respectively [10], as predicted by the Ergun relations of Eq. 5.4, where the values of d were chosen as different averages of the pore size distribution depending on whether the axial or radial orientations were considered, according to the previous discussion. For the viscous permeability, a reasonable agreement was found when A = (80±1) μm^2, whereas the inertial permeability did not follow Ergun's relationship. Instead, it was essentially constant for a given orientation, yielding (11.8±0.8) ·10^{-8} m and (5±3) ·10^{-8} m for axial and radial orientations, respectively.

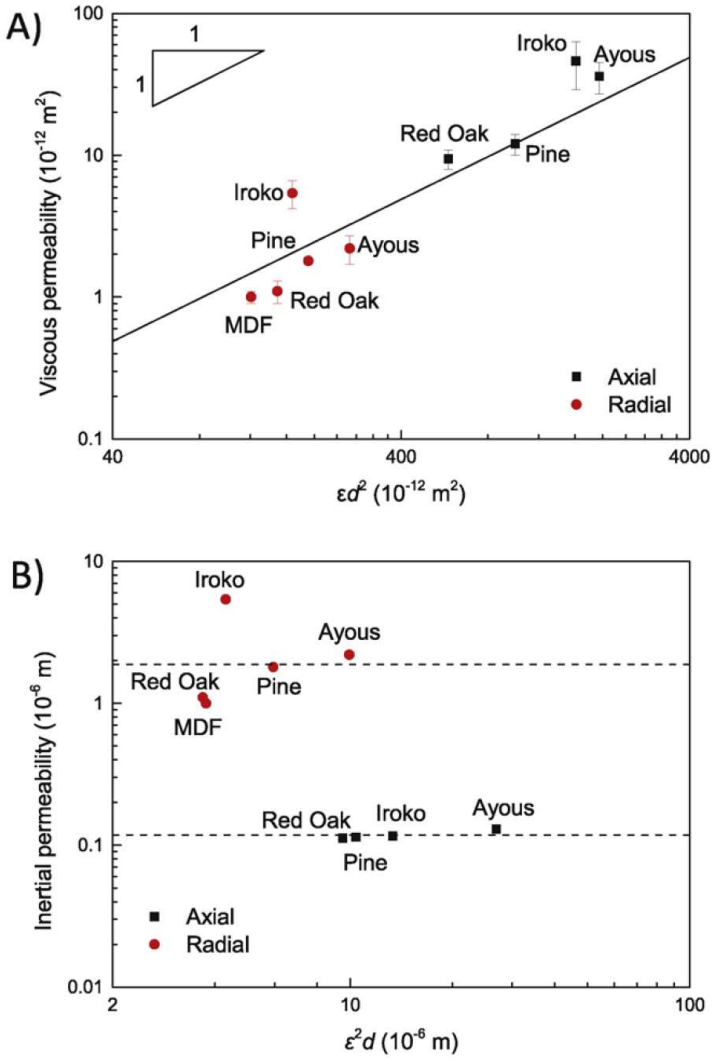

Figure 5.3. A) Viscous permeability k_1 vs. εd^2 and B) inertial permeability k_2 vs. $\varepsilon^2 d$ as dictated by Ergun's relationships, in both axial and radial directions [10]

These correlations can help to predict the range of permeability of porous SiC ceramics, although several precautions must be kept in mind. First, bioSiC samples do not have a set of perfectly cylindrical pores and thus deviations may occur. In addition, it is worth bearing in mind that not all the porosity may be available for fluid flow and the average pore size considered on the permeability constants from these models were calculated by intrusion porosimetry, which was a gross simplification because the whole size distribution of bioSiC samples was reduced to a single mean value [9,12], making it perhaps the greatest source of error. These models would also be improved by including additional microstructural parameters for complex structures such as tortuosity of the porous media which reflect the anisotropy of this material in both directions. Nevertheless, the values predicted by the proposed correlation reasonably agree with those calculated experimentally at least for the linear permeability and thus could be useful as a first benchmark to determine whether a wood precursor could be valid for a particular application [10].

5.2. Relationship between intrinsic filtration efficiency and permeability

Microstructural parameters of bioSiC may influence its capture efficiency as much as they influence the permeability. The initial efficiency tests with the lab-scale samples in the diesel boiler were useful to search direct relationships between the microstructural parameters of a wood-based bioceramic material and its filtration performance taking also into account the relative orientation of the flux and the cells which has proved to be one of the most relevant influences in the permeability of the bio-material [18]. This study with laboratory disk-shaped samples shows the filtering effect of the material, and it does not include the effect of DPF geometry in particles accumulation evolution as will be shown in the following chapter.

Table 5.1. Initial (clean state) intrinsic efficiency of the bioSiC samples

Sample		**Initial intrinsic efficiency**
Ayous	Axial	0.447
	Radial	0.838
Pine	Axial	0.876
	Radial	0.820
Iroko	Axial	0.353
	Radial	0.840
Oak	Axial	0.616
	Radial	0.827
MDF	Radial	0.807

In order to study the natural efficiency of bioSiC without taking into account the particle load, the average of its efficiency was calculated in the first 60 seconds of operation (test conditions and procedure in Section 3.3.4). The results are shown in Table 5.1.

For this work, the dependence of the efficiency on each parameter has been analysed: porosity, pore size, and specific surface. Given the complexity of biological microstructure, trends are not easy to find but when using a global parameter as permeability. In general, two statements can be made: i) the microstructure affects more axial samples than radial ones, and ii) porosity and specific surface are not as decisive in efficiency as pore size is.

For radial samples efficiency remains almost constant regardless the porosity and specific surface, while for axial samples not even a trend can be found. Pore size affects the filtration efficiency of bioSiC more than porosity or specific surface do. In this sense, two parameters were analysed: the most likely pore size (Figure 5.4a), and the maximum pore size (Figure 5.4b). This latter, the maximum pore size, generates a clearer trend: the larger the maximum pore size, the lower the filtration efficiency.

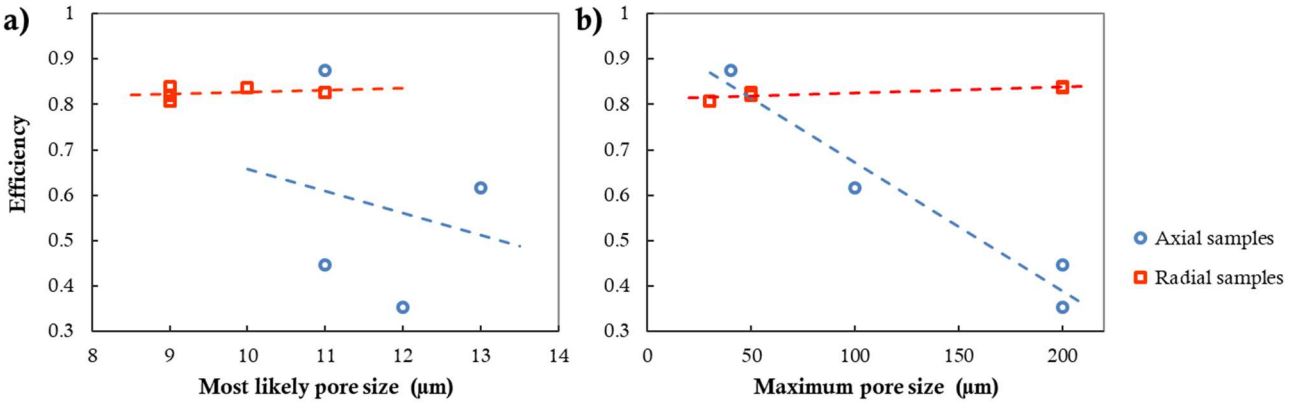

Figure 5.4. Initial efficiency of the bioSiC samples as a function of: a) the most likely pore size, and b) the maximum pore size

When it comes to microstructural characterization, permeability turns out to be the most representative parameter. In this work an experimental correlation based on the obtained results has been considered (Eq. 5.14) to get a general idea of the performance of this novel material when used in filtration applications [18].

$$\eta_N = e + \frac{k_1}{k_1 - k_0} \qquad \text{Eq. 5.14}$$

A hyperbolic relationship has been used where k_0 might represent the average maximum permeability of a clean bioSiC sample for which the initial efficiency is minimum; and e might be the average maximum initial efficiency of bioSiC for samples with low permeability. With $e = 0.84$ and $k_0 = 1.4 \cdot 10^{-10}$ the best fit is obtained. There is a significant scattering in the results

due to the microstructural variations of wood and to the differences between precursors. Figure 5.5 shows the experimental results obtained in this work and the proposed correlation curve.

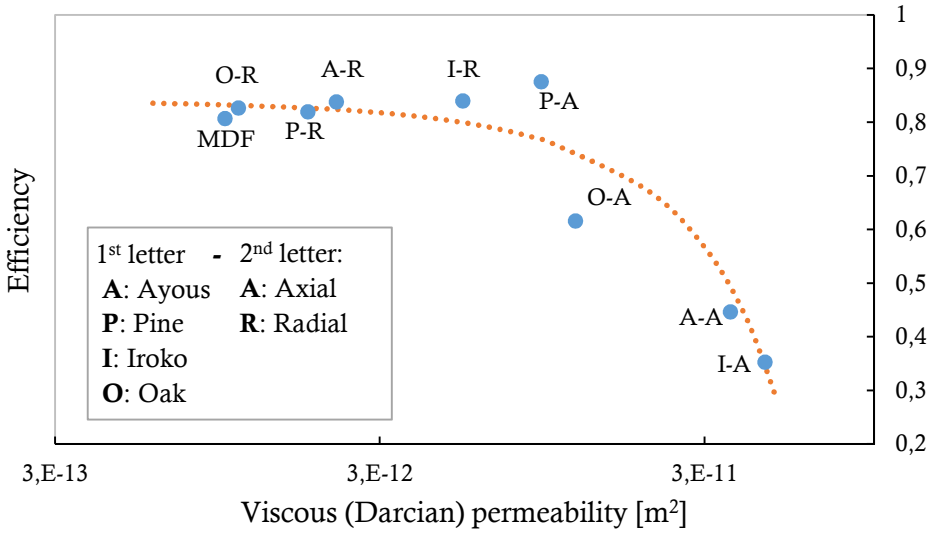

Figure 5.5. Dependence of bioSiC filtration efficiency on the permeability

The previous study on the permeability of bioSiC showed that this material has viscous (Darcian) permeabilities in the range 10^{-11}-10^{-12} m^2, and inertial terms in the range 10^{-7}-10^{-8} m, both promising values for hot-gas filtering applications [10]. Thus, the best precursors for making bioSiC particulate filters are those that have a high efficiency and high permeability, that is, those situated above the presented correlation curve. Among all the samples studied in this work, axial pine seems to be the best choice (Figure 5.5).

5.3. Contribution of viscous and inertial effects to total pressure drop

The Reynolds number Re for porous media is defined as the ratio between inertial and viscous effects, and allows the linear and nonlinear flow behaviour to be predicted [9]. Re is defined as:

$$Re = \frac{\rho v_i d}{\eta} \qquad \text{Eq. 5.15}$$

where v_i is the interstitial fluid velocity, which can be calculated between the difference on superficial velocity and the porosity ($v_i = v\varepsilon^{-1}$). For a Reynolds number less than one ($Re < 1$), the energy is dissipated due to viscous friction and the pressure drop can be determined simply by applying Darcy's law. For Reynolds numbers ranging between $1 < Re < 150$, the flow is also predominantly laminar but inertial effects at a small proportion are already present in the flow, while for $Re > 150 - 300$ the flow is mainly turbulent and unsteady.

Due to the difficulty of determining a representative pore size in complex porous media, Ruth and Ma proposed an alternative model in order to assess the flow regime [19], where relative

contributions of viscous and inertial effects on total pressure drop when a gas is flowing through a porous medium could be determined by the dimensionless Forchheimer's number [4]. It was defined as a function of the permeability constants according to Eq. 5.16.

$$F_0 = \frac{\rho v}{\eta}\frac{k_1}{k_2} \qquad \text{Eq. 5.16}$$

For $F_0 \ll 1$, viscous effects are dominant on the flow, while for $F_0 \gg 1$ the pressure drop is due mainly to inertial effects [20]. The individual contributions of viscous and inertial effects to total pressure drop from this parameter can thus be estimated as follows:

$$\frac{\Delta P_{viscous}}{\Delta P_{total}}(\%) = \frac{1}{1+F_0} \qquad \text{Eq. 5.17}$$

$$\frac{\Delta P_{inertial}}{\Delta P_{total}}(\%) = \frac{F_0}{1+F_0} \qquad \text{Eq. 5.18}$$

Table 5.2 reports the calculated F_0 and Figure 5.6 shows the dependence of both viscous and inertial contributions to the total pressure drop of each wood-bioSiC as a function of sample orientation under air-flow velocities ranging from 0.01 to 0.4 m/s [10].

Table 5.2. Forchheimer number (F_0) range of the bioSiC samples for air-flow velocity ranging from 0.01 to 0.4 m/s

Sample		**Forchheimer number F_0**
Ayous	Axial	0.17-6.91
	Radial	0.02-0.82
Pine	Axial	0.05-2.05
	Radial	0.02-0.79
Iroko	Axial	0.25-9.89
	Radial	0.03-1.35
Oak	Axial	0.07-2.72
	Radial	0.03-1.25
MDF	Radial	0.03-1.19

It was noted that the flow regime depended heavily on the direction of the sample. At very low gas velocities (0.01 m/s), the pressure drop in both orientations was due mainly to viscosity effects. Nevertheless, as air velocity increased, the contribution of inertial effects to total pressure drop became more remarkable in axial samples, being close to 90% at the highest velocity. Conversely, in radial samples viscosity effects were more efficient, showing a gentler drop with increasing flow velocity. At the highest velocity the ratio of the inertial part to the whole flow was close to 50%. This trend was also observed in the experimental curves presented in Chapter 4 (Figure 4.16). The pressure drop for radial samples was more consistent with Darcy's law,

following a linear trend with the increase in velocity, implying that flow was mainly laminar and losses of viscous energy were due to friction between gas layers [21].

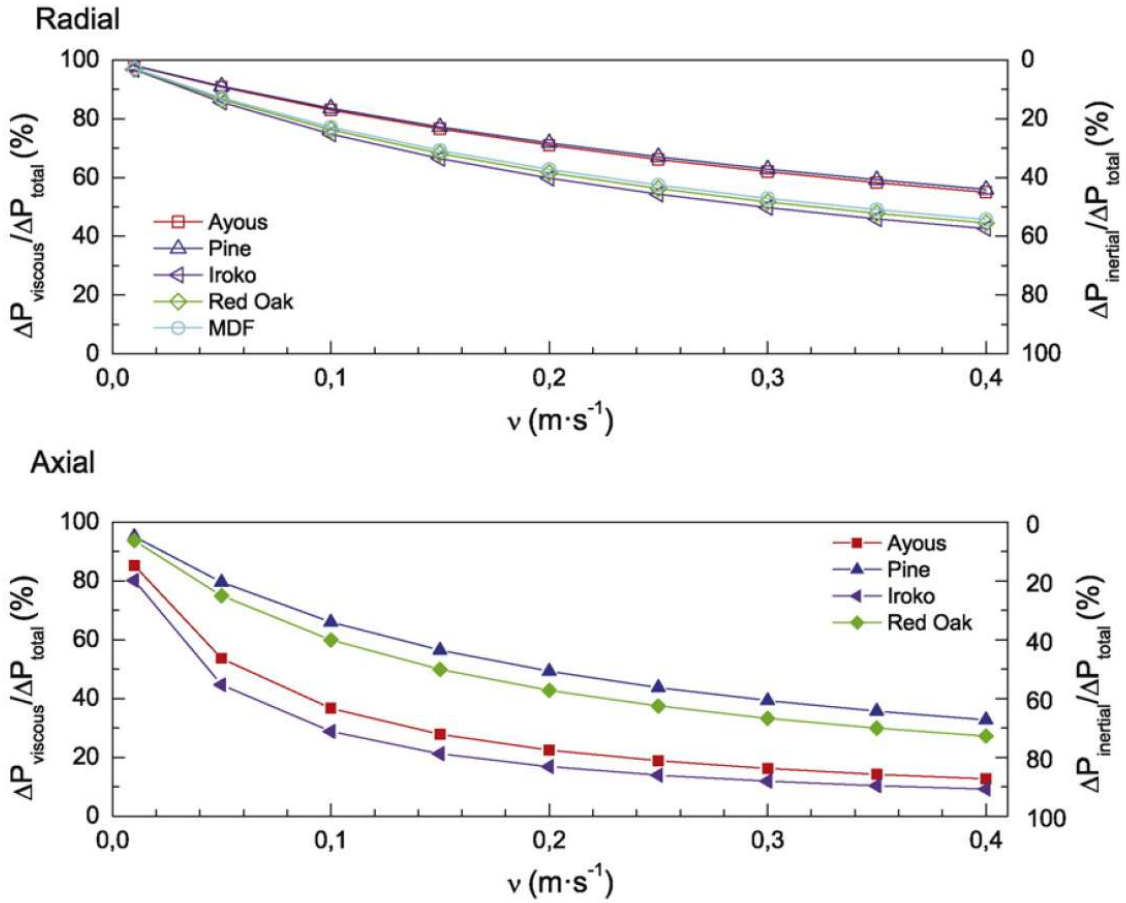

Figure 5.6. Viscous and inertial terms of the bioSiC samples as a percentage of total pressure drop, as a function of air-flow velocity [10]

Differences in the two contributions depending on the direction were due mainly to the anisotropy and the tortuosity of bioSiC, as well as the presence of large axial channels [10]. In axial samples, air flow traversed the straight, mostly cylindrical axial channels running to the sides of the samples with lower tortuosity than in the case of radial samples where, due to the absence of interconnected channels, the air flow travelled through the sample from the SiC grain boundaries, resulting in an orderly and laminar flow. For a given flow rate, inertial effects and turbulent flow will be more significant in the axial direction as the effective pore size and thus Reynolds number is higher than in the radial direction [10].

5.4. Thermal conductivity dependence on the microstructure

Porous biomorphic silicon carbide samples can be considered a two phase system: a combination of a dense solid silicon carbide scaffold and pores. In terms of the cellular solids theory developed

by Gibson and Ashby [17], the thermal conductivity of a porous material depends on four contributions:

$$k^* = k_s + k_g + k_c + k_r \quad \text{Eq. 5.19}$$

where k_s is the contribution through the porous solid, k_g is the conduction through the gas contained in the pores, k_c is the contribution due to convection and k_r the contribution of radiation.

Since the samples were tested in vacuum, conduction and convection inside the pores was not present, and radiative contributions has been shown to be negligible in this range of temperature [22]. The presence of pores in bioSiC samples can lead to a reduction in thermal conductivity because of the smaller solid fraction compared to dense SiC, but also because of a decreased mean free path for phonon transport as a result of phonon scattering at pores [23,24].

Thermal diffusivity measurements were performed on samples with porosity levels between 45% and 72%. At room temperature, it can be seen that thermal conductivity of porous silicon carbide material decreases from 88 to 26 $W \cdot m^{-1}K^{-1}$ in the axial direction and from 66 to 5 $W \cdot m^{-1}K^{-1}$ in the radial direction. This indicates that porosity affects thermal conductivity in ceramic materials due to a decrease in the solid phase of SiC and therefore an increased porosity leads to a decreased thermal conductivity, as expected. These results are consistent with other studies from the literature showing that porosity is a determinant factor in the reduction of the thermal conductivity [22,24,25]. It is not the only important parameter in the determination of thermal conductivity though; pore size and shape can also play a significant role.

There are several analytical models proposed to describe the thermal conductivity of porous materials according to pore size and fractional porosity. The model of Rice establishes that the thermal properties of a porous material can be described considering the minimum solid area (MSA) [26], that is the minimum area of solid material that can be found in any plane perpendicular to the excitation. This area depends on porosity, pore geometry and distribution. To apply this model, it has been considered that porous bioSiC samples have perfectly cylindrical pores aligned in a simple cubic arrangement, and thus the conductivity depends on the direction of heat flux due to pore anisotropy. As it has been shown, the thermal conductivity of a porous material with aligned pores in the directions parallel to the heat flow can be related to the fully bulk conductivity k_0 as a function of porosity following [22]:

$$k^*_{axial} = (1 - \varepsilon)k_0 \quad \text{Eq. 5.20}$$

On the other hand, in the radial direction, where the direction of heat flow is perpendicular to the pores, the thermal conductivity is given by:

$$k^*_{radial} = \left(1 - \left(\frac{4}{\pi}\varepsilon\right)^{1/2}\right)k_0 \quad \text{Eq. 5.21}$$

Simplified models related the thermal conductivity of anisotropic porous material as a function of the porosity fraction and the solid phase-contribution. Using the Litovskii equation [27], the conductivity for porous materials depends on porosity following:

$$k = k_0(1-\varepsilon)\sqrt{(1-\varepsilon)} \qquad \text{Eq. 5.22}$$

And Kingery et al. [25,28] describe the thermal conductivity of porous ceramics by the following equation:

$$k = k_0 \frac{(1-\varepsilon)}{(1+\varepsilon)} \qquad \text{Eq. 5.23}$$

where k_0 is the thermal conductivity of the bulk SiC and ε is the porosity fraction of the porous material.

Figure 5.7 compares the effective thermal conductivity calculated from the measured data and the effective thermal conductivity from [22] with the effective thermal conductivity predicted by the three models described above used in porous material in order to investigate the influence of porosity. The effective thermal conductivity ($k_{effective} = k^*/k_0$) was obtained by normalizing the experimental values by the theoretical thermal conductivity of fully dense SiC at each measured temperature, which is taken from [29] for small grained SiC ceramics. Theoretical effective thermal conductivities were calculated using Eq. 5.20-Eq. 5.23 taking into account the pore volume fraction of each type of biomorphic SiC.

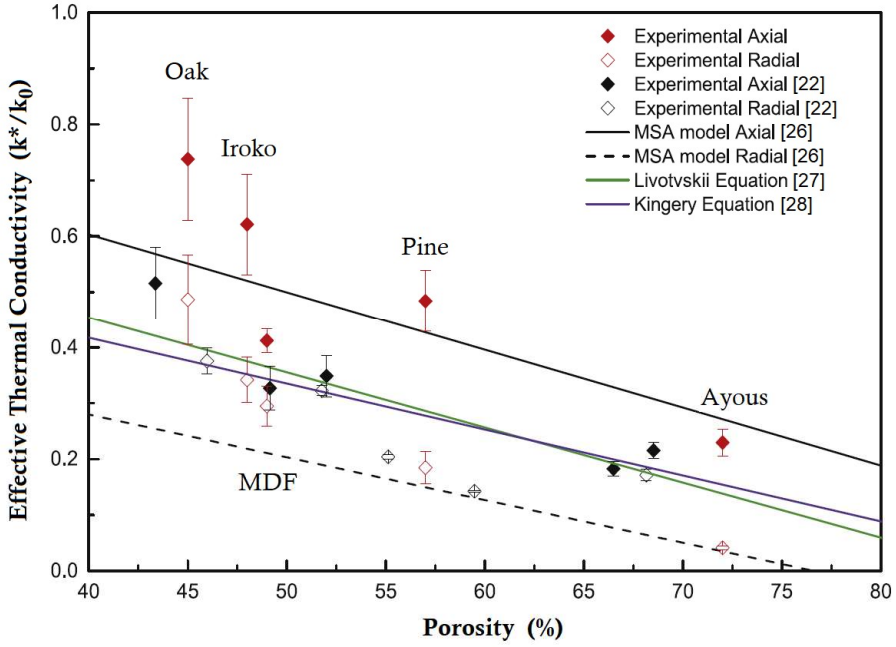

Figure 5.7. Effective thermal conductivity of the bioSiC samples as a function of porosity. Comparison between experimental values from this work and analytical predictions from different models [30]

It is clear from Figure 5.7 that there are large discrepancies between thermal conductivities predicted by the three models. The experimental values are significantly higher than the calculated ones. The predicted curves based on the MSA model under-estimates the experimental thermal conductivity as a function of porosity. Consistently, measured thermal conductivities are higher than those predicted by the MSA model in all cases, and the difference is larger at lower porosities.

The differences between experimental values and the theoretical values are attributed to the fact that the thermal conductivity of a two-phase system depends not only on the amount of porosity but also on the pore shape and distribution. Deviations on the experimental values with respect to the different models could be due that bioSiC samples exhibit a complex and multimodal pore size distribution, as it has been observed by mercury porosimetry (see Figure 4.6 in Chapter 4). Since pore geometry also varies with the choice of wood precursor, a model that describes an ideal pore morphology might not be adequate for describing the range of microstructures that these materials exhibit [30].

In this work, higher thermal conductivity values than those previously reported in the literature have been found for comparable values of porosity. By comparison, Pappacena et al. [22] measured thermal conductivity values of up to 42 $W \cdot m^{-1}K^{-1}$ for 65 vol% of porosity, and 19 $W \cdot m^{-1}K^{-1}$ for 69 vol% of porosity at room temperature, for bioSiC samples made from beech, mahogany, poplar, sapele and red oak woods. In their work, chemical etching for 1–2 weeks was used to remove the residual silicon, in contrast to capillary extraction and evaporation used in this work. The difference between the values of thermal conductivity may be due to this differences in processing. For very long etching times, the residual Si at the SiC grain boundaries might have been eliminated, leading to a loss in grain connectivity that further lowers thermal conductivity of bioSiC samples [31]. Although the values in this paper are higher than those reported previously, thermal conductivity values show the same influence with porosity, temperature and orientation [30].

Other important parameter that can play a significant role in the thermal conductivity is the grain size of SiC and the density and nature of grain boundaries [29]. The values of thermal conductivity in SiC were found to increase with the grain size due to a lower density of phonon-scattering boundaries. When bioSiC samples were heat-treated up to 1800 °C to remove the remnant silicon, the grain size could have increased with the temperature, increasing connectivity in the SiC grains and enhancing the conductivity compared to samples that were made by acid etching. The higher thermal conductivity of bioSiC samples from this work may well be due to the grain characteristics in comparison to biomorphic silicon carbide processed by chemical etching; our samples show a highly percolated structure with a lower density of grain boundaries [30].

Anisotropy of the thermal conductivity

It is interesting to highlight the effect of the anisotropy of bioSiC in the thermal conductivity values. BioSiC samples are formed by a SiC scaffold and a pore region, and is important to know

how both phases are distributed, if the pores are aligned in the direction parallel to the direction of heat flow, or conversely, the pores are aligned perpendicular to the direction of flow.

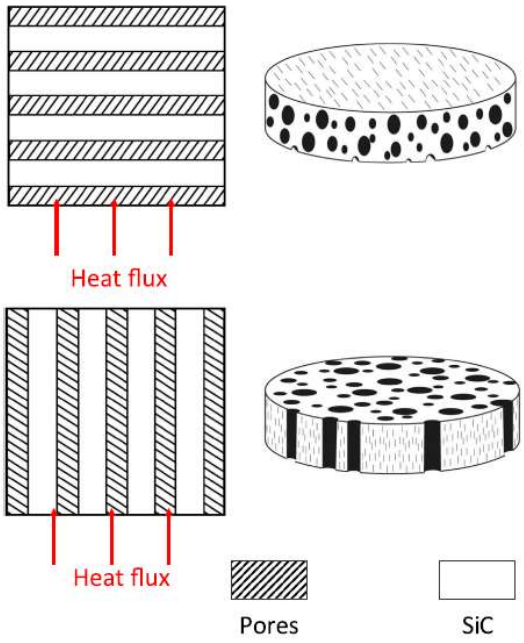

Figure 5.8. Schematic depiction of the relation between heat flux direction and microstructure in: a) radial and b) axial orientations [30]

The variation between axial and radial experimental thermal conductivities as a function of temperature was observed in Figure 4.10. The thermal conductivity of the bioSiC samples measured in the axial orientation shows higher values than measurements in the radial orientations. It can be seen that the thermal conductivity of radial samples is about a 30–82% lower than that of axial samples depending on the total porosity, as has been previously reported by Parfen'eva et al. [32]; and although the temperature increases, the anisotropy coefficient β (k_{axial}/k_{radial}) tends to be of the same order of magnitude for each wood precursor (Table 5.3).

Table 5.3. Anisotropy coefficient ($\beta = k_{axial}/k_{radial}$) of the bioSiC samples at room temperature and 700 °C

	Anisotropy coefficient	
Sample	**Ambient temperature**	**700 ºC**
Ayous	5.75	5.03
Pine	2.42	2.67
Iroko	1.88	1.72
Oak	1.47	1.57
MDF	1.26	1.51

These values also depend on the microstructure and pore size distribution. Iroko, Oak and MDF bioSiC samples show less variation in thermal conductivity values with the direction of heat flux because of the more regular and homogeneous microstructure of the wood precursor. These values as a function of orientation correspond well with the concept illustrated in Figure 5.8. In the axial orientation, there are direct heat pathways through the dense solid silicon carbide scaffold and the heat flux could travel through the solid phase parallel to the direction of the channels (pores). In contrast, in the radial direction where the direction of heat flow is perpendicular to the pores, the conductive large regions are in series, leading to a lower overall thermal conductivity [30].

5.5. Mechanical strength dependency on density

In Section 4.2.3 of the previous Chapter, the measured values of the maximum compressive strength were presented (see Table 4.5). Through the following graphs, the dependency of the compressive strength on the density has been analysed. The reported maximum compressive strength was the average of a minimum of five measurements for each wood-bioSiC and loading conditions in both directions (axial and radial). Error bars represent one standard deviation [10].

In Figure 5.9A a comparison of maximum compressive strengths as a function of density is provided for each wood-derived SiC specimen for the two different orientations. As can be seen from Table 4.5 and Figure 5.9A, compressive strengths are in the range ~3–115 MPa, showing a dependence on density and orientation of the wood precursor. In both directions, the values approximate a potential relationship with the relative density. The values decrease significantly with decreasing density of the samples, in direct relation to the porosity fraction. This result agrees with findings in previous works [31,33,34], in which the mechanical strength of these ceramic samples depended on density. Consequently, greater pore volume gradually diminished the mechanical strength. MDF-derived bioSiC presents a higher compressive strength; measured values were higher than expected in relation to their density because some fibres could be oriented in the direction of maximum compressive load, which yielded a higher compressive strength [35].

In Figure 5.9B the relative strength data ($\sigma_{bioSiC}/\sigma_{SiC}$) is plotted as a function of the relative density that determines the SiC volume fraction (ρ_{bioSiC}/ρ_{SiC}). These factors may be related to a potential dependence according to the following equation given by the model of Gibson and Ashby [36]:

$$\frac{\sigma_{bioSiC}}{\sigma_{SiC}} = \left(\frac{\rho_{bioSiC}}{\rho_{SiC}}\right)^{n} \qquad \text{Eq. 5.24}$$

where σ_{bioSiC} and ρ_{bioSiC} are the strength and the bulk density of the porous solid (bioSiC), σ_{SiC} and ρ_{SiC} are the strength and the density of a fully dense SiC monolith, and n is a geometric exponent which depends on the microstructure and loading direction. Values of compressive strength (3.9 GPa) and theoretical density of fully dense SiC (3.21 g/cm^3) were taken from the

literature [29,37]. Since the exponent n is derived from the fitting of log-log plots, its calculation does not depend on the actual numerical values assigned to the bulk properties of the solid phase. Due to the porosity of the material, the values found here were much lower than the strength for the fully dense material.

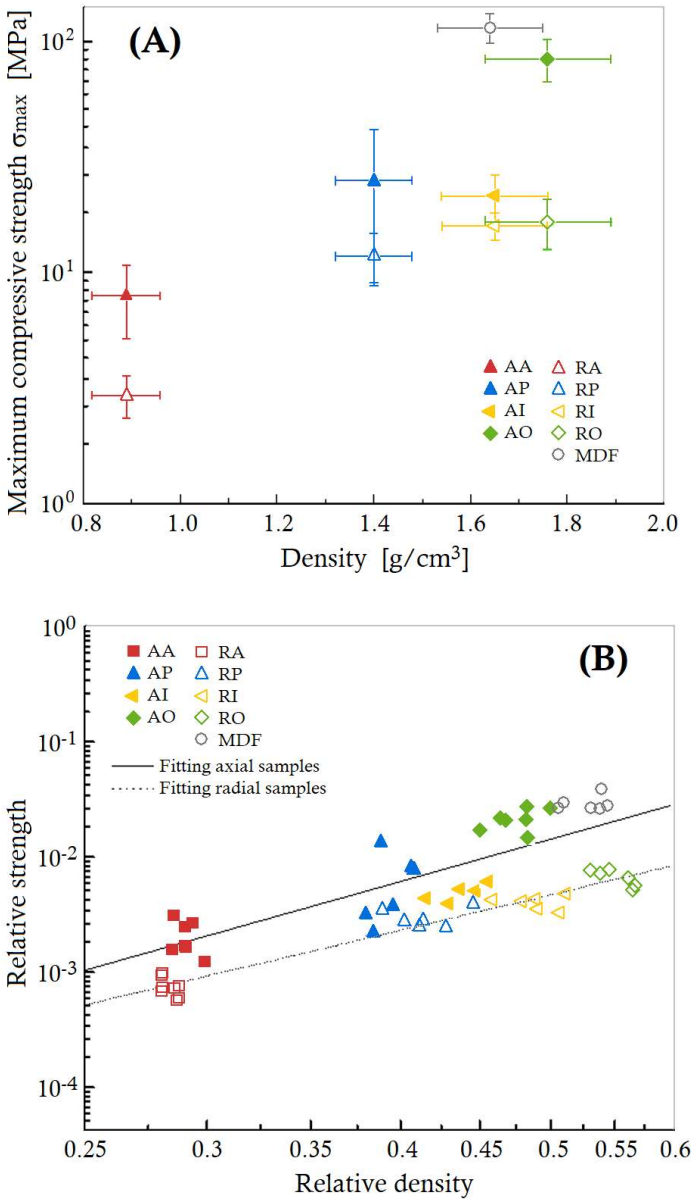

Figure 5.9. (A) Maximum compressive strength at room temperature as a function of density and (B) relative strength as a function of relative density of the bioSiC specimens

The exponent was higher than predicted by the model (3.78 for axial samples and 3.19 for radial samples), but consistent with previous works confirming that this model results in an overestimation when applied to porous bioSiC samples derived from wood [34,37]. Since MDF samples performed more like axial samples than radial samples, the geometric exponent n was determined by fitting the values of radial samples without considering the results of MDF.

5.6. Applicability as filter material

Filter materials are selected according to pore structure and microstructural parameters [38]. Small pore sizes and low volume fractions of porosity enhance filtration efficiency and the mechanical stability of the samples, while at the same time increase the pressure drop in the filter with the gas flow. Consequently, a trade-off needs to be found between filtration efficiency and pressure drop.

Pore volume in most commercial filters is within the range of 40– 50% or exceptionally 60% [39]. Furthermore, typically a well-defined monomodal pore distribution is sought for improving particle-filtration efficiency and filter selectivity [39,40]. Therefore, ceramic filter substrates normally present pore volumes of about 50% and average pore sizes of 10 μm. Regarding the five precursors used in this work, the level of porosity was controlled by selecting a wood precursor. Ayous, Oak and Iroko showed a multimodal pore-size distribution with larger pores up to hundreds of micrometers. In this way, Pine and MDF had more desirable characteristics, because of their narrower and more homogeneous pore distributions.

From the knowledge of the influence of microstructure on permeability values, it is possible to estimate the pressure drop originated in a filter under a given flow rate. Innocentini et al. [41] have classified a wide range of porous materials according to permeability parameters.

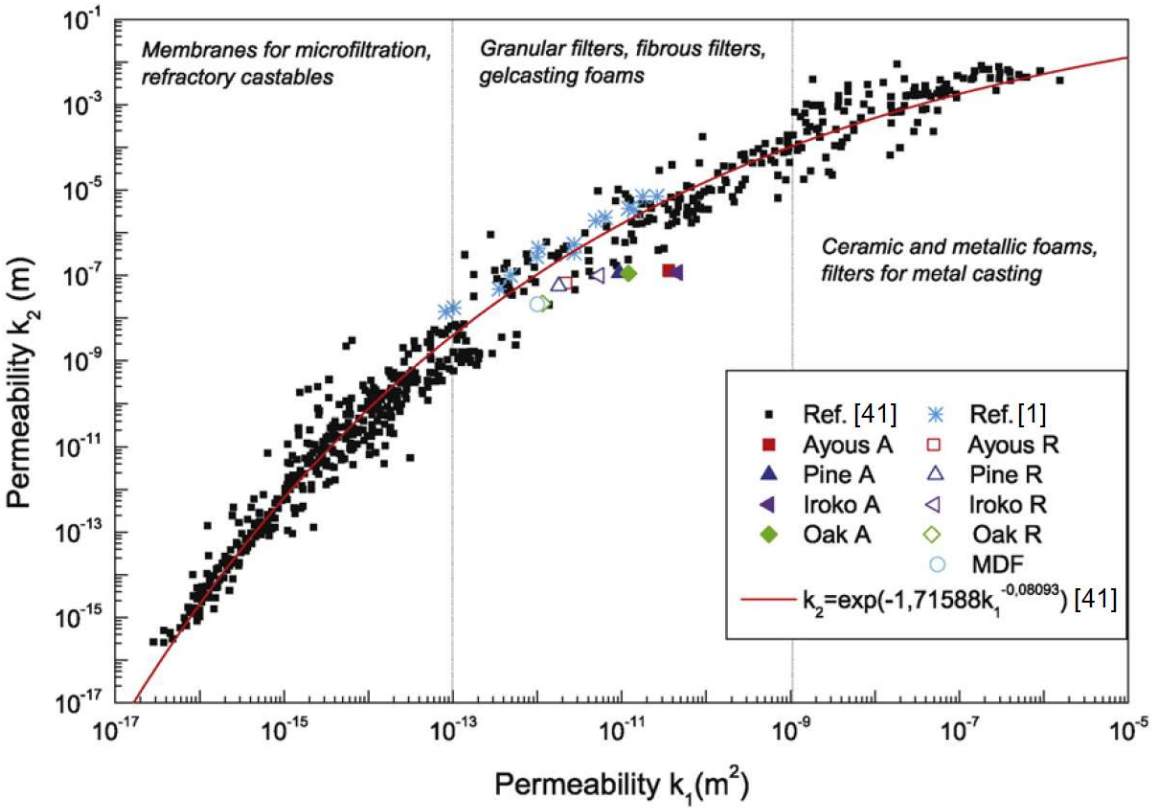

Figure 5.10. Classification of filter materials according to permeability values from the literature [41] including experimental data from this work [10]

In Figure 5.10 an adapted version of the map from the studies of Innocentini et al. is presented including all the results found in the present work for bioSiC materials, the results for other filter ceramics of cordierite bonded porous SiC for comparison purposes [1] and the exponential fit $\left[k_2 = \exp(-1.71588{k_1}^{-0.08093})\right]$ that relates permeability parameters of a variety of porous media. Permeability of porous bioSiC materials were located according to the classification in the typical range for granular and fibrous filters, which normally present Darcian permeabilities in the range 10^{-9}–10^{-13} m^2. For axial samples, permeability values deviated slightly from the general trend and were generally higher than other values reported in the literature for commercial granular filters because of the presence of interconnected larger pores with preferred orientation [10].

Alonso-Fariñas et al. [42] and Bautista et al. [35] assessed the feasibility of porous MDF-derived bioSiC as high-temperature filters in gasification plants with permeability values of 10^{-13} m^2 for porosities ranging from 40–60%, and with a filtration efficiency higher than 98%. In ceramic materials used as diesel particulate filters, permeability typically ranges from 10^{-12} to 10^{-9} [39]. Eom et al. [43] reported permeability values of macroporous SiC ceramics on the order of 10^{-12}–10^{-13} m^2 with porosities of 50–60%. For a volume of porosity of 75%, Song et al. [44] reported permeability values in the range of 10^{-13} m^2 and Yan et al. [8] reported values in the range of 10^{-12} m^2 on porous cordierite-mullite ceramic samples with porosity of 40–50%. According to the map in Figure 5.10, and permeability values of commercial filters, bioSiC seems to be a promising material for filtering applications.

In terms of mechanical stability, all samples have enough strength not to fail during filtration applications despite their high porosities. Nevertheless, Ayous-bioSiC showed notably poor mechanical stability as a consequence of the high porosity-volume fraction and may not be a suitable precursor for filter applications.

5.7. Economic considerations

Availability for mass production at low prices and low weight is a prerequisite for automotive applications. Compared to other popular DPFs substrates like cordierite or aluminium titanate, silicon carbide turns out to be relatively expensive [39]. This difference is due to the high sintering temperatures of silicon carbide, and the high price of its raw materials [45].

- The traditional fabrication route for extruded ceramic monoliths involves two main processes: extrusion moulding and sintering. The first one is relatively easy and cheap, but sintering requires very high temperatures. The sintering temperature depends on the material. To sinter silicon carbide temperatures above 1600 °C are needed. Cordierite for instance require lower sintering temperatures.
- On the other hand, the raw materials needed to make silicon carbide monoliths are: SiC powders and a binder material. The binder material can be starch, which is cheap, but the SiC powders are expensive.

The manufacturing process of biomorphic silicon carbide differs totally from that of extruded ceramics. Unlike granular silicon carbide commercially used in DPFs, bioSiC cannot be manufactured from sludge by a sintering process. BioSiC is manufactured from the pyrolysis of wood blocks and it passes through different stages, but always in solid state. It requires mechanization instead of extrusion and different thermal processes. Consequently, the costs of a possible massive production may differ considerably.

In terms of raw material prices, the cost of bioSiC is similar to that of extruded SiC. The cost of the vegetal precursor is almost negligible, and the cost of silicon powder is in the same range than the cost of silicon carbide powder at industrial scale. BioSiC is considered an ecoceramic material because it can be made from wood wastes or renewable resources; and it does not need a high quality silicon powder for the reaction.

Regarding the thermal demand, the manufacturing process of bioSiC may have a different costs depending on the chosen procedure for removing the silicon in excess. The evaporation procedure proposed in this thesis requires higher temperatures, since the evaporation point of silicon must be exceeded. In that case the energy cost of producing bioSiC may be of the same order that the cost of producing sintered SiC. On the contrary, the silicon removal through chemical etching can be done at room temperature, so a significant cost reduction can be achieved.

5.8. Conclusions

In the previous chapter, the most representative properties of bioSiC as potential candidate for material substrate in automotive DPFs have been characterized and analysed by using small simple laboratory samples. The study began with a general characterization of its microstructural and physical properties, and finished with a specific study over filtration efficiency and permeability, as they are the parameters of the material most directly linked to the filtration performance. The characterization study was performed keeping in mind the final application which the material is intended to be used for, that is the application to Diesel Particulate Filters for automotive engines. In this sense, certain measurements such as porosity, pore size, or permeability, have been considered more relevant in the decision-making process. However, the characterization study has been quite exhaustive and from the author's point of view it may be useful for any future study of biomorphic SiC for any other application.

In this chapter a further analysis on the measurements previously presented has been done. Significant parameters of bioSiC from the point of view of filtration performance (permeability, thermal conductivity and compressive strength) have been correlated with microstructural features (pore size, porosity and density) to draw useful relationships and to predict the performance of any biomorphic substrate made from a different precursor for the considered application.

Average pore size, alignment of pores and tortuosity seemed to be the key factors in permeability results. For permeability prediction concerning microstructural parameters, an Ergun-type relationship was proposed where the equivalent pore size is determined by integration of the pore size distribution, although to different integration limits in the axial and radial directions to reflect the materials' anisotropy. The flow performance of the material was characterized by calculating the Forchheimer's number. We showed that in radial samples inertial effects were not as remarkable as in axial samples, but both terms of Forchheimer's equation must be considered for flow-regime prediction. On the other hand, compressive strength has been found to diminish with porosity, the resulting values being from 3 to 115 MPa.

Thermal conductivity values reveal a strong dependence on the porosity fraction. The thermal conductivity values of the most porous sample at room temperature are 22 and 5 $W \cdot m^{-1}K^{-1}$ depending on the direction of heat flux as a function of the direction of the pores, while for the less porous sample are 88 and 60 $W \cdot m^{-1}K^{-1}$. The experimental values were compared with the theoretical values from three analytical models proposed to describe the thermal conductivity of a porous material attending to pore size and fractional porosity. Experimental values are higher than predicted in the axial direction but agree reasonably with the predictions for the radial direction. However, in the more porous samples, the experimental values are close to the theoretical values calculated by the minimum solid area model.

All the results pointed to the possibility of tailoring these two properties by selecting a particular wood precursor and controlling the microstructural parameters of the final porous ceramics. With the control of these properties, the best optimum requirements for filtering applications of the end product may be fulfilled.

The performance of a bioSiC wall-flow DPF mainly depends on two factors: on the material features of the substrate, and on the geometrical design of the complete system. Chapters 4 and 5 were focused on presenting the results at the material level. In the following chapter, the results of the a more specific study considering the complete design of an MDF-bioSiC wall-flow DPF will be presented. It will include, not only the measurements of efficiency and pressure drop from the experimental campaign, but also the results of the numerical simulations and a further analysis comparing the performance of this bioSiC wall-flow DPF with that of other commercial DPFs.

References

[1] Dey A, Kayal N, Chakrabarti O, Caldato RF, André CM, de Mello Innocentini MD. Permeability and Nanoparticle Filtration Assessment of Cordierite-Bonded Porous SiC Ceramics. Ind Eng Chem Res 2013;52:18362–18372.

[2] Moreira EA, de Mello Innocentini MD, Coury JR. Permeability of ceramic foams to compressible and incompressible flow. J Eur Ceram Soc 2004;24:3209–18. doi:10.1016/j.jeurceramsoc.2003.11.014.

[3] Topates G, Petasch U, Adler J, Kara F, Mandal H. Production and permeability of porous

Si3N4 ceramics produced by starch addition. J Asian Ceram Soc 2013;1:257–61. doi:10.1016/j.jascer.2013.06.002.

[4] Topates G, Mammitzsch L, Petasch U, Adler J, Kara F, Mandal H. Microstructure–permeability relation of porous β-Si3N4 ceramics. J Eur Ceram Soc 2013;33:1545–51. doi:10.1016/j.jeurceramsoc.2012.12.022.

[5] Wang B, Zhang H, Phuong HT, Jin F, Yang JF, Ishizaki K. Gas permeability and adsorbability of the glass-bonded porous silicon carbide ceramics with controlled pore size. Ceram Int 2015;41:2279–85. doi:10.1016/j.ceramint.2014.10.032.

[6] Kumar A, Mohanta K, Kumar D, Parkash O. Low cost porous alumina with tailored gas permeability and mechanical properties prepared using rice husk and sucrose for filter applications. Microporous Mesoporous Mater 2015;213:48–58. doi:10.1016/j.micromeso.2015.04.004.

[7] Eom J-H, Kim Y-W, Song I-H, Kim H-D. Processing and properties of polysiloxane-derived porous silicon carbide ceramics using hollow microspheres as templates. J Eur Ceram Soc 2008;28:1029–35. doi:10.1016/j.jeurceramsoc.2007.09.009.

[8] Yan W, Li N, Li Y, Tong J, Luo H. Strength and gas permeability of porous cordierite-mullite ceramics with different phase compositions and microstructures prepared by a pore-forming in-situ technique. J Ceram Process Res 2013;14:109–13.

[9] de Mello Innocentini MD, Faleiros RK, Pisani Jr R, Thijs I, Luyten J, Mullens S. Permeability of porous gelcast scaffolds for bone tissue engineering. J Porous Mater 2010;17:615–27.

[10] Gómez-Martín A, Orihuela MP, Becerra-Villanueva JA, Martínez-Fernández J, Ramírez-Rico J. Permeability and mechanical integrity of porous biomorphic SiC ceramics for application as hot-gas filters. Mater Des 2016;107:450–60. doi:10.1016/j.matdes.2016.06.060.

[11] Ergun S, Orning AA. Fluid Flow through Randomly Packed Columns and Fluidized Beds. Ind Eng Chem 1949;41:1179–84.

[12] Biasetto L, Colombo P, de Mello Innocentini MD, Mullens S. Gas Permeability of Microcellular Ceramic Foams. Ind Eng Chem Res 2007;46:3366–72.

[13] Macdonald IF, El-Sayed MS, Mow K, Dullien FAL. Flow through Porous Media-the Ergun Equation Revisited. Ind Eng Chem Fundam 1979;18:199–208.

[14] Dey A, Kayal N, Chakrabarti O, Caldato RF, de Mello Innocentini MD, Guerra VG. Investigations on Material and Mechanical Properties, Air-Permeation Behavior and Filtration Performance of Mullite-Bonded Porous SiC Ceramics. Int J Appl Ceram Technol 2014;11:804–16.

[15] Isobe T, Kameshima Y, Nakajima A, Okada K, Hotta Y. Gas permeability and mechanical properties of porous alumina ceramics with unidirectionally aligned pores. J Eur Ceram Soc 2007;27:53–9.

[16] Richardson JT, Peng Y, Remue D. Properties of ceramic foam catalyst supports: pressure drop. Appl Catal A Gen 2000;204:19–32.

[17] Gibson LJ, Ashby MF. Cellular Solids - Structures & Properties. Cambridge University Press; 1999.

[18] Orihuela MP, Gómez-Martín A, Becerra-Villanueva JA, Chacartegui R, Ramírez-Rico J.

Performance of biomorphic silicon carbide as particulate filter in diesel boilers. J Environ Manage 2017;203:907–19. doi:10.1016/j.jenvman.2017.05.003.

[19] Ma H, Ruth DW. The microscopic analysis of high forchheimer number flow in porous media. Transp Porous Media 1993;13:139–60.

[20] de Mello Innocentini MD, Lefebvre LP, Meloni RV, Baril E. Influence of sample thickness and measurement set-up on the experimental evaluation of permeability of metallic foams. J Porous Mater 2010;17:491–9.

[21] Najmi H, El-tabach E, Chetehouna K, Gascoin N, Falempin F. Effect of flow configuration on Darcian and Forchheimer permeabilities determination in a porous composite tube. Int J Hydrogen Energy 2016;41:316–23. doi:10.1016/j.ijhydene.2015.10.054.

[22] Pappacena KE, Faber KT, Wang H, Porter WD. Thermal conductivity of porous silicon carbide derived from wood precursors. J Am Ceram Soc 2007;90:2855–62. doi:10.1111/j.1551-2916.2007.01777.x.

[23] Elliott SR. The Physics and Chemistry of Solids. Chichester, United Kingdom: John Wiley & Sons; 1998.

[24] Yang B-K, Sakka Y. Thermophysical properties of porous SiC ceramics fabricated by pressureless sintering. Sci Technol Adv Mater 2007;8:655–9.

[25] Eom J-H, Kim Y-W, Raju S. Processing and properties of macroporous silicon carbide ceramics: A review. J Asian Ceram Soc 2013;1:220–42.

[26] Rice RW. Porosity of Ceramics: Properties and Applications. 1998.

[27] Parfen'eva LS, Orlova TS, Kartenko NF, Sharenkova N V., Smirnov BI, Smirnov IA, et al. Thermal conductivity of high-porosity cellular-pore biocarbon prepared from sapele wood. Phys Solid State 2009;51:2023–31. doi:10.1134/S1063783412080240.

[28] Kingery WD, Bowen HK, Uhlmann DR. Introduction to Ceramics, 2nd Edition. New York: Wiley; 1976.

[29] Snead LL, Nozawa T, Katoh Y, Byun T, Kondo S, Petti DA. Handbook of SiC properties for fuel performance modeling. J Nucl Mater 2007;371:329–77. doi:10.1016/j.jnucmat. 2007.05.016.

[30] Gómez-Martín A, Orihuela MP, Ramírez-Rico J, Chacartegui R, Martínez-Fernández J. Thermal conductivity of porous biomorphic SiC derived from wood precursors. Ceram Int 2016;42:16220–9. doi:10.1016/j.ceramint.2016.07.151.

[31] Torres-Raya C, Hernandez-Maldonado D, Ramírez-Rico J, García-Gañán C, De Arellano-López AR, Martínez-Fernández J. Fabrication, chemical etching, and compressive strength of porous biomimetic SiC for medical implants. J Mater Res 2008;23:3247–54. doi:10.1557/JMR.2008.0392.

[32] Parfen'eva LS, Orlova TS, Smirnov IA, Misiorek H, Mucha J, Jezowski A, et al. Anisotropy of the thermal conductivity and electrical resistivity of the SiC/Si biomorphic composite based on a white-eucalyptus biocarbon template. Phys Solid State 2006;48:2281–8.

[33] Presas M, Pastor JY, LLorca J, De Arellano-López AR, Martínez-Fernández J, Sepúlveda RE. Mechanical behavior of biomorphic Si/SiC porous composites. Scr Mater 2005;53:1175–80. doi:10.1016/j.scriptamat.2005.07.033.

[34] Kaul VS, Faber KT, Sepúlveda R, De Arellano-López AR, Martínez-Fernández J.

Precursor selection and its role in the mechanical properties of porous SiC derived from wood. Mater Sci Eng A 2006;428:225–32. doi:10.1016/j.msea.2006.05.033.

[35] Bautista MA, Cancapa JQ, Martínez-Fernández J, Rodríguez MA, Singh M. Microstructural and mechanical evaluation of porous biomorphic silicon carbide for high temperature filtering applications. J Eur Ceram Soc 2011;31:1325–32. doi:10.1016/j.jeurceramsoc.2010.06.014.

[36] Gibson LJ, Ashby MF. Celullar Solids - Structure & Properties. Cambridge University Press; 1998.

[37] Varela-Feria FM, Martínez-Fernández J, De Arellano-López AR, Singh M. Low density biomorphic silicon carbide: microstructure and mechanical properties. J Eur Ceram Soc 2002;22:2719–25.

[38] Tandon P, Heibel A, Whitmore J, Kekre N, Chithapragada K. Measurement and prediction of filtration efficiency evolution of soot loaded diesel particulate filters. Chem Eng Sci 2010;65:4751–60. doi:10.1016/j.ces.2010.05.020.

[39] Adler J. Ceramic Diesel Particulate Filters. Int J Appl Ceram Technol 2005;2:429–39. doi:10.1016/B978-0-12-385469-8.00032-0.

[40] Kittelson DB. Engines and nanoparticles: A review. J Aerosol Sci 1998;29:575–88. doi:10.1016/S0021-8502(97)10037-4.

[41] de Mello Innocentini MD, Sepulveda P, dos Santos Ortega F. Permeability. Cell. Ceram. Struct. Manuf. Prop. Appl., 2006, p. 313–41.

[42] Alonso-Fariñas B, Lupion M, Rodríguez-Galán M, Martínez-Fernández J. New candle prototype for hot gas filtration industrial applications. Fuel 2013;114:120–7. doi:10.1016/j.fuel.2012.12.054.

[43] Eom J-H, Kim Y-W, Song I-H. Effects of the initial α-SiC content on the microstructure, mechanical properties, and permeability of macroporous silicon carbide ceramics. J Eur Ceram Soc 2012;32:1283–90.

[44] Song I-H, Kwon I-M, Kim H-D, Kim Y-W. Processing of microcellular silicon carbide ceramics with a duplex pore structure. J Eur Ceram Soc 2010;30:2671–6.

[45] Konstandopoulos AG. Technology Evaluation Report for Diesel Engine After-Treatment System. 2013.

Chapter 6
Filtration performance of wall-flow MDF-bioSiC DPFs

In chapters 4 and 5, the microstructural and physical properties of nine different bioSiC specimens were presented and analysed. The characterization study was performed keeping in mind the final application which the material is intended to be used for, that is the application to Diesel Particulate Filters for automotive engines. In this sense, more attention was paid to some properties such as the porosity, the pore size, or the permeability, since they are known to have more influence in the suitable filtration performance of the material. These properties carried greater weight in the decision-making process regarding the precursor selection for the wall-flow DPF prototype. However, the characterization study has been quite exhaustive and, from the author's point of view, the results can be useful and extrapolated to the use of biomorphic SiC in other applications.

Chapter 6 is focused on the results of the experimental campaigns with the MDF-bioSiC wall-flow DPF prototypes, and provides both empirical and numerical results of the filtration performance of the filters under real operating conditions. It has two main sections. In Section 6.2 the results of the experimental campaign with the bioSiC wall-flow prototypes are presented. First, all the preliminary tests and considerations are presented, and then the main results of these tests are presented, focused on filtration efficiency and pressure drop. After that, Section 5.3 presents the results of the numerical simulations described in Section 3.6. First, evidence of the validation is provided; and then, the results of the simulation of the real-scale bioSiC DPF under real driving conditions are presented. In the final section, a summary of the main results and conclusions is provided.

Related publications

1. M.P. Orihuela, A. Gómez-Martín, P. Miceli, J.A. Becerra-Villanueva, R. Chacartegui, D. Fino. *Experimental measurement of the filtration efficiency and pressure drop of wall-flow Diesel Particulate Filters (DPF) made of biomorphic Silicon Carbide using laboratory generated particles.* Applied Thermal Engineering, Vol. 131, 41-53, 2018.
   doi: 10.1016/j.applthermaleng.2017.11.149

2. M.P. Orihuela, F. Shikh Anuar, I. Ashtiani Abdi, M. Odabaee, K. Hooman. *Thermohydraulics of a metal foam-filled annulus*. International Journal of Heat and Mass Transfer, Vol. 117, 95-106, 2018.
   doi: 10.1016/j.ijheatmasstransfer.2017.10.009
3. M.P. Orihuela, O. Haralampous, R. Chacartegui, J. Martínez. *Numerical simulation of a wall-flow Diesel Particulate Filter made of biomorphic Silicon Carbide*. SAE international (under review)

6.1. Introduction

An ideal DPF for automotive applications must have some specific characteristics: it must be considerably porous in order to prevent dangerous back pressures; it must act as a heat sink in order to keep heat during low loads; and it must be resistant to thermal shocks as the one that takes place during the regeneration process. All these aspects can be represented by two physical entities: Specific Heat (C_p) and Thermal Shock Resistance (TSR). Silicon Carbide is known to have higher thermal conductivity and tensile strength than Cordierite. In particular, recrystallized Silicon Carbide (Re-SiC) and all those technologies able to achieve high porosity, are able to stand more porosities than cordierite without affecting its thermal performances [1]. However, its high coefficient of thermal expansion (CTE) usually affects negatively its TSR [2,3].

Table 6.1. Thermal and mechanical properties of the bioSiC samples (evaluated at ambient temperature) affecting its thermal shock performance

Sample		**Specific heat** [4] **(J/kg K)**	**Thermal conductivity** [5] **(W/m K)**	**Maximum tensile strength** [6] **(MPa)**	**Thermal expansion coefficient (K^{-1})**	**Young modulus** [7] **(GPa)**	**Poisson ratio** [6]
Ayous	Axial	671.28	26	45	$1.5 \cdot 10^{-6}$	178	0.15
	Radial	671.28	4.4	45	$1.5 \cdot 10^{-6}$	178	0.15
Pine	Axial	671.28	55	45	$1.2 \cdot 10^{-6}$	214	0.15
	Radial	671.28	23	45	$1.2 \cdot 10^{-6}$	214	0.15
Iroko	Axial	671.28	74	79	$2 \cdot 10^{-6}$	214	0.15
	Radial	671.28	39	79	$2 \cdot 10^{-6}$	214	0.15
Oak	Axial	671.28	88	79	$1.5 \cdot 10^{-6}$	250	0.15
	Radial	671.28	60	79	$1.5 \cdot 10^{-6}$	250	0.15
MDF	Axial	671.28	43	79	$1.5 \cdot 10^{-6}$	270	0.15
	Radial	671.28	34	79	$1.5 \cdot 10^{-6}$	270	0.15

Table 6.1 presents a summary of the main thermal and mechanical properties of bioSiC from different precursors affecting its behaviour against thermal shock. Values have been extracted searching in the literature and, in some cases, they are only approximated. The CTE was experimentally measured and turns out to be lower than the typical CTE of a standard SiC [4]. Gathering these representative values of thermal conductivity [5], tensile strength [6], Young

modulus [7], and Poisson ratio [6] of bioSiC, an estimation of the TSR can be made. Figure 6.1 shows a simplified Ashby chart where the estimated values of C_p and TSR (for ΔT=650-100=550°C) of bioSiC are presented, compared to those of other commercial ceramics.

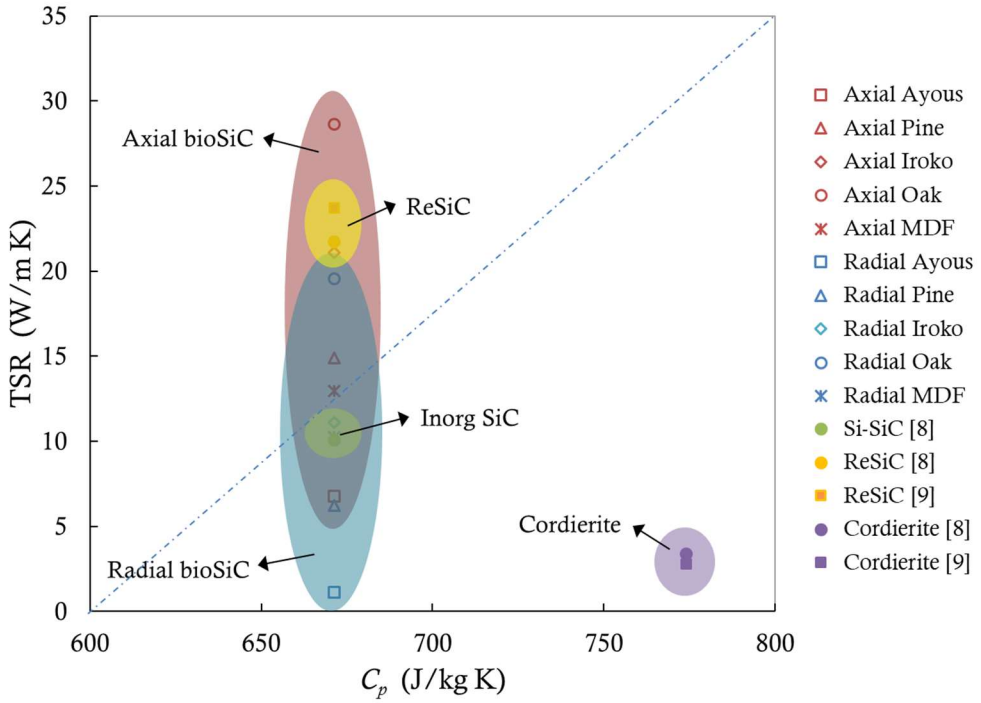

Figure 6.1. Estimated Thermal Shock Resistance and Specific Heat of bioSiC ceramics compared to other commercial ceramics [8,9]

Although scattered, estimated bioSiC TSR values compete with those of commercial ceramics and present promising values specially for bioSiC generated from axial precursors.

6.2. Experimental results with the bioSiC DPF prototypes

As described in Section 3.5, to perform the filtration tests a synthetic SG was used. Each prototype was subject to three filtration tests and regenerated after each one to remove the deposited soot and start over again with the clean filter. Tests were performed under controlled and reproducible conditions, with a fixed gas flow rate of 5 LPM and a soot mass flow rate of 4 mg/h.

6.2.1. Preliminary blank tests

Before starting the filtration tests, two previous blank tests were needed in order to: (i) determine the permeability of MDF-bioSiC in the direction perpendicular to the compression one, and (ii) to determine the pressure drop caused by other elements different from the filter along the canning (cordierite holder and thermocouple guides mainly).

Permeability of MDF-bioSiC in the direction perpendicular to the compression one

The first test was performed setting different air flow rates, from 1 LPM to 14 LPM, through the sample and measuring the pressure drop in each case. The air flow velocity v was determined dividing the imposed flow rate Q by the total cross section for the air (the total internal surface of the inlet channels). The pressure drop per unit length ($\Delta P/L$) depends on the velocity v following the quadratic trend that the well-known Darcy's law with Forchheimer's extension [10] describes (Eq. 6.1). Therefore, calculating the quadratic fitting curve, both the Darcian permeability and the inertial one can be obtained.

$$\frac{\Delta P}{L} = \frac{\eta}{k_1} v + \frac{\rho}{k_2} v^2 \qquad \text{Eq. 6.1}$$

The results of this test revealed that the Darcian permeability of MDF-bioSiC in the direction perpendicular to the compression one is $k_1 = 3.96 \cdot 10^{-14}\ m^2$, and the inertial permeability $k_2 = 1.32 \cdot 10^{-1}\ \ m$. These values are around two orders of magnitude lower than the values reported by Gómez-Martín et al. [11] for other bioSiC samples, and in particular for the MDF-bioSiC with the gas flowing in the compression direction. This fact indicates that a change on the relative orientation of the flux respect to the fibre may produce a lower pressure drop than the one reported in this study.

Pressure drop caused by other elements different from the filter along the canning

The second blank test was performed placing the canning in the test rig without the bioSiC prototype but with all the auxiliary elements: the cordierite holder with the vermiculite mop and the Castable Refractary Alumina sealing layer, and the two guides for the thermocouples. As in the previous test, different air flow rates were set, from 1 LPM to 14 LPM, and the pressure drop was measured. The experimental data show a linear dependency between the pressure drop and the flow rate. For 5 LPM, the most used flow rate in this study, the pressure drop of the system turns out to be 41.9 mbar. This value was subtracted later from all the pressure drop data obtained in this work.

6.2.2. Characterization of the soot generator

The wall-flow MDF-bioSiC filters analysed in this study have been designed as an aftertreatment system for automotive diesel engines. The use of laboratory generated soot particles guarantees the repeatability of the experiment and provides with constant operating conditions. However, the applicability of the results of this study depends on the similarity between the particle size distribution of the SG and that of a real modern engine. For that reason, the first stage of the experimental campaign was to characterize the production of soot particles of the SG. By setting the previously mentioned operating parameters on the SG (5 LPM of argon and 4 mg/h of soot mass flow rate), and bypassing the particle laden stream directly to the measuring area with the SMPS and the CPC, the concentration and the particle size distribution of the SG was measured.

In order to reduce the uncertainty and secure reliable data, 4 sets of measurements were made over 20-minutes periods (10 scans 135 s long), and the average was considered as the result.

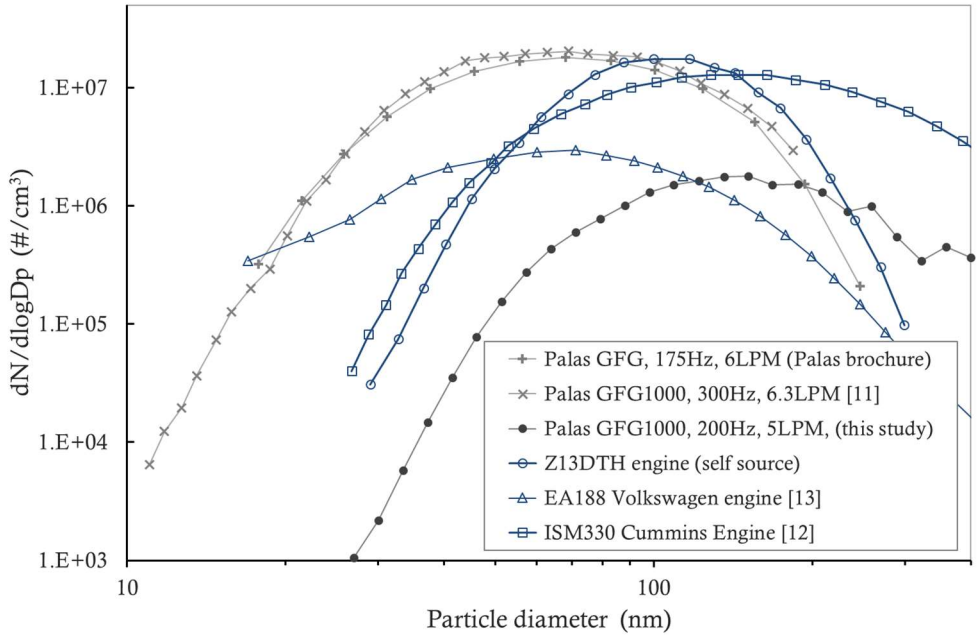

Figure 6.2. Normalized particle size distribution of the soot generator Palas GFG 1000 and comparison with the distribution in the exhaust of different engines [12]

The resulting normalized particle distribution is presented in Figure 6.2 versus the particle diameter with black filled dots. As a reference, the characteristic curves of the same SG (Palas GFG 1000) for different flow rates and spark frequencies are presented; one of them extracted from the technical brochure of the equipment, and the other one from the study carried out by Roth et al. [13]. In the same graph (Figure 6.2), three particle size distribution curves from three different diesel engines are also presented: one belonging to the Dipartimento di Scienza Applicata e Tecnologia (DISAT) of the Polytechnic of Turin, and two other diesel engines that have been taken from the literature. The curve obtained from [14] corresponds to a 6-cylinder 10.8 L heavy-duty engine, and the curve obtained from [15] corresponds to a 4-cylinder 2 L engine. In all the cases, the data correspond to the particle concentration just after the engine, before the filtering system.

The soot production of real engines may present a high variability depending on the size and the operating conditions. Statistically, a large part of the curves found in the literature for light-duty diesel engines present the peak at around 60-80 nm. The SG is able to produce particles concentrations similar to those of a real engine but with the advantage of doing it through a controlled process with higher precision than a running engine where many other parameters may also affect. The argon volume flow rate and the spark frequency were chosen in this study according to the dimensions of the filter samples. As a result, the peak concentration of particles is lower than the one that can be obtained in other conditions, but still not far from the production of particles of a real engine considering the logarithmic scale of the curves. The main difference between the production of particles with the SG and the production of particles of an engine is

the peak mobility diameter. The peak mobility diameter of a modern diesel engine is around 30 nm, whilst the SG used for this study produces generally bigger agglomerates with peak mobility diameters hardly lower than 60 nm. The Differential Mobility Analyzer of the SMPS allows to measure particles in the size range of 10 to 1000 nm, which covers almost the complete range of particles sizes of an engine and of the SG. Nevertheless, the production of particles lower than 20 nm is so low with the SG, that the uncertainty in the calculations for this range (D_p < 20 nm) is too high.

6.2.3. Filtration efficiency

One of the main objectives of this work of characterization of the manufactured MDF-bioSiC wall-flow filters is to determine their filtration efficiency. The filtration efficiency of a filter can be calculated as the ratio between the number concentration of soot particles deposited inside the filter and the number concentration that it has to face at the inlet (Eq. 6.2):

$$\eta_N = \frac{N_{in} - N_{out}}{N_{in}} \qquad \text{Eq. 6.2}$$

In each moment of the filtration process, Eq. 6.2 allows us to calculate the transient efficiency of the tested filter.

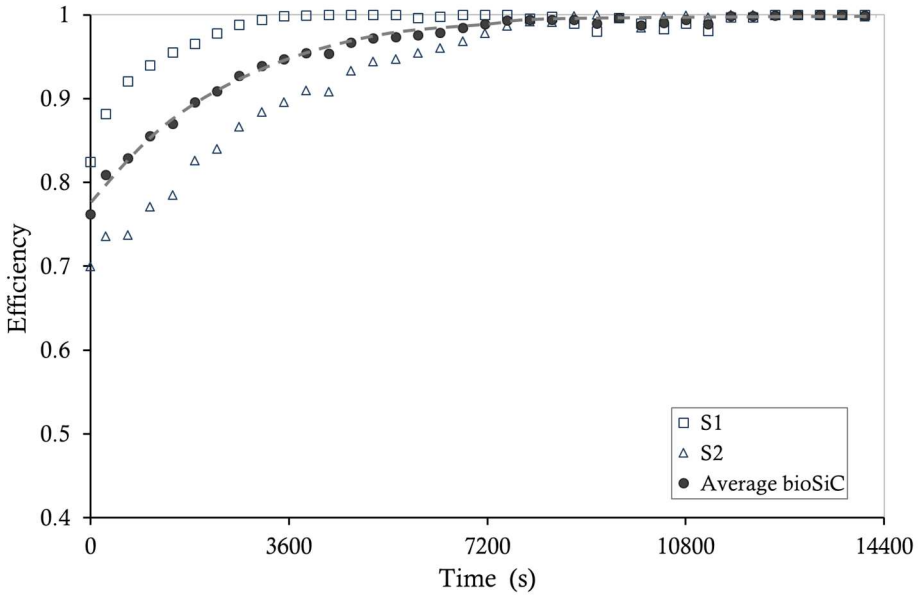

Figure 6.3. Filtration efficiency of the wall-flow bioSiC DPF prototypes

The resulting transient filtration efficiency of both prototypes (S1 and S2) is presented in Figure 6.3. For the clean filter (time = 0) a filtration efficiency of 77% has been found; and after two hours of soot loading, the filtration efficiency reaches in any case values around 100%. In this figure can be appreciated that there is a difference over 18% in the experimental efficiency between S1 and S2 despite the fact that both of them are supposed to come from the same precursor and to be equally manufactured. As will be shown later in the text, the difference in pressure drop is also significant, but not as high as it is in the case of efficiency. Therefore, these

differences may be partly caused by a variation in the permeability of the material, but more probably by a different porosity distribution and the inaccuracies in the hand-made manufacturing process [12].

Eq. 6.2 is also applicable for separated particle sizes ranges, which is useful to determine the filtration efficiency of the substrate as a function of the particle diameter. Figure 6.4 shows this dependency for both samples S1 and S2 in two different moments of the test: the initial moment and after 30 minutes of soot loading. In general, an increase in the efficiency with the particle diameter can be observed, which reveals the higher weight of the interception mechanism against the diffusion one in the filtration phenomenon for the diameter ranges measured in this study. Actually, the theoretical curve of filtration efficiency versus particle diameter presents an asymptotical behaviour also for small particles (horizontal asymptote: $\eta_N = 1$), and a minimum value of efficiency for particles sizes in the range between 50 nm and 300 nm depending on the characteristics of the filter and the flow [16,17].

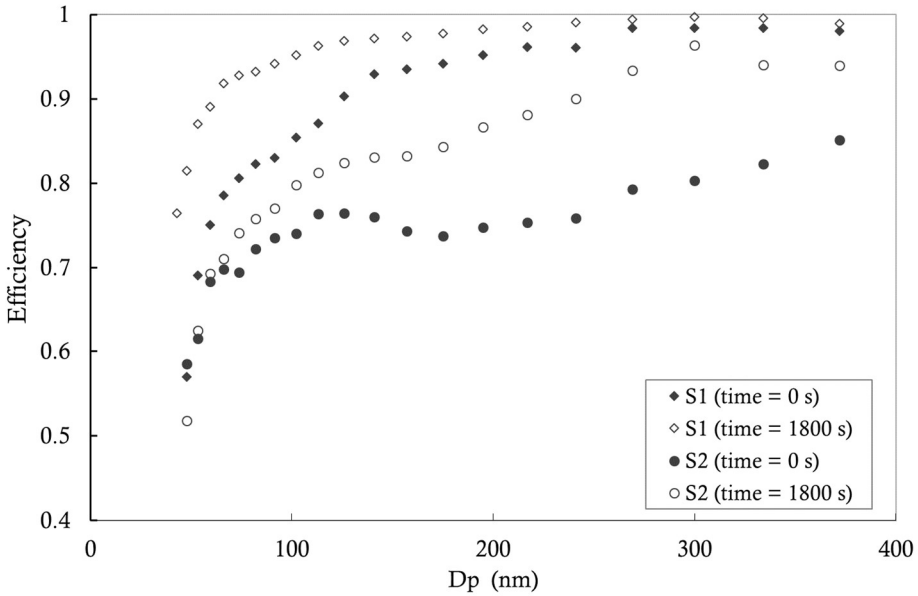

Figure 6.4. Filtration efficiency of the wall-flow bioSiC DPF prototypes as a function of the particle diameter in two different moments: t=0s, and t=1800s [12]

In this study, only the filtration efficiency for particles larger than 50 nanometres is reported. As explained before, for particles smaller than 50 nanometres the concentration of particles generated by the SG was so low that the uncertainty introduced by the SMPS in the raw counts was larger than the measurement itself; therefore, they were disregarded.

6.2.4. Pressure drop

The pressure drop is directly measured in each test with a differential pressure sensor at the inlet and outlet of the filter samples. The transient evolution of the pressure drop is shown in Figure 6.5 for the two measured samples, along with the average curve. The maximum difference in pressure drop between samples S1 and S2 is in this case around 12%. As explained previously,

this difference might be caused by variations in the permeability during the soot load. The initial pressure drop of the 31-mm-long wall-flow filters was around 23 mbar in both cases, so no significant differences are expected in the permeability of the clean filters. Compared to other commercial filters, the bioSiC prototypes designed in this work present a longer and slower transition phase from deep-bed to cake filtration.

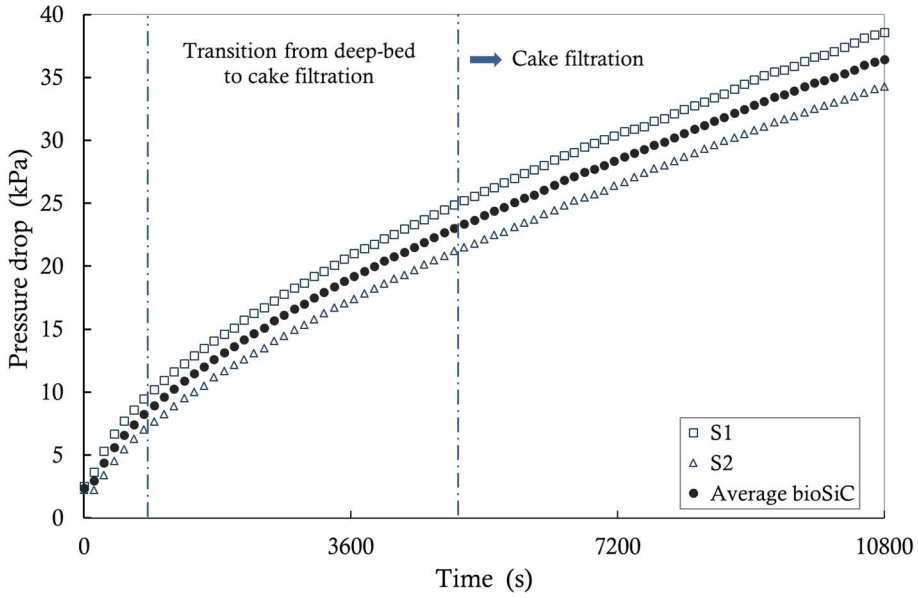

Figure 6.5. Pressure drop of the wall-flow bioSiC DPF prototypes

6.2.5. Preliminary estimation of the performance during the soot load

The soot mass retained in the filter was not directly measured in this study. In order to have an estimation of the behaviour of the filter as a function of the soot load, and to be able to compare with commercial filters, an approximate calculation of the soot load was made based on the power law expression for the effective density (ρ_e) proposed by Mati Maricq [18]. The expression given by Eq. 6.3 characterize fractal-like soot particles generated by diesel engines, where ρ_e is the effective density; but it is a general expression and with an appropriate selection of the fractal dimension D_f and the primary particle parameters (diameter d_m and density d_0), it has been applied to the soot particles artificially generated in the laboratory.

$$\rho_e = \rho_0 \left(\frac{d_m}{d_0}\right)^{D_f-3} \qquad \text{Eq. 6.3}$$

According to Schneider et al. [19], the spark soot particles generated with the SG Palas GFG1000 reveal a fractal dimension of $D_f = 2.1$. On the other hand, according to Wentzel et al. [20] the diameter of the primary particles for Palas soot is 6.6 nm. The density of the primary carbon particles of the soot coming from the Palas SG was estimated from the study carried out by Gysel et al. [21]. It provides with values of the effective density of this Palas soot for some particle sizes (200 nm, 300 nm, and 500 nm). These values were used to determine the density of the primary

particles, and to better adjust the diameter of the primary particle and the fractal dimension. Then, with the general expression of Maricq (Eq. 6.3), the effective density was extrapolated to the rest of the particle size range. The final values of d_0, ρ_0 and D_f used for this work were 1.7 g/cm^3, 6 nm, and 2.05 respectively. The mass of soot in each moment is calculated from the raw number of particles, by multiplying them by the volume of a sphere of the same mobility diameter, and by the effective density.

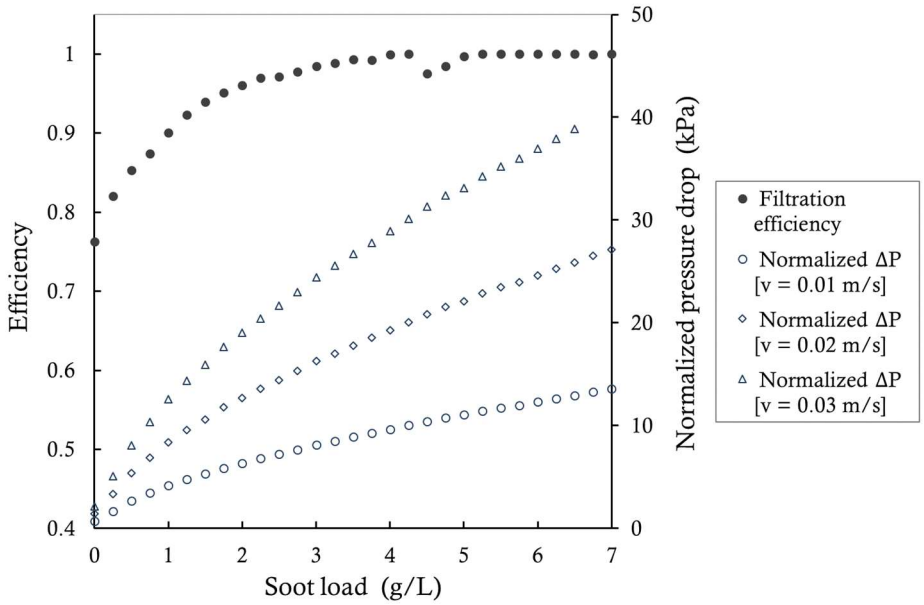

Figure 6.6. Filtration efficiency and normalized pressure drop of the wall-flow bioSiC DPF prototypes as a function of the estimated soot load [12]

In Figure 6.6, the evolution in pressure drop and efficiency are presented jointly as a function of the estimated soot load. The pressure drop has been normalized to different flow velocities to allow the comparison with other filters: v is the darcian velocity of the gas flow through the porous wall. A linear dependence between pressure drop and darcian velocity has been considered neglecting the inertial term.

Table 6.2. Correspondence between gas flow rate and darcian velocity depending on the geometric design

	Tested design	**Reference commercial designs**		
Cell density (cpsi) / Wall thickness (mils)	372/11.8	200/8	200/12	300/12
Gas flow rate (m^3/h)	600	600	600	600
Cell density (cpsc) / Wall thickness (mm)	58/0.3	31/0.203	31/0.305	46.5/0.305
Channel width (mm)	0.96	1.57	1.45	1.13
Internal surface of one channel (m^2)	$1.073 \cdot 10^{-3}$	$1.755 \cdot 10^{-3}$	$1.621 \cdot 10^{-3}$	$1.263 \cdot 10^{-3}$
Frontal area for Ø 10 inch = 25.4 cm (m^2)	0.0507	0.0507	0.0507	0.0507
Total crossing area (m^2)	15.766	13.781	12.728	14.878
Darcian velocity (m/s)	0.0106	0.0121	0.0131	0.0112

Apart from the temperature, which definitely influences the pressure drop in a filter, also the geometrical design affects the pressure drop due to the change in the total crossing area for the gas. In a full size bioSiC filter, taking into account the geometrical design of the honeycomb structure with which the filters of this work have been manufactured (cell density and wall thickness), a darcian velocity of 0.01 m/s would be equivalent to a flow rate of around 600 m^3/h. In Table 6.2, this correspondence between the darcian velocity and gas flow rate for a hypothetical real-size filter (Ø10'', 11'') is presented and compared with the same flow rate for other designs of commercial filters.

6.2.6. Active regeneration of the filter

In this work, the evolution in pressure drop during the regeneration process was measured along with the evolution in temperature in order to get a preliminary idea of the temperature levels required by the wall-flow bioSiC filter to be cleaned and to recover the initial state of pressure drop. Figure 6.7 shows the general trend that was found in all the regeneration processes. Since not all the filtration tests had exactly the same length, and taking into account the deviation that pressured prop presented from one sample to the other, in the regeneration results the pressure drop is presented non-dimensionalized. This way, similar trends are observed for all the tests regardless the sample.

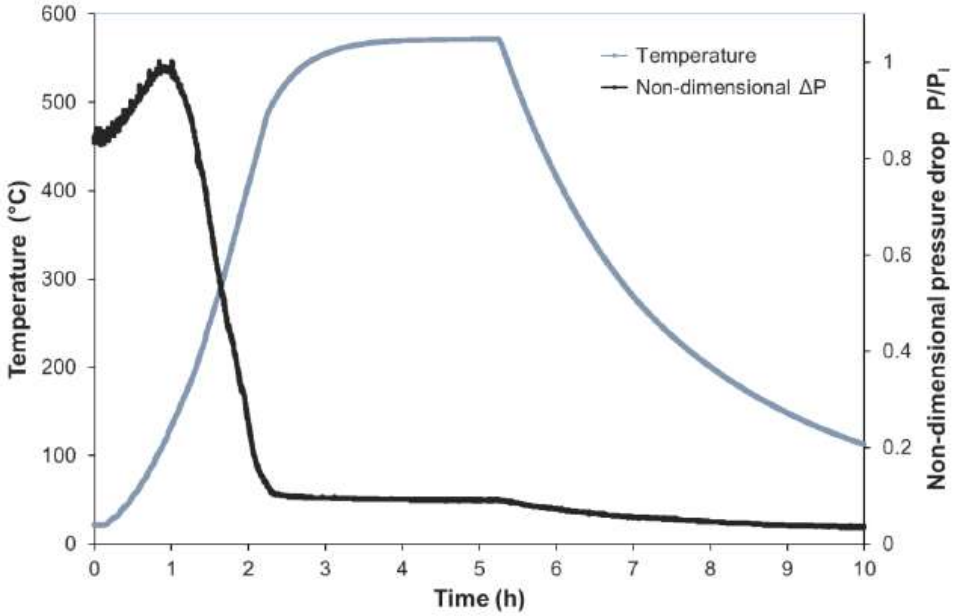

Figure 6.7. Evolution in the temperature and the non-dimensional pressure drop during the regeneration process

In Figure 6.7, it can be appreciated that the temperature follows the programed sequence in the furnace (a ramp of 5 ºC/min until 650 ºC, and a 3 hours-dwell). Nevertheless, in the filter, the temperature usually stays below the target temperature of the furnace. During the dwell, for instance, it stays around 590 ºC. The pressure drop shows a slight rise in the first stage of heating due to the expansion of the gases. Then, as the soot gets burnt, it starts falling and drops to its

minimum just before the temperature reaches the dwell stage. Then, it remains constant until the end of the dwell. Once the reactor finishes the heating sequence and it shuts down, the system starts cooling down so a further decrease in pressure drop is observed from then on due to the cooling of the flowing gases. The response of the pressure drop to the temperature was found to be quick. The most remarkable observation from the graph is that the pressure drop starts decreasing from the beginning of the heating process and that it reaches its minimum level when the temperature in the filter is still around 500 ºC.

With these results obtained from the regeneration process the experimental study was concluded. As a summary, the filtration efficiency and the pressure drop of a small prototype of wall-flow DPF were determined using a laboratory-generated soot-laden stream. The results presented in this study show that, in the initial stage (clean filter), bioSiC wall-flow DPFs may have a filtration efficiency between 0.7 and 0.85 and a pressure drop of around 2 kPa for a normalized wall velocity of 0.01 m/s at ambient temperature. This performance is in line with the performance of other commercial substrates. Although an extrapolation to a large-scale prototype stills needs to be done, these preliminary results show a high particle abatement efficiency with an acceptable pressure drop. The size of a filtration system may affect its filtration parameters, especially its pressure drop since the length of the channels may be a significant factor in the global computation of the pressure drop.

6.3. Results of the numerical simulation

6.4. Summary: potential of wall-flow MDF-bioSiC DPFs

The prototypes of MDF-bioSiC wall-flow DPFs designed in this thesis show significantly high filtration efficiencies. During the experimental tests in the laboratory with the soot generator, efficiencies between 70% and 85% were obtained. When the results are scaled up to a real-size filter under real driving conditions, even a higher efficiency can be expected. Simulations show that values of efficiency around 95% at the clean stage, and close to 100% after a short period of operation time can be expected. The simulation of the bioSiC DPF under the New European Driving Cycle shows that particulate emissions much below the regulation limits can be achieved with this aftertreatment system. The simulation predicts the release of 0.13 mg of soot per km, which is only a 3% of the maximum mass of particles allowed by the Euro 6 standard. It shows the high interest of the bioSiC prototypes developed, able to accomplish by long the higher requirements of particles abatements of the European emissions regulation.

The experimental pressure drop was around 2 kPa for a normalized wall velocity of 0.01 m/s at ambient temperature. When the filter is simulated in real conditions, the initial pressure drop increases up to 3-4 kPa. During the soot loading process, this pressure drop can be as high as 18 kPa in the simulated conditions, but, at that point (5 g/l of soot load) the efficiency has reached practically 100%.

From this results it can be stated that the pressure drop introduced by the MDF-bioSiC DPF prototype is typically high. It is usually higher that the pressure drop introduced by other commercial DPFs, albeit not in all the cases. The main cause of this issue is the low permeability of the chosen precursor. At this point, it is important to underline that all the results presented in this chapter are limited to MDF-bioSiC filters. The prototypes were made from MDF and the numerical model has been built over an MDF filter. MDF-bioSiC tested with the gas flowing perpendicular to the compression direction has lowest permeability among the nine bioSiC specimens studied in this thesis. Despite the relative deviation of the pressure drop respect to the reference cases, the particles abatement efficacy is exceptionally high and offers a wide reduction margin to improve the substrate permeability. There is a wide variety of wood species that might be used as precursors, and many of them are known to have higher permeabilities.

In the same line, it is worth mentioning that the DPF geometry has not been optimized in this work. Different geometry designs with different parameters could have been taken (i.e: looking to reduce manufacturing tasks). Therefore, there is room for iterative improvements the bioSiC DPF designs after the good results obtained.

References

[1] Bautista MA, De Arellano-López AR, Martínez-Fernández J, Bravo-León A, López-Cepero JM. Optimization of the fabrication process for medium density fiberboard (MDF)-

based biomimetic SiC. Int J Refract Met Hard Mater 2009;27:431–7. doi:10.1016/j.ijrmhm.2008.10.016.

[2] Adler J. Ceramic Diesel Particulate Filters. Int J Appl Ceram Technol 2005;2:429–39. doi:10.1016/B978-0-12-385469-8.00032-0.

[3] De Arellano-López AR, Martínez-Fernández J, González P, Domínguez C, Fernández-Quero V, Singh M. Biomorphic SiC: A New Engineering Ceramic Material. Int J Appl Ceram Technol 2005;1:56–67.

[4] Snead LL, Nozawa T, Katoh Y, Byun T, Kondo S, Petti DA. Handbook of SiC properties for fuel performance modeling. J Nucl Mater 2007;371:329–77. doi:10.1016/j.jnucmat.2007.05.016.

[5] Gómez-Martín A, Orihuela MP, Ramírez-Rico J, Chacartegui R, Martínez-Fernández J. Thermal conductivity of porous biomorphic SiC derived from wood precursors. Ceram Int 2016;42:16220–9. doi:10.1016/j.ceramint.2016.07.151.

[6] Greil P, Vogli E, Fey T, Bezold A, Popovska N, Gerhard H, et al. Effect of Microstructure on the Fracture Behavior of Biomorphous Silicon Carbide Ceramics. J Eur Ceram Soc 2002;22:2697–707. doi:10.1016/S0955-2219(02)00135-8.

[7] Singh M, Salem JA. Mechanical properties and microstructure of biomorphic silicon carbide ceramics fabricated from wood precursors. J Eur Ceram Soc 2002;22:2709–17. doi:10.1016/S0955-2219(02)00136-X.

[8] Uchida Y, Ichikawa S, Harada T, Hamanaka T. Durability Study on Si-SiC Material for DPF. SAE Tech Pap 2003;2003-01–03:1–6.

[9] Miwa S, Abe F, Hamanaka T, Yamada T, Miyairi Y. Diesel Particulate Filters Made of Newly Developed SiC. SAE Tech Pap 2001;2001-01–01:1–8.

[10] Civan F. Fluid motion in porous media. In: Wiley, editor. Porous media Transp. Phenom., John Wiley & Sons; 2011, p. 97–144.

[11] Gómez-Martín A, Orihuela MP, Becerra-Villanueva JA, Martínez-Fernández J, Ramírez-Rico J. Permeability and mechanical integrity of porous biomorphic SiC ceramics for application as hot-gas filters. Mater Des 2016;107:450–60. doi:10.1016/j.matdes.2016.06.060.

[12] Orihuela MP, Gómez-Martín A, Miceli P, Becerra-Villanueva JA, Chacartegui R, Fino D. Experimental measurement of the filtration efficiency and pressure drop of wall-flow diesel particulate filters (DPF) made of biomorphic Silicon Carbide using laboratory generated particles. Appl Therm Eng 2018;131:41–53. doi:10.1016/j.applthermaleng.2017.11.149.

[13] Roth C, Ferron GA, Karg E, Lentner B, Schumann G, Takenaka S, et al. Generation of Ultrafine Particles by Spark Discharging. Aerosol Sci Technol 2004;38:228–35. doi:10.1080/02786820490247632.

[14] Dabhoiwala RH, Johnson JH, Naber JD. Experimental Study Comparing Particle Size and Mass Concentration Data for a Cracked and Un-Cracked Diesel Particulate Filter. SAE Tech Pap Ser 2009;2009-01–06:1–12.

[15] Mizutani T, Kaneda A, Ichikawa S, Miyairi Y, Ohara E, Takahashi A, et al. Filtration Behavior of Diesel Particulate Filters (2). SAE Tech Pap 2007 World Congr (SAE Tech Pap 2007) 2007.

[16] Gong J, Rutland CJ. PDF-based heterogeneous multiscale filtration model. Environ Sci

Technol 2015;49:4963–70. doi:10.1021/acs.est.5b00329.
[17] Gong J, Rutland CJ. Filtration Characteristics of Fuel Neutral Particulates Using a Heterogeneous Multiscale Filtration Model. J Eng Gas Turbines Power 2015;137:1–8. doi:10.1115/1.4030282.
[18] Matti Maricq M. Characterization of Combustion and Engine Exhaust Particles. In: Marijnissen JC, Gradon L, editors. Nanoparticles Med. Environ. Inhal. Heal. Eff. 1st ed., Springer Netherlands; 2010, p. 19–37.
[19] Schneider J, Weimer S, Drewnick F, Borrmann S, Helas G, Gwaze P, et al. Mass spectrometric analysis and aerodynamic properties of various types of combustion-related aerosol particles. Int J Mass Spectrom 2006;258:37–49. doi:10.1016/j.ijms.2006.07.008.
[20] Wentzel M, Gorzawski H, Naumann KH, Saathoff H, Weinbruch S. Transmission electron microscopical and aerosol dynamical characterization of soot aerosols. J Aerosol Sci 2003;34:1347–70. doi:10.1016/S0021-8502(03)00360-4.
[21] Gysel M, Laborde M, Mensah AA, Corbin JC, Keller A, Kim J, et al. Technical note: The single particle soot photometer fails to reliably detect PALAS soot nanoparticles. Atmos Meas Tech 2012;5:3099–107.
[22] Samaras Z, Geivanidis S, Vermeulen R, Vonk W, Noble A, Andersson J, et al. Technical feasibility of different regulatory OBD threshold limits (OTL) for Euro 6 (LD) vehicles. vol. Ref. Ares. 2014. doi:10.2769/32688.
[23] Directive 98/69/EC. Off J Eur Comm 1998;350:1–56.
[24] Dabhoiwala RH, Johnson JH, Naber JD, Bagley ST. A Methodology to Estimate the Mass of Particulate Matter Retained in a Catalyzed Particulate Filter as Applied to Active Regeneration and On-Board Diagnostics to Detect Filter Failures. SAE Tech Pap Ser 2008;2008-01–07:1–23.
[25] Tandon P, Heibel A, Whitmore J, Kekre N, Chithapragada K. Measurement and prediction of filtration efficiency evolution of soot loaded diesel particulate filters. Chem Eng Sci 2010;65:4751–60. doi:10.1016/j.ces.2010.05.020.
[26] Tsuneyoshi K, Takagi O, Yamamoto K. Effects of Washcoat on Initial PM Filtration Efficiency and Pressure Drop in SiC DPF. SAE Tech Pap Ser 2011;1:1–10.
[27] www.testo.com. Soot generator testo REXS – Reproducible EXhaust Simulator - Data sheet n.d.:1–2.
[28] Haralampous O, Kandylas I, Koltsakis G, Samaras Z. Diesel particulate filter pressure drop Part 1: Modelling and experimental validation. Int J Engine Res 2004;5:149–62. doi:10.1243/146808704773564550.
[29] Wolff T, Friedrich H, Johannesen L, Hajizera S. A New Approach to Design High Porosity Silicon Carbide Substrates. SAE Tech Pap 2010;2010-01–05:1–11.
[30] Bollerhoff T, Markomanolakis I, Koltsakis G. Filtration and regeneration modeling for particulate filters with inhomogeneous wall structure. Catal Today 2012;188:24–31. doi:10.1016/j.cattod.2011.12.017.

Chapter 7
Conclusions and future work

In this final chapter, the main contributions of the thesis are presented, and the main conclusions of the research are summarized. Finally, some possible future research lines and ideas are presented.

7.1. Main contributions

This thesis contains relevant elements of merit, that surpass the current state of the art regarding the problem of particulate emission control systems in diesel vehicles. The following items are, from the author's point of view, the most relevant attainments:

- In Chapter 4, the results of a filtration-focused characterization study over several bioceramic specimens are presented. The analysed samples were made from precursors selected as potential candidates for filtering applications. And the measured properties were chosen among the possible measurable properties as the most influential parameters in the filtration performance of a substrate.

- In comparison with other characterization studies found in the literature over bioSiC samples, this study has strongly taken into consideration the anisotropy of the material and has provided experimental measurements for both the axial and the radial directions in the majority of the tests.

- In Chapter 5, some relevant relationships between functional parameters of the biomorphic material are identified. They help to predict the potential of other biomorphic substrates made from different precursors (other than the five precursors chosen for this thesis) for their use in particles filtering applications. For instance, thanks to these correlations, the permeability and the filtration efficiency of other biomorphic substrates can be estimated based on their pore size distribution.

- In the general methodology for bioSiC fabrication, the chemical etching with acids for the removal of the remnant silicon has been substituted by an evaporation of the silicon at

high temperatures. This alternative procedure has two main advantages: the elimination of the risks associated with the handling of acids, and the possibility of treating thicker pieces assuring the complete removal of the silicon.

- Remarkable contributions have been made in the manufacture of complex bioSiC pieces. This thesis addresses for the first time the manufacture of wall-flow-type geometries by mechanization instead of by extrusion. A successful technique has been proposed for that purpose. In addition, solutions for accurately sticking bioSiC pieces and casting additional parts in the material such as the plugs of the channels are provided.

- In Chapter 6, experimental measurements of the filtration performance of an MDF-bioSiC wall-flow DPF prototype are provided for both the initial state and during the soot load. The tests were performed in controlled and repeatable conditions, yielding accurate results and allowing a better understanding of the effect of different factors in the filters performance.

- A detailed numerical model has been applied to the tested MDF-bioSiC wall-flow DPF prototype that takes into account the microstructural features of the substrate. This model has allowed to scale the results up to a real-size MDF and to evaluate the potential of this novel system in the automotive industry.

7.2. Main research conclusions

From the characterization study, several conclusions have been drawn.

One important advantage of bioSiC compared to other commercial substrates is the wide range of densities, porosities and pore sizes that can be obtained depending on the selected precursor. The porosimetry study has revealed that bioSiC samples made from natural precursors present a trimodal distribution of pores. The first range between 0.1 and 20 μm; the second between 2 and 60 μm; and the third one from 30 μm and upward. From the three pore size ranges, the third one (corresponding to large macropores) is the most detrimental to the filtration efficiency.

The results have shown that the cutting direction of the wood is a crucial factor in the filtration performance of the biomaterial. In general, the permeability and the filtration efficiency of bioSiC substrates is lower when the gas crosses the material in the same direction of the cells (parallel to the axis of the tree). For all bioSiC samples in the axial direction, except for Pine-bioSiC, k_1 was at the same order of magnitude (10^{-11} m^2) in contrast to radial samples for which all values were around 10^{-12} m^2, an order of magnitude lower. k_2 for all axial samples was in the range of 10^{-7} m, and 10^{-8} m in the case of radial samples.

Thermal conductivities of bioSiC are in the range of 4–88 W/m K and significantly decrease with increasing temperature. The thermal and mechanical properties are also highly dependent on this

factor. The heat diffusion is favoured when the heat flux is applied in the same direction than the pores. And the compression strength is also higher when the load is applied in the direction of the fibres. Maximum compressive strength ranges from 8 to 88 MPa in axial samples, while in the radial orientation it is 1.4–3.2 times lower, ranging from 2 to 10 MPa.

Average pore size, alignment of pores and tortuosity seems to be key factors in the permeability results. An Ergun-type relationship has been proposed in this work to predict the permeability of a biomorphic material as a function of the equivalent pore size. The equivalent pore size is determined by integrating the pore size distribution within specific integration limits stablished as a function of the flux direction.

BioSiC has lower thermal conductivity, lower compressive strength and lower thermal expansion coefficient (CTE) than monolithic β-SiC. The thermal conductivity and (indirectly) the compressive strength affect negatively the Thermal Shock Resistance (TSR); but the lower CTE compensates this effect. In general, biomorphic SiC offers a wider range of TSRs compared to other materials typically used as substrate in DPFs: from 0 to 30 W/mK. The anisotropy plays again a fundamental role in the resulting behaviour. BioSiC TSR turns out to be better when the loads (thermal and mechanical) are applied in the direction of the cells. In some cases, the calculated values surpass those of Re-SiC, inorganic SiC and cordierte.

Three possible correlations between thermal conductivity and porosity (taken from the previous literature) have been analysed in this work as potential prediction tools for the thermal behaviour of biomorphic silicon carbide. The three models show discrepancies with the experimental values, especially with the axial samples at low porosities. Reasonable fits are obtained with the Litovskii equation and the Kingery equation. However, bioSiC exhibit a complex and multimodal pore size distribution; and the thermal conductivity of two-phase systems depends not only on the amount of porosity but also on the pore shape and distribution.

As stated in previous studies, the compressive strength shows a dependency on the density and, consequently, on the porosity. In this work, the model of Gibson and Ashby has been suggested to correlate the relative strength with the density of the biomorphic material.

These observations point to the possibility of tailoring the permeability, the thermal conductivity or the compressive strength by selecting a particular wood precursor and controlling the microstructural parameters of the final porous ceramics. With the control of these properties, the best optimum requirements for filtering applications of the end product may be fulfilled.

By using MDF as precursor, a wall-flow DPF can be manufactured that significantly improves the filtration efficiency of other commercial alternatives of the market. Through this work, the suitability of bioSiC as particulate filter substrate for automotive applications has been widely demonstrated in terms of filtration efficiency. At the clean state, the MDF-bioSiC prototypes had a filtration efficiency of about 77%. After two hours of soot loading, their filtration efficiency reached values of around 100%.

From the results obtained with the prototype, it is concluded that wall-flow DPFs made from MDF can largely comply with the emission limits imposed by the current European standards. When the MDF-bioSiC wall-flow DPF was simulated under the NEDC cycle, the calculated amount of released particle was $8.75 \cdot 10^{8}$ particles/km (0.129 mg/km), which is far below the limit imposed by the current European limit: $6 \cdot 10^{11}$ particles/km (4.5 mg/km).

Due to the low permeability of MDF walls of the bioSiC prototype, the pressure drop introduced by the MDF-bioSiC DPF is typically high. The initial pressure drop of the prototypes tested in laboratory conditions (with the SG) was around 23 mbar. When the full-scale MDF-bioSiC wall-flow DPF is simulated in the real exhaust of an engine, higher values are obtained. The pressure drop of MDF-bioSiC wall-flow DPFs is usually higher that the pressure drop introduced by other commercial DPFs. However, the exceptionally high abatement efficacy of the designed prototype offers a wide reduction margin to improve the substrate permeability. It is worth mentioning that the geometrical design of the filter has not been analysed in this work, so even further improvement may be expected by optimizing the geometrical features of the system.

7.3. Future works

Although important contributions have been made regarding the manufacture of complex bioSiC elements such as the wall-flow geometry of DPF, further effort is still necessary to move forward in the learning curve for the application of this material at commercial stage. Still there are some issues that may be optimized. The mechanization process for example is specially challenging due to the small size of the channels and the limited length of the drilling tools. Besides, the high number of channels that must be mechanized to conform a full filter, along with the abrasive properties of carbon, leads to a premature wear of the mechanizing tools. The union/welding of pieces made of porous bioceramic materials carries important difficulties too, especially if the porosity of the contact surface needs to be preserved.

This thesis was focused on the microstructure of the substrate and in how it affects the behaviour of the whole wall-flow DPF but the geometrical design of a wall-flow DPF (diameter, length, wall thickness, cell density) may also affect its filtration performance. In this work, the bioSiC wall-flow DPF prototype was carefully designed paying attention to these aspects, but their influence on the filtration performance of the prototype was not specifically studied. In order to further improve the performance of the resulting bioSiC wall-flow DPF, it would be interesting to adapt and optimize the geometry to different precursors and DPF configurations.

It is important to underline that all the results presented in Chapter 6 of this thesis derive from the usage of only one type of precursor. As repeatedly commented, the wall-flow DPF prototypes for this thesis were manufactured from MDF for two main reasons:

- First, because the only initial quantitative requirement for DPF is the maximum amount of particles that they let scape from the exhaust pipe, set by the Euro 6 regulations; and MDF turned out to be one of the most efficient precursors among the five options studied.

- And second, because up to now the manufacturing process involves mainly manual procedures, and from a practical point of view it was easier to use a homogenous material rather than a natural wood, where the hardest seams might hinder the mechanization of the small channels.

The final filtration efficiency of the MDF-bioSiC wall-flow DPF prototype was well above the minimum necessary to comply with the current Euro 6 standards, while the backpressure it introduced was higher than the backpressure introduced by other commercial filters. For future works, it would be interesting to explore the possibility of selecting precursors with similar efficiency and but higher permeability in order to reduce the pressure drop of the DPF without affecting its filtration capacity, as well as designing different DPF geometries for a better adaptation to these precursors.

The numerical model used for this thesis was calibrated with the experimental measurements of the MDF-bioSiC prototypes. Consequently, the conclusions of the numerical simulations are valid basically for MDF filters. In order to be able to extrapolate these conclusions to other DPFs made with other precursors, additional experiments with the alternative prototypes would be needed. The use of numerical tools like the one proposed in this thesis allows to perform many simulations and getting many conclusions with few resources in a short time. Testing small prototypes and extrapolating its behaviour through numerical simulation tools may result indispensable before moving on to the manufacture of a full-scale prototype.

In future steps, advanced designs with optimized geometry/precursor selection should be tested in real engines for different applications and engine designs.

In this work, the performance of bioSiC wall-flow DPFs is assessed based on the intrinsic microstructural and physical properties of the substrate. The influence of other phenomena in the filtration performance of the bioceramic filters was not considered: the chemistry of soot oxidation processes, the influence of catalysts deposition, or the thermal regeneration processes, were out of the scope of this thesis. An interesting research line for the future could involve exploring the performance of the bioSiC filters from a chemical point of view, including the deposition of catalysts or a deeper analysis on the regeneration process.